Sedimentation of Oblate Ellipsoids

Von der Fakultät Mathematik und Physik der Universität Stuttgart
zur Erlangung der Würde eines Doktors der
Naturwissenschaften (Dr. rer. nat.) genehmigte Abhandlung

vorgelegt von

Frank Rodolfo Fonseca Fonseca

aus Bogotá Colombia

Hauptberichter:	Prof. Dr. H. J. Herrmann
Mitberichter:	Prof. Dr.-Ing. Rainer Helmig
Tag der mündlichen Prüfung:	14. Mai 2004

Institut für Computeranwendungen 1 der Universität Stuttgart

2004

To Laura Sofia,

a little part of heaven

on earth ...

Contents

Kapitel 1

Deutsche Zusammenfassung

Newton zeigte, dass Körper mit einer konstanten Beschleunigung auf die Erde fallen, aber trotz der unleugbaren Anziehung der Schwerkraft bewegen sich nicht alle fallenden Gegenstände auf gerader Flugbahn abwärts. Die Betrachtung der Flüssigkeit beinhaltet sehr schwierige und nichtlineare Interaktionen. Trotz der bahnbrechenden Bemühungen durch Maxwell (1853), der als erstes die Körper- Flüssigkeit-Interaktion betrachtet hat, blieb das allgemeine Problem ohne Lösung. Andererseits ist die Sedimentbildung eines Systems von Partikeln in einer Flüssigkeit unter dem Einfluss der Schwerkraft ein sehr wichtiges Problem in der Hydrodynamik und in der Statistischen Physik. Dieses Problem hat viele Anwendungen in den grundlegenden Wissenschaften wie in den Luftfahrtwissenschaften, der Biophysik, der Klimaforschung sowie auf dem Gebiet der technischen chemischen Reaktoren, z.B. der Ausbreitung von Verschmutzung, in Tintenstrahldruckern, den druckaufgeladenen Wirbelschichtsystemen, etc.. Dieses Problem weist schwierige Multikörper-Interaktionen wegen der weitreichenden Hydrodynamik auf, die für Kugeln über einen Bereich von $1/r$ abfällt, wobei r der Abstand zwischen den Partikeln ist, Ramaswamy (2001). Troz diese breiten Anwendungmöglichkeiten fehlt der Partikelsedimentbildung weiterhin eine statistisch-mechanische und hydrodynamische Beschreibung und bleibt ein ungelöstes Problem.

1.1 Simulationsmethode

Das Modell wurde durch Höfler and Schwarzer (2000) entwickelt, erweitert durch Kuusela et. al. (2001) und wird in einigen Studien von Kuusela et. al. (2003) und Fonseca and Herrmann ((1) 2004) angewandt. Die Bewegung von Flüssigkeiten wird gelöst, indem man die inkompressiblen Navier-Stokes Gleichungen auf einem diskreten Gitter löst:

$$\begin{array}{c} \frac{\partial \mathbf{v}}{\partial t} + (\mathbf{v} \cdot \boldsymbol{\nabla})\mathbf{v} = -\boldsymbol{\nabla} p + \frac{1}{Re}\nabla^2 \mathbf{v} + \mathbf{f} \\ \boldsymbol{\nabla} \cdot \mathbf{v} = 0 \end{array} \tag{1.1}$$

wobei $\mathbf{v}$ die Geschwindigkeit der Flüssigkeit ist, sowie p den Druck und $\mathbf{f}$ eine externe Kraft darstellt, die in unserem Problem die Schwerkraft ist. Die Reynoldszahl

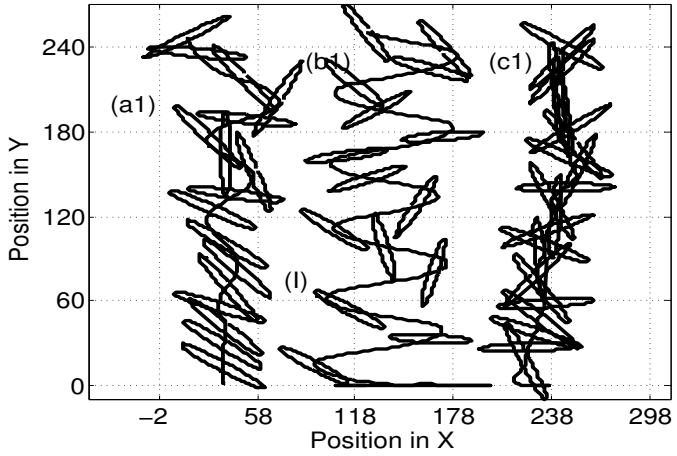

Abbildung 1.1: Typische Falltrajektorien in unseren Simulationen. Wir zeigen das unveränderlich-fallende Regime, $(a1)$, mit $\Delta r = 0.25$, $\nu = 0.033$; $(b1)$ die periodische Oszillation mit $\nu = 0.025$, $\Delta r = 0.133$. $(c1)$, und die chaotische Bewegung mit $\Delta r = 0.25$, $\nu = 0.033$.

$Re = v2R_M\rho_f/(\nu)$, wobei v die vertikale oblate Ellipsoidgeschwindigkeit ist, $2R_M$ der größte Durchmesser des oblaten Ellipsoids, ρ_f die Dichte und $\nu = \mu/\rho_f$ die kinematische Viskosität (μ ist die Scherviskosität). Die Froude Zahl ist $Fr = (v^2)/(g(2R_M))$, $\mathbf{g}$ ist dabei die Schwerkraft. Die Grenzbedingungen zwischen der Flüssigkeit und den oblaten Ellipsoidpartikeln sind erfüllt, wenn man in Betracht zieht, dass die Bewegung der Flüssigkeit auf der Partikeloberfläche abhängig von der rutschfreien Grenzbedingung ist, $\mathbf{v}(\mathbf{x}) = \mathbf{v_t} + \mathbf{r}(\mathbf{x})_{CM} \times \boldsymbol{\omega}$, wobei $\mathbf{v}_t$ die translationale Geschwindigkeit des Ellipsoids ist, $\mathbf{r}(\mathbf{x}_{CM})$ der Vektor von seiner Mitte zum Punkt $\mathbf{x}$ an der Ellipsoidoberfläche, und $\boldsymbol{\omega}$ die Winkelgeschwindigkeit des Ellipsoids.

Die Interaktion zwischen der ellipsoidalen Oberfläche und der Flüssigkeit, die an das Ellipsoid angrenzt, wird erhalten, indem man eine wiederherstellende Kraft einfügt, die eine "Verteilungskraft" in die Volumenkraft der Navier-Stokes Gleichung verursacht. Diese Verteilungskraft ahmt die Gegenwart des Ellipsoids in dem Sinne nach, dass die Flüssigkeit innerhalb des Ellipsoids sich wie ein steifer Körper bewegt. Eine nichtreibende Kraft wird ausgeübt, wenn die Partikelschablone und der steife Körper nicht in der gleichen Position sind (Höfler (2000)).

Die repulsive Kraft zwischen den Ellipsoiden wird proportional zu ihrer Überlappung gewählt. Wenn die oblaten Ellipsoide nichtüberlappend sind, ist die Kraft null, und über kurze Abstände vermeiden die hydrodynamischen Kräfte, die das Vorhandensein der Flüssigkeit beschreiben, den Kontakt zwischen den Partikeln (Kuusela et. al. (2001)). Für diese Kraft wird eine Kontaktfunktion gewählt, die eingehender in Kuusela et. al. (2001) und in Perram and Rasmussen (1996) erklärt wird. Die Geometrie des oblates Ellipsoids wird durch sein Seitenverhältnis Δr gekennzeichnet, definiert als das Verhältnis des minimalen Radius R_m zum maximalen Radius R_M, somit $\Delta r = R_m/R_M$.

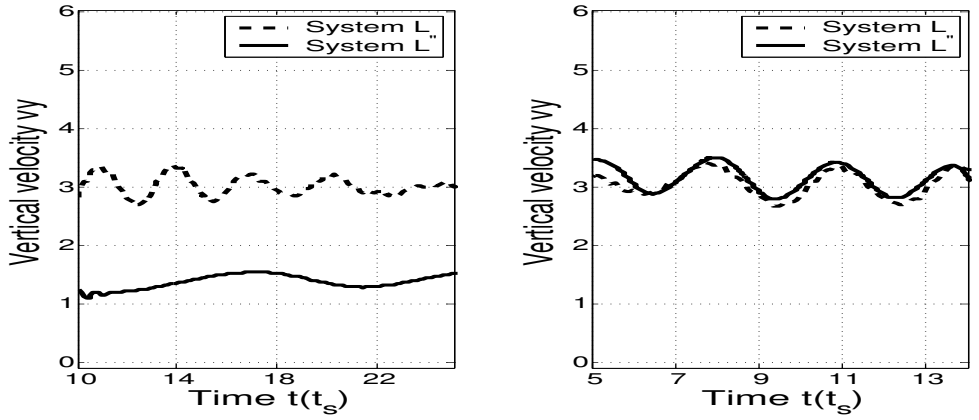

Abbildung 1.2: Ausgangsbedingungen im System: $\theta_o = 26.6^0$, $h_o = 220$, $\Delta r = 0.15$ und kinematische Viskosität $\nu = 0.083$. In der Abbildung stellen wir die vertikale Geschwindigkeit gegen die Zeit in beiden Systemen (durchgezogene Linie), $L^{'}$, ($n = 2$, gestrichelte Linie mit Quadraten) dar. Die Superposition wird durch Anwendung der Umkehrtranformation durchgeführt, die in Tabelle 1.1 beschrieben wird.

System L	$\rightarrow$	System $L^{'}$			System L	$\rightarrow$	System $L^{'}$
L_{hor}	$\rightarrow$	$n * L_{hor}$			T^*	$\rightarrow$	$n * T^*$
R_M	$\rightarrow$	$n * R_M$			v_{hor}	$\rightarrow$	$\frac{v_{hor}}{n}$
R_m	$\rightarrow$	$n * R_m$			v_{vert}	$\rightarrow$	$\frac{v_{vert}}{n}$
g	$\rightarrow$	$\frac{g}{4*n}$					

Tabelle 1.1: Transformationsregeln der Sedimentation. n ist eine reelle Zahl.

1.2 Die Phasen

Wir fanden drei unterschiedliche Arten von Bewegung, genannt Phasen, in unseren Simulationen: Der stationäre Zustand, die seitliche oder periodische Bewegung (Belmonte et. al. (1998)) und eine chaotische Bewegung, die in Abb. 1.1 gezeigt werden.

1.3 Der stationäre Zustand und periodische Phasen: Ähnlichkeitgesetz.

Die Grenzgeschwindigkeit v wird bestimmt durch das Gleichgewicht zwischen den Trägheits- und Viskositätskräften $F_i = F_d$, daher ist $v \sim \sqrt{gR_m}$. Wir nehmen an, dass die charakteristische Periode der Bewegung von der seitlichen Abmessung L_{hor} des Behälters abhängt und von der vertikalen Abmessung unabhängig ist. Folglich nehmen wir an, dass die Periode sich wie $T^* \sim L_{hor}/v$ ändern sollte. Die Transformation in Tabelle 1.1 läßt die Froude und Reynoldszahl konstant und die Dynamik in den zwei Systemen ist äquivalent,

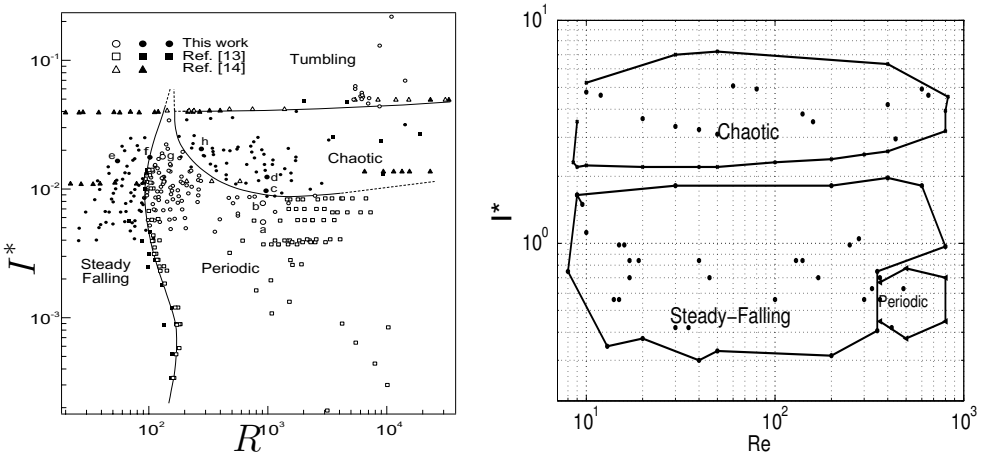

Abbildung 1.3: Die linke Abbildung zeigt das Zustandsdiagramm der fallenden Scheiben wie in Belmonte et. al. 1998 berichtet. In des rechten Abbildung stellen wir der Phasenraum für das fallende oblate Ellipsoid dar, das wir in unseren Simulationen erhalten haben.

wenn sich die dynamischen Variablen wie in Tabelle 1.1 (Abbildung 1.2) ändern. Auch die Dynamik für den stationären Zustand und die periodischen Phasen werden auf dieser Skala unabhängig voneinander.

1.4 Zustandsdiagramm und Übergänge.

Im Phasenraum definieren wir ein dimensionsloses Trägheitsmoment $I^\star = \frac{5}{4}\frac{\rho_{ellip}}{\rho_{fluid}}\Delta r$, das das Verhältnis des Trägheitsmoments des oblaten Ellipsoids zu der seines kugelförmigen Äquivalents bei der gleichen Reynoldszahl $Re = \frac{U(2r_M)}{\nu}$ ist. Es ist wichtig zu erwähnen, dass das Experiment für eine fallende Scheibe mit kleinen Seitenverhältnissen durchgeführt wurde, und wir erwarten, dass die Dynamik des Systems ähnlich der eines oblaten Ellipsoids sein wird.

Wenn wir unser Diagramm in Abb. 1.3 rechts mit den experimentellen Resultaten links in Abb. 1.3 (Field et. al. (1997)) vergleichen, sehen wir, dass in beiden Abbildungen die Verteilung der Phasen ähnlich ist. Die Unterschiede bezüglich unseres Diagramms mit denen von Field et. al. (1997) sind, dass sie Scheiben benutzen und nicht oblate Ellipsoide und das Taumel-Regime nicht in unseren Resultaten vorkommt. Die Koexistenz der dynamischen Phasen ist von der anfänglichen Orientierung des oblaten Ellipsoids unabhängig.

Links in Abbildung 1.4 zeigen wir das Verhalten der charakteristischen Zeit T^*/T. Mit Erhöhung die Reynoldszahl Re geht die charakteristische Zeit nach Null bei $Re_c \approx 355$ (Abb. 1.3). Nach diesem Punkt finden wir die periodische Phase, die sich wie die Phase des unverändlichen Fallens mit einer unendlichen charakteristischen Zeit verhält. Folglich können wir T^*/T als Ordnungparameter betrachten, und der Kontrollparameter für diesen Übergang ist die Reynoldszahl. Dieser Übergang ist wie ein Phasenübergang zweiter Ordnung. Die innere Abbildung stellt das Potenzgesetz mit einem kritischen Exponenten

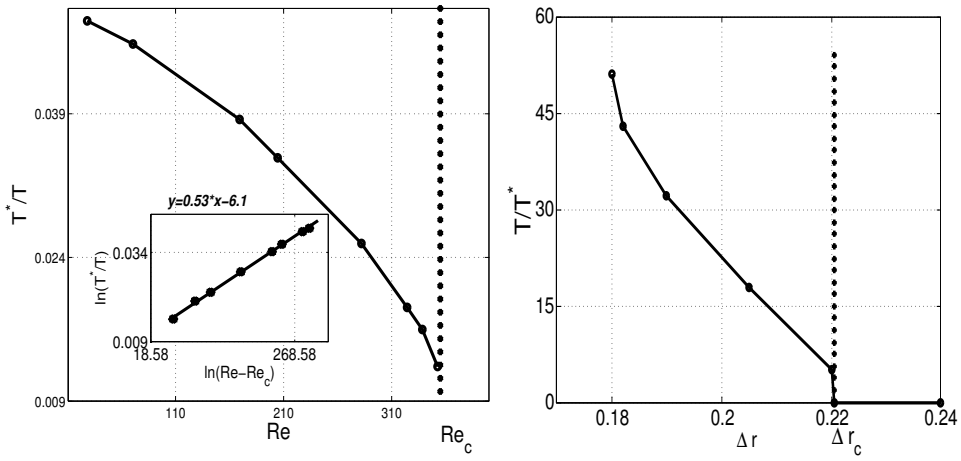

Abbildung 1.4: Die linke Abbildung stellt den T^*/T gegen den Ordnungparameter Re, mit $Re_c \approx 355$ dar. Die innere Abbildung zeigt das Potenzgesetz-Verhalten mit einem Exponenten nahe bei 0.5. Die rechte Abbildung zeigt den T/T^* gegen den Ordnungsparameter Δr, mit $\Delta r_c \approx 0.22$.

≈ 0.5 dar. Im Fall des oberen Teils des Übergangs, Abb. 1.3, deutet die Veränderung des oblaten Ellipsoid-Seitenverhältnisses die Änderung von einen stationären Zustand Fallen zu einem periodisches Regime an.

Der Übergang vom stationären Zustand Fallen zum chaotischen Regime wird in Abb. 1.4 rechts dargestellt. Wir verwenden T/T^*, d.h. die Inverse des zuvor verwendeten Ordnungsparameters, um den Übergang zu beschreiben und als Kontrollparameter das Seitenverhältnis Δr. Bei Δr_c wird ein endlicher Sprung des Ordnungsparameters beobachtet. Die charakteristische Zeit T/T^* verschwindet wegen der nicht-regelmässigen bewegungen, die gegen kleine Schwankungen der anfänglichen Orientierung sehr empfindlich sind. Dieser Übergang scheint daher ein Phasenübergang erster Ordnung zu sein.

1.5 Sedimentationsgeschwindigkeit für oblate Ellipsoide

In der linken Abbildung 1.5 zeigen wir die mittlere vertikale Sedimentationsgeschwindigkeit $v(t)_{\|}$ als Funktion des Volumenanteils Φ_V für Ellipsoide und Kugeln und v ergleichen dann mit dem phänomenologischen Richardson-Zaki Gesetz $\frac{v(\Phi)}{v_0} = (1-\Phi_V)^n$ (Richardson and Zaki (1954)) mit $n = 5.5$. Der Grenzwert $\Phi_V \rightarrow 0$ entspricht dem einzelnen fallenden Ellipsoid, das wir in Fonseca and Herrmann ((1) 2004) studierten. Es ist interessant zu unterstreichen, dass die Sedimentationsgeschwindigkeit des Ellipsoids, die dem phänomenologischen Richardson-Zaki Gesetz folgt, verglichen mit der der äquivalenten Kugel, klein ist. Für Ellipsoide geht die vertikale Mittelgeschwindigkeit durch ein lokales Maximum bei $\Phi_V \approx 0.05$. Dieses Maximum ist ziemlich interessant, da es nicht für Kugeln beobachtet wird. Ähnliche nicht-monotone Sedimentation über nicht-kugelförmige Körper (z.B. Fasern) ist experimentell durch Herzhaft and Guazzelli (1999) und für pro-

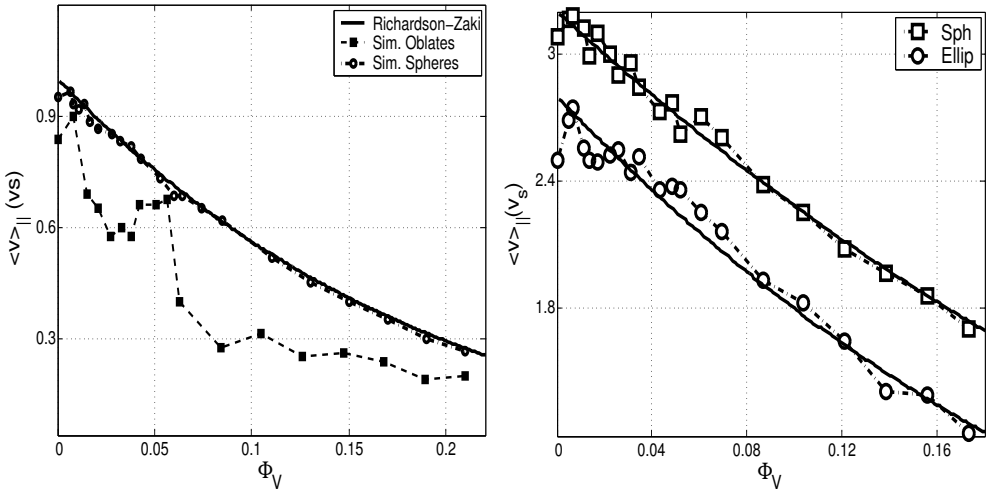

Abbildung 1.5: Linker Plot zeigt die mittlere Sedimentationsgeschwindigkeit $v(t)_{\|}$ für das oblate Ellipsoid (gestrichelte Linie mit Quadraten) und die Kugel (gestrichelte Linie mit Punkten), als Funktion des Volumenanteil Φ_V bei $Re = 4 * 10^{-2}$. Die rechte Abbildung zeigt die mittlere Sedimentationsgeschwindigkeit bei $Re \approx 7$. Das oblate Ellipsoid-Seitenverhältnis ist $\Delta r = 0.25$, die äquivalent Kugel hat $R_{equi} = 0.97$.

late Ellipsoide in Simulationen von Kuusela et. al. (2001) berichtet worden.

Abbildung 1.5 rechts stellt die mittlere vertikale Geschwindigkeit für Ellipsoide (□) und die äquivalenten Kugeln (○) als Funktion des Volumenanteil bei niedriger Reynoldszahl dar (Re ≈7). In einer vorhergehenden Arbeit ist diese Simulationsmethode mit Erfolg bis zu $Re \approx 10$ (Höfler and Schwarzer (2000) und Kuusela et. al. (2003)) verwendet worden. Das Zwischenmaximum für die Ellipsoide wird nicht in Abb. 1.5 rechts beobachtet, wie in Abb. 1.5, links bei der niedrigen Reynoldszahl gezeigt. Ein Vergleich mit dem phänomenologischen Richardson-Zaki Gesetz (durchgezogene Linie im Abb. 1.5 rechts) zeigt einen Exponenten von $n_{Sph} = 3.2$ für Kugeln und $n_{Ellip} = 4.0$ für Ellipsoide. In beiden Fällen folgen die Daten dem Richardson-Zaki Gesetz recht gut. Diese Exponenten ($n_{Sph} = 3.2$ und $n_{Ellip} = 4.0$) liegen zwischen dem Grenzwert niedriger Partikel-Teilchen-Zahlen ($n \approx 4.5$) und einem turbulenten Partikelsystem ($n \approx> 2.5$), Richardson and Zaki (1954).

1.6 Orientierungsverhalten

Die mittlere vertikale Orientierung (MVO) θ wird als Funktion des Volumenanteils in Abb. 1.6 links gezeigt. Für kleinere Volumenanteile zeigt das MVO eine stärkere Ausrichtung mit der Schwerkraft, und im Grenzfall $\Phi_V \to 0$ wird eine genauere Ausrichtung mit der Schwerkraft beobachtet, welches dem Orientierungsverhalten für ein oblates Ellipsoid entspricht, das in Fonseca and Herrmann ((1) 2004) beobachtet wurde. Wir sehen auch für das MVO ein Zwischenmaximum bei $\Phi_V \approx 0.05$, welches das lokale Maximum der vertikalen Geschwindigkeit bei gleichem Volumenanteil erklären könnte, das in

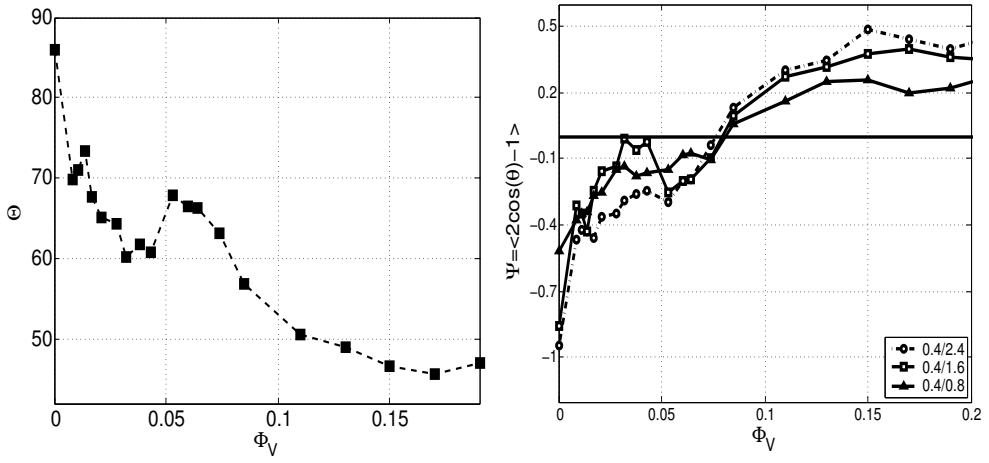

Abbildung 1.6: Die Verteilungsfunktion $P(cos(\theta))$ für die mittlere vertikale Orientierung θ für unterschiedliche Volumenanteile. Das Ellipsoid-Seitenverhältnis ist $\Delta r = 0.25$ und die Reynoldszahl $Re = 4 * 10^{-2}$. Ordnungparameter Ψ als Funktion des Volumenanteils, Φ_V für, drei unterschiedliche Seitenverhältnisse $\Delta r = 0.4/2.4$; $0.4/1.6$;$0.4/0.8$.

Abb. 1.5 dargestellt ist. Dieses Zwischenmaximum existiert nicht für Kugeln. Für größere Werte des Volumenanteils ($\Phi_V > 0.08$) zeigt die Abbildung eine monotone Abnahme.

Um die Orientierung der oblaten Ellipsoide quantitativ zu bestimmen führen wir die Größe $\Psi =< 2cos(\theta) - 1 >$ ein, die auch in Kuusela et. al. (2003) als Ordnungsparameter der Orientierung mit den Werten -1, 0 oder $+1$ verwendet wurde, wenn alle oblaten Ellipsoide zur Schwerkraft senkrecht, zufällig orientiert oder entlang der Schwerkraft ausgerichtet sind. Abbildung 1.6 rechts zeigt das Verhalten von Ψ gegen Φ_V, für kleinere Volumenanteile nimmt der Ordnungsparameter $\Phi_V \approx 0.001 - 0.08$ negative Werte an, was die Ausrichtung entlang der Schwerkraft beweist und in Übereinstimmung mit dem Grenzwert, $\Phi_V \rightarrow 0$ (ein oblates Ellipsoid) Fonseca and Herrmann ((1) 2004), ist. Ungefähr bei $\Phi_V \approx 0.08$ ist der Ordnungsparameter Null. Für größeres $\Phi_V \geq 0.08$, die orientierung deutet bei positivem Ordnungparameter senkrecht zur Schwerkraft. Im Bereich von $\Phi_V \approx 0.001 - 0.08$, hat Ψ ein lokales Minimum nahe bei $\Phi_V \approx 0.05$, wo wir ein lokales Maximum in Abb. 1.6 rechts und in Abb. 1.5 links fanden. Die Simulationen wurden mit zwei anderen unterschiedlichen Längenverhältnissen wiederholt, $\Delta_r = 0.4/0.8; 0.4/2.4$, und wir beobachteten ähnliches Verhalten.

1.7 Diffusion

Abbildung 1.7 (a) zeigt die Ableitung der mittleren quadratischen Teilchenverschiebung dR/dt für sedimentierende Ellipsoide, wobei $R(t) =< [x(t) - (x(0) + < v > t)]^2 >$ ist. Die Klammern bedeuten, dass ein Mittelwert über das Ensemble jener Partikel, die sich im unteren Bereich des Behälters befinden, gebildet wird. $< v >$ ist die mittelere Geschwindigkeit aller Partikel mit $v \neq 0$. Die Graphiken stellen die größen Anisotropie den parallelen ($\|$) und senkrechten ($\perp$) Anteile dar. Im Allgemeinen stellen beide Anteile

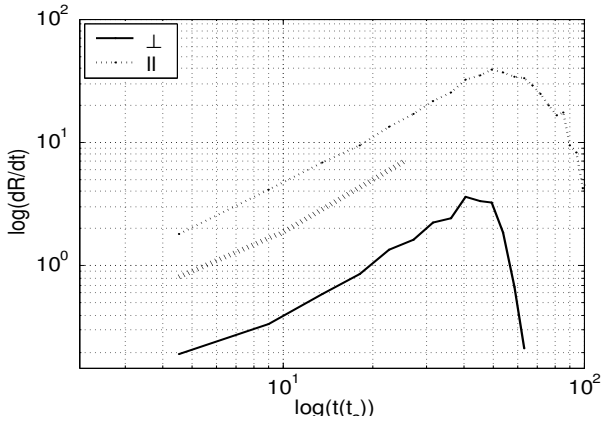

Abbildung 1.7: Abbildung zeigt die parallelen ($\|$) und senkrechten ($\perp$) Anteile der M.S.D. für sedimentierende Ellipsoide in einer log-log Skala. Die dicken gepunkteten Linien dazwischen stellen das Wachstum in den ballistischen und nicht-diffusiven Regimen dar. Der Kugelradius ist $R_{equi} = 1.01$. Die Reynoldszahl ist 2×10^{-2} und das Seitenverhältnis $\Delta r = 0.4/1.6$. Die Zahl der Ellipsoide ist von der Größenordnung 10^3.

Zeit	$\rightarrow$	Adimensional Zeit	
t	$\rightarrow$	$\frac{t}{t_s}$	
$< x^2 >$	$\rightarrow$	$\frac{<x^2>}{4R_{eq}^2}$	
v	$\rightarrow$	$\frac{v}{v_s}$	

Tabelle 1.2: Transformationsregeln für die Sedimentation

ein anfängliches sogenanntes ballistisches Regime dar, wie in Abbildung 1.7 (a), durch eine parallele dicke gepunktete Linie zwischen den Kurven bildlich dargestellt ist. Dieses ballistische Regime ist zu t^2 proportional. Wir finden ein nicht-diffusives Verhalten definiert durch $R(t) \equiv t^\alpha$ und Exponenten zwischen $1.4 \leq \alpha \leq 2.5$, deren Werte von der Ellipsoiddichte, der Viskosität und dem Seitenverhältnis abhängen.

In Tabelle 1.2 stellen wir die Tranformationsregeln dar, die verwendet werden, um die Graphiken in Abbildung 1.8 übereinander zu legen. Die Reynoldszahl wird durch die Tranformationsregeln unverändert gelassen. Dieses Ergebnis gilt für kleine $Re \lessapprox 10^{-2}$.

1.8 Räumliche Korrelationen

Wir beginnen unsere Analyse, indem wir die räumlichen Korrelationen in den Geschwindigkeitsfluktuationen studieren (im Folgenden SCVF). Die normalisierte Autokorrelationsfunktion des parallelen ($\|$) Anteils der Geschwindigkeitsfluktuationen werden wie folgt definiert (Segré et. al. (1997)):

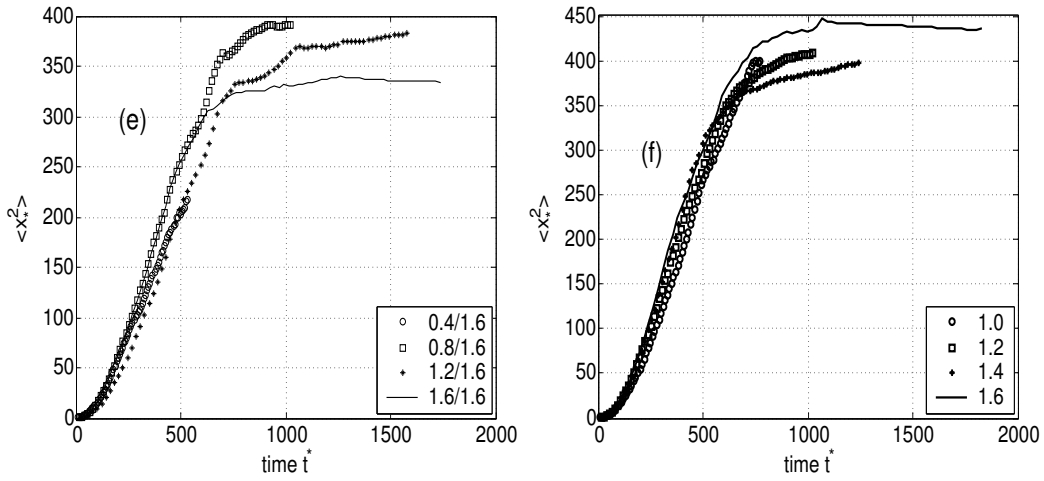

Abbildung 1.8: Alle Kurven liegen relativ gut übereinander, was die Transformationsregeln in Tabelle 2 rechtfertigt.

$$C_{\parallel}(\mathbf{r}) \equiv \frac{\langle \delta v_{\parallel}(0) \delta v_{\parallel}(\mathbf{r}) \rangle}{\langle \delta v_{\parallel}(0)^2 \rangle} \tag{1.2}$$

wobei die Klammern $\langle ... \rangle$ einen Ensembledurchschnitt über mehrere individell unterschiedliche Konfigurationen im Raum und in den Orientierungen (Ellipsoide) darstellen. Dabei stellt $\delta \mathbf{v}_i = \mathbf{v}_i - \mathbf{v}_{sed}$ die Fluktuationen in der Geschwindigkeit und $\mathbf{v}_{sed} = \langle v_i \rangle$ die Mittlere Geschwindigkeit der Konfiguration dar. Falls der Abstand $\mathbf{r}$ in der Richtung genommen wird, die zur Schwerkraft parallel ist, dann nennen wir die parallele Komponente $C_{\parallel}(x) = C_{\parallel}$ oder falls senkrecht dazu, dann nennen wir die senkrechte Komponente $C_{\parallel}(z) = C_{\perp}$.

1.9 Änderungen im Volumenanteil und Kollaps

Abbildung 1.9 zeigt, dass alle Kurven des SCVF für Kugeln und Ellipsoide im ($||$) Anteil zur Schwerkraft übereinstimmen. Hier bei wird der Abstand $R_{eq}\Phi_V^{-1/3}$ benutzt, wie von Segré et. al. (1997) vorgeschlagen. Bei der Übereinstimmung der Kurven betrachten wir es als bemerkenswert, dass sie für Änderungen des Volumenanteils bis zum 60-fachen gültig ist. Die von uns gefundenen Korrelationslängen können wie folgt angegeben werden: $\xi_{\perp,sph} = 29 r_{eq}\phi^{-1/3}$; $\xi_{\parallel,sph} = 13 r_{eq}\phi^{-1/3}$, was sich nicht erheblich von den Resultaten von Segré et. al. (1997) unterscheidet. Im Ellipsoidfall (siehe Abbildung 1.9, (b)), findet man auch eine sehr gute Übereinstimmung der Kurven. Die Werte für die Korrelationslänge sind $\xi_{\perp,Ell} = 25 R_{eq}\Phi^{-1/3}$; $\xi_{\parallel,Ell} = 10 R_{eq}\Phi^{-1/3}$. Die Korrelationslänge für Ellipsoide ist in beiden Anteilen kleiner als für Kugeln.

Die Amplitude der parallelen ($\parallel$) und senkrechten ($\perp$) Anteile der Geschwindigkeitsfluktuationen ist in Abbildung 1.10 dargestellt. Die Graphiken werden in einer log-log Skala dargestellt. Für $0.005 \leq \Phi_V \leq 0.07$ sind Fluktuationen gefunden worden, die sowohl für

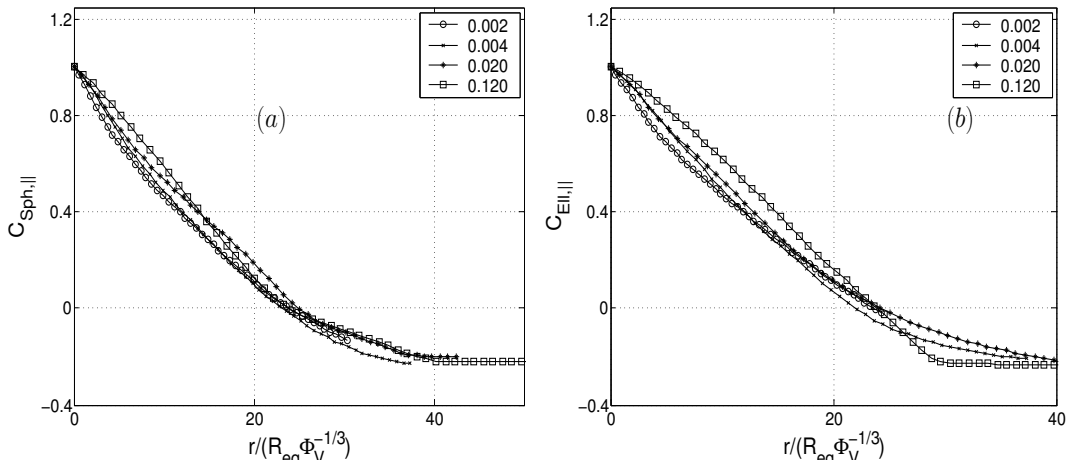

Abbildung 1.9: Kollaps der räumlichen Korrelationsfunktion für den (||) Anteil für Kugeln (a) und Ellipsoide (b).

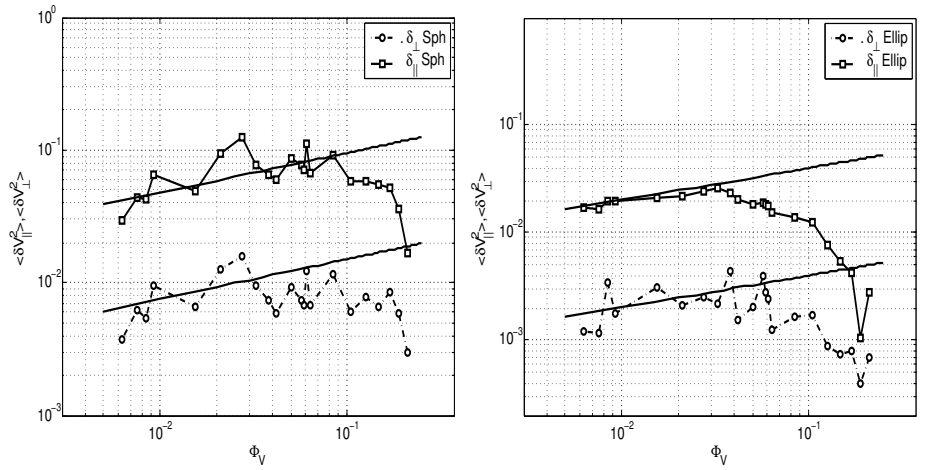

Abbildung 1.10: Die oberen Abbildungen stellen die räumlichen Korrelationsfunktionen für Kugeln und Ellipsoide in den parallelen (||) und senkrechten ($\perp$) Anteilen als Funktion des Volumenanteils in einer log-log Skala dar. Die Reynoldszahl ist 2×10^{-2}, der Radius $R_{equi} = 1.01$ der Kugeln und das Ellipsoid-Seitenverhältnis ist $\Delta r = 0.4/1.6$.

Kugeln, als auch für Ellipsoide wie $\approx \Phi_V^{1/3}$ (die gerade Linie über den Daten) wachsen, (Segré et. al. (1997)). Für größere Volumenanteile $\Phi_V > 0.07$) werden die Fluktuationen in beiden Anteilen, für Kugeln und für Ellipsoide, verringert.

1.10 Änderung der Behältergröße

Wir studieren die Geschwindigkeitsfluktuationen wie in der vorhergehenden Arbeit von Segré et. al. (1997) und verändern die Korrelationslänge, um Größeneffekte zu untersuchen. Die Resultate sind in der Abbildung 1.11 für Kugeln (gestrichelt-punktierte

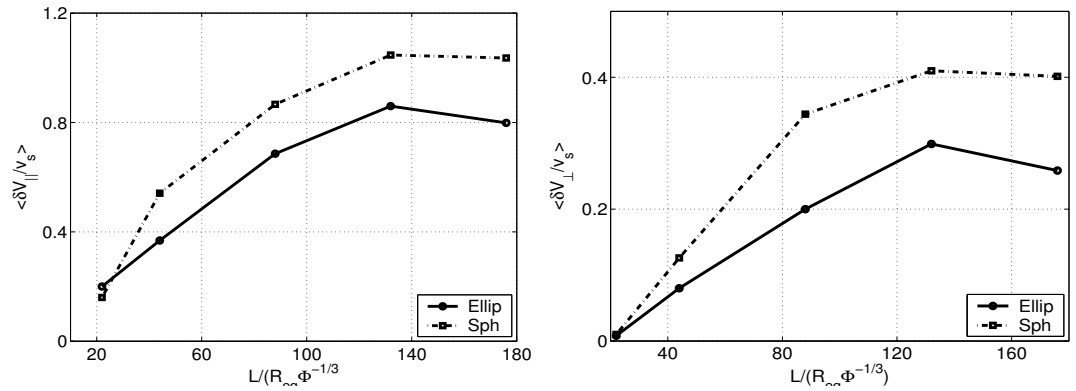

Abbildung 1.11: Die linke Abbildung zeigt den parallelen Anteil der Geschwindigkeitsfluktuationen bei veränderlicher Behältergröße. Die rechte Abbildung zeigt den vertikalen Anteil. Die Reynoldszahl ist 2×10^{-2}, der Radius der Kugeln ist $R_{equi} = 1.01$, und das Ellipsoid-Seitenverhältnis ist $\Delta r = 0.4/1.6$.

Linie) und Ellipsoide gezeigt (durchgezogene Linie). Die Behältergrößen werden mit $L/(R_{equ}\Phi^{-1/3})$ normalisiert. Wie im Fall von Segré et. al. (1997) und von Höfler (2000) zeigen die Geschwindigkeitsfluktuationen eine anfängliche Übergangsregion, die eine starke Abhängigkeit von der Behältergröße, zwischen $20 \leq L/(R_{eq}\Phi^{-1/3}) \leq 100$ haben. Danach sind die Simulationsdaten unabhängig von der Behältergröße. Im Allgemeinen zeigen Ellipsoide und Kugeln das gleiche Verhalten, aber mit einem kleineren Gesamtwert für Ellipsoide. Wie erwartet wird ist das Verhältnis des Parallelanteils $\parallel$ der Geschwindigkeitsfluktuation zum Vertikalanteil $\perp \approx 2.5$ für Kugeln und Ellipsoide, Segré et. al. (1997). Der gleiche Wert für beide Partikelnformen beweist, dass das anisotrope Verhalten der Geschwindigkeitsfluktuation von der Partikelform unabhängig ist. Die durch die Schwerkraft verursachte Symmetriebrechung wirkt gleichermaßen auf Kugeln und Ellipsoide.

Caflish and Luke (1985) fanden, dass die Geschwindigkeitsfluktuationen bei Zunahme der Behältergröße divergieren können. Andererseits wurde weder in Experimenten, Simulationen, noch in der Theorie ein Beweis für solche Divergenzen gefunden. In Höfler (2000) wird argumentiert, dass Systeme, die durch Wände begrenzt sind, nicht eine vergleichbare Skalierung der Geschwindigkeitsfluktuationen aufweisen. Stattdessen zeigen sie eine Sättigung, sobald die kleinste Ausdehnung des Behälters eine kritische Größe übersteigt. Es besteht die Schwierigkeit, ein einziges Skalierungesetz zu finden. In unseren Simulationen wurde die Behältergröße variiert, indem man die gesamte quadratische Unterseite änderte. Die Resultate in Abb. 9.7 (a) und (b) zeigen keine Divergenz der Geschwindigkeitsfluktuationen für Kugeln oder Ellipsoide und bewegen sich sehr nahe an den Resultaten, die durch Segré et. al. (1997) gegeben werden.

Chapter 2

Introduction

2.1 The falling objects

The tree leaves flutter to the ground in autumn, exhibiting a complex motion and refusing to follow the shortest path. The way in which objects fall to the ground has been studied since antiquity. Objects were thought to return to "their natural" places by the ancient Greeks. During Renaissance, Galileo Galilei dropped two metal balls from the leaning Tower of Pisa and showed that they fall at the same rate despite having different masses. Newton showed, that the bodies fall on earth driven by a constant acceleration and he also observed the complex motion of objects falling in both air and water (Viets and Lee (1971)).

But despite gravity's undeniable attraction, not all falling objects travel downwards in straight trajectories. The consideration of fluid surrounding the objects (figure 2.1), introduces a very complicated and nonlinear interaction between the object and the fluid. The first pioneering effort was made by Maxwell (1853), who was the first to consider the fluid-object interaction and proposed a model for a falling paper strip.

In the beginning, theoreticians made few assumptions
a) constrained motion in 2-d was taken into account
b) vortices in fluid were ignored
c) considered a fluid with zero viscosity
Based on these assumptions, Gustav Kirchhof showed that the problem reduces to a simplified set of equations that can be solved for simple particle geometries. This method also appears in the Horace lamb's classic treatise on hydrodynamics, (Lamb (1932)).

A deeper understanding of the motion of falling objects in a fluid is of great technical importance, and has been investigated in a variety of contexts, including meteorology (Kajikawa (1982)), aircraft stability (Mises (1945)), power generation (Lugt (1983)), chemical engineering (Marchildon et. al. (1964)), and also in the study of stability of submarines and the centrifugation of cells by biological techniques.

In the nineties Aref and Jones (1993), found by means of numerical solutions of Kirchhoff's equations that the trajectory of an object moving through an incompressible, invis-

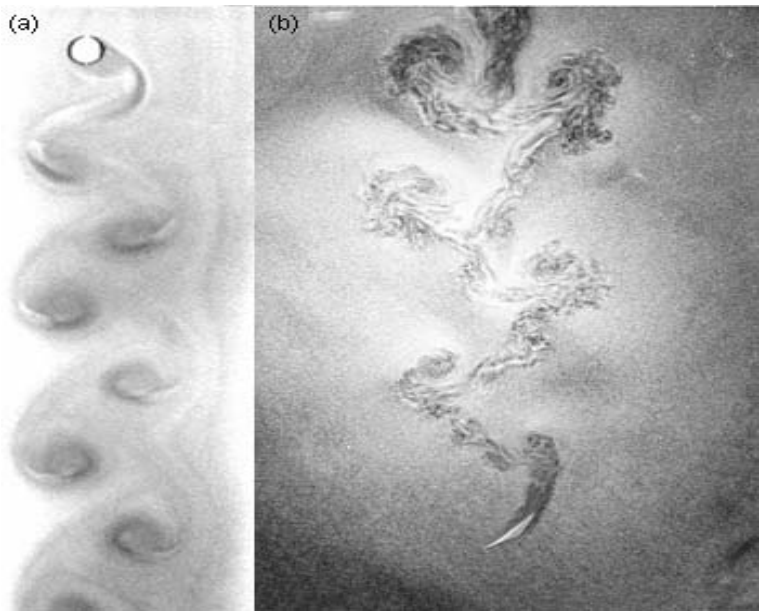

Figure 2.1: Images of the vortices shedding by (a) a rising air bubble (Kelly and Wu 1997) and (b) a metal strip as it falls through water (S. Field et al 1998). It is possible to see the fluid motion due to a dispersion of small aluminum particles in the water. The vortex sheds in each case are synchronized with the zigzag motion of the object.

cid and irrotational fluid is chaotic. Tanabe and Kaneko (1994,95) and Mahadevan et. al. (1995) used a phenomenological model for the falling of a piece of paper in 1-d. They included the lift and kinematic viscosity, but neglected the inertia of the fluid, and described five falling regimes of which two were chaotic. Further, Mahadevan (1996) implemented an older work presented in Horace Lamb's classic treatise on hydrodynamics to the problem of falling cards that takes into account the effect of the fluid as a shape-dependent renormalization of the mass and the moment of inertia tensor. Tumbling and drift motion were observed which are a consequence of the anisotropy in mass and viscosity in the model. Furthermore, Mahadevan et. al. (1999) also made an experiment by dropping horizontal cards of thickness d and width w showing that the tumbling frequency, Ω scales as $\Omega \approx d^{1/2}w^{-1}$, consistent with the dimensional argument that balances the drag against gravity.

Additionally, Field et. al. (1997) investigated experimentally the behavior of falling disks in a fluid and identified different dynamical regimes as a function of the moment of inertia and the Reynolds number. They obtained experimental evidence for chaotic intermittency (Bauer et. al. (1992)). Belmonte et. al. (1998), in an experiment with thin flat strips falling in a fluid, observed two motions: side to side oscillation (flutter) and end-over-end rotation (tumbling) figure 1.2. They proposed a phenomenological model including inertial drag and lift which reproduces this motion and yields the Froude similarity which describes the transition from fluttering to tumbling regime.

In spite of this large effort, the general problem of the falling of a body in interaction with the surrounding fluid (figure 2.1), remains without solution.

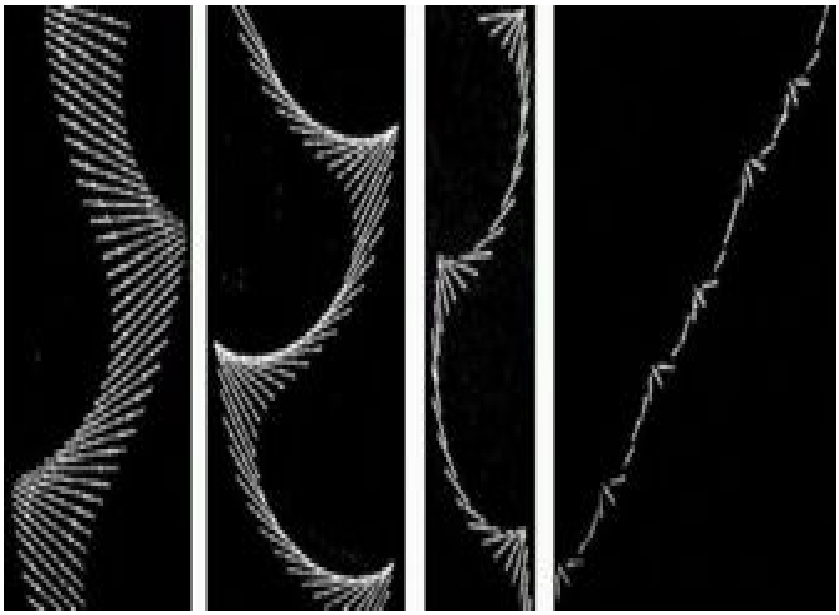

Figure 2.2: The images show a collage of consecutive video fields (Belmonte et. al. 1998) of two fundamental motions: side-to-side oscillation (flutter) and end-over-end rotation (tumble).

2.2 Many particle sedimentation

The sedimentation of a system of particles in a fluid under the action of gravity is a very important problem in fluid dynamics and statistical physics. This problem has many applications in basic sciences such as aerospace sciences, biophysics, environment, etc, and in the field of engineering e.g. chemical reactors, contamination spreading, ink-jet printing, fluidized beds, etc. Many natural processes involve particles immersed in fluids for example, blood flux, particles in the atmosphere, diffusion studies of organelles transport in living cells, paper making, sedimentation in rivers and lakes. To understand such systems, a better knowledge in sedimentation and ability to simulate the sediment behavior is very much required. With this wide range of applications, the particle sedimentation still lacks a statistical mechanical and fluid dynamical description and remains an open problem.

Sedimentation and statistical physics have a long and distinguished common history, beginning with the classical theoretical (Einstein (1906)) and experimental (Perrin (1916)) studies of Brownian motion. The early work dealt primarily with suspensions at or near thermal equilibrium. This meant that the source of fluctuations in the system is a thermal bath characterized by the temperature. The correlation and response functions of physical observables are tightly linked by fluctuation dissipation relations. The interest of physicists in the statistical mechanics and hydrodynamics of suspensions (Pusey (1997)) has continued to the present day with the focus shifting progressively to the problems of systems far from equilibrium. The effect of shear flow on the structure and crystallization of suspensions has received a great deal of attention (Ackerson and Clark (1984)); the con-

ceptually simpler state of sedimentation (Russel et. al. (1989), Blanc and Guyon (1991)) where there is on average no relative motion of the particles.

2.3 Driven suspension and hydrodynamic dispersion

Systems presenting steadily sedimenting suspensions are in a non-equilibrium state and therefore have properties qualitatively different from the system in thermal equilibrium in two important ways. Firstly, the suspended particles are denser than the fluid and also in order to balance between gravity and viscous dissipation on average there is a downward relative speed. Secondly, irrespective of the particle being sedimented or sheared, they display random particle motion even when the thermal Brownian motion is negligible. Each particle influences the other in such a way that the dynamics is highly sensitive to initial conditions. The resulting chaos as observed in Brady and Bossis (1985) and Jánosi et. al. (1997), implies that the time-evolution of the coarse-grained quantities must be described using diffusion coefficients and noise sources, even though the microscopic dynamics in the absence of thermal Brownian motion is entirely deterministic. This phenomenon of diffusive behavior induced by the flow due to the objects driven through the fluid, in the absence of a thermal noise is called hydrodynamic diffusion or hydrodynamic dispersion. This places many questions about the large-scale structure and long-time dynamics of sedimenting or sheared suspensions mainly in the domain of non-equilibrium statistical physics rather than traditional fluid dynamics.

In general, the suspended particles are acted upon by Brownian and other forces. If D_{th} is the thermal Brownian diffusivity of a solute particle with radius a in a flow with typical velocity gradient $\dot{\gamma}$ around the particle, then the P*é*clet number Pe,

$$Pe = \frac{\dot{\gamma} a^2}{D_{th}} \tag{2.1}$$

is a dimensionless measure of the importance of particle flow compared to the thermal diffusion in the suspension. For a particle moving (for example, sedimenting) with a speed v through an unbounded fluid,

$$\dot{\gamma} \approx \frac{v}{a} \tag{2.2}$$

For a Brownian sphere of radius a and buoyant weight (i.e. weight minus the weight of solvent displaced) $W = m_R g$ settling through a viscous fluid at temperature $k_B T$ in energy units, the settling speed, v_s is:

$$v_s = \frac{m_R g}{\Gamma} \tag{2.3}$$

Here, g is acceleration due to gravity and Γ is the coefficient of viscous drag of the fluid ($\Gamma = 6\pi a\nu$ for a sphere). The Einstein relation tells us that the diffusivity, $D_{th} = k_B T/\Gamma$. Thus, $Pe = m_R g a/k_B T$ is independent of the kinetic coefficients of the system. A

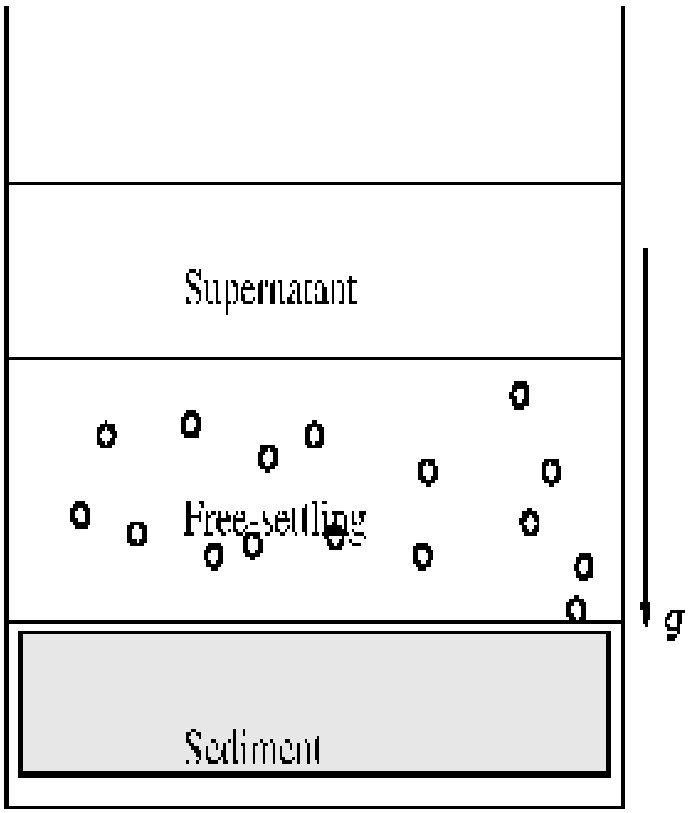

Figure 2.3: Batch sedimentation.

suspension in which Pe is extremely large, (10^2 or more) is a non-Brownian suspension. In such suspensions the physics is dominated by the driving force (gravity in the case of sedimentation) and hydrodynamics whereas thermal fluctuations play a negligible role.

In contrast De Groot and Mazur (1984), non-equilibrium steady states such as flow of electrical or thermal currents, fluctuations and hydrodynamic diffusivities in driven non-Brownian suspensions are determined by the driving force. They have nothing to do with the thermodynamic temperature of the system and are hence not constrained by fluctuations dissipation relations. Even in suspensions with $Pe = 1$, there will be substantial non-equilibrium contributions to diffusion, fluctuations and linear response of the hydrodynamic interactions.

2.4 Steady sedimentation and the fluidized bed geometry

One of the most familiar aspects of sedimentation is the separation (figure 2.3), of a suspension into sediment and supernatant with a free-settling layer in between (Russel et. al. (1989)) under steady sedimentation. This state can in principle be realized by studying

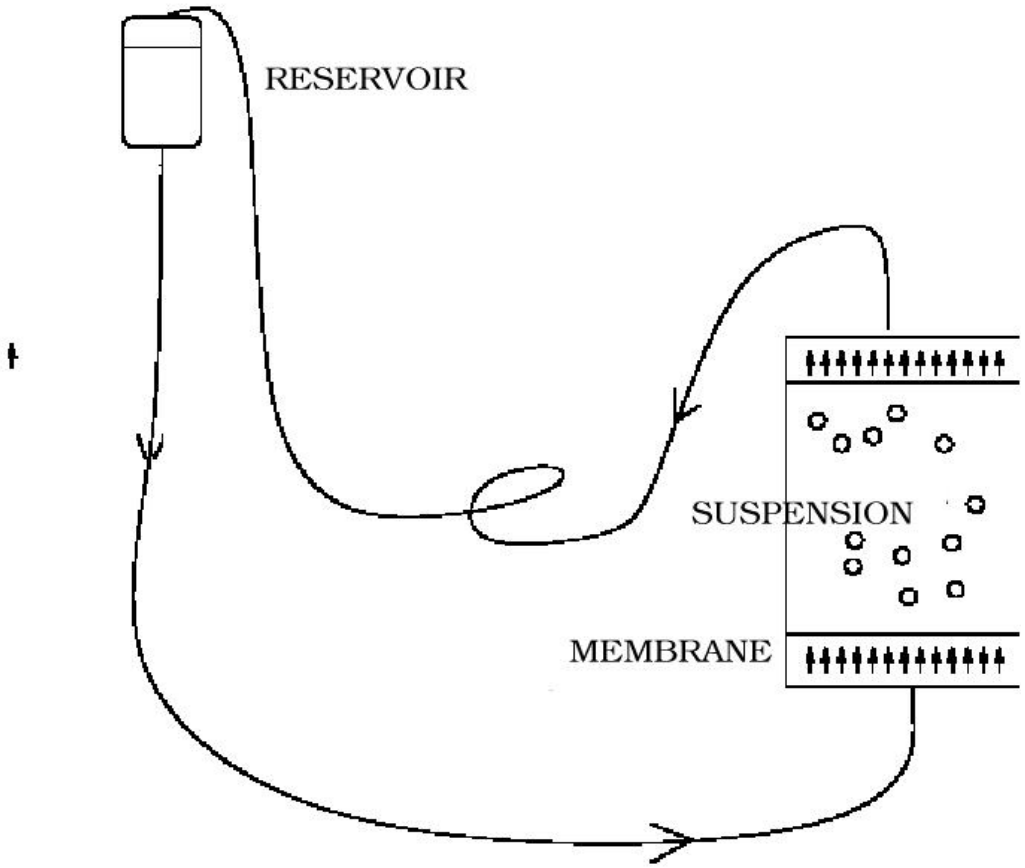

Figure 2.4: Fluidized bed.

the free-settling region alone, while feeding in particles from the top to compensate those which form the sediment. An elegant way of achieving this idea in a spatially homogeneous perpetually settling state is to move the reference frame with the settling particles in the 'fluidized geometry' (reference Xue et. al. (1995)) as follows. Subject the suspension to an upward flow of speed v_0 from below (figure 2.4). The number density, n_0 is spatially uniform and is compatible with the flow rate. For samples whose linear dimensions are large in all directions the behavior, apart from a change of reference frame, should be identical in the bulk to that of a collection of particles with number density n_0 settling with speed v_0 in the laboratory frame in an unbounded fluid. Although not all the experiments that have been performed in the fluidized-bed geometry probe the statistical properties of steady-state sedimentation, it is an ideal setting for such studies. The majority of the experiments, even those performed in conventional batch sedimentation are carried out under the implicit assumption that the underlying state is statistically stationary. Throughout the many-ellipsoid part of this thesis we are concerned with the nature of such a steadily sedimenting state and fluctuations about this state.

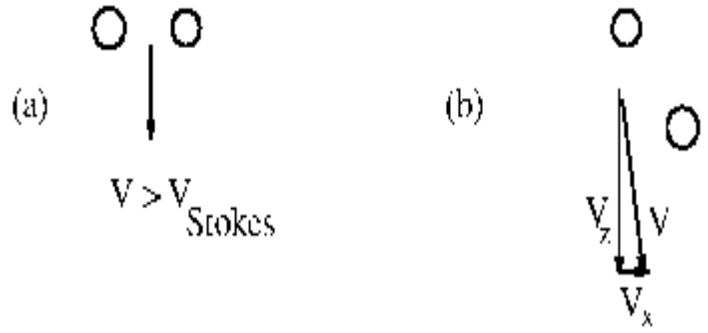

Figure 2.5: (a) A pair of particles settling side by side settles faster than an isolated particle; (b) a pair with oblique separation vector settles with a small horizontal component to its velocity.

2.5 Low Reynolds number flow

The Reynolds number $Re = U(2 * R_M)/\nu$ is a measure of the ratio of inertial to viscous forces in the flow of a fluid with $\nu = \mu/\rho$ the kinematic viscosity and μ the shear viscosity; ρ the mass density; with U and L being the vertical velocity and the largest radius of the ellipsoid, respectively. For the suspensions, Re ranges from 10^{-3} up to 4 depending upon the values of ρ and ν.

If we work in the Stokesian limit, $Re = 0$, several important features of Stokesian flow in the presence of particles (Russel et. al. (1989)) can be summarized.

(i) The equations of the fluid flow in this limit are linear.

(ii) An isolated single particle of buoyant weight W settling under gravity in an unbounded container gives rise to a velocity field decaying as W/r with distance, r from the particle to any point in the fluid.

(iii) A localized density fluctuation about a background of uniform concentration of settling particles likewise produces a $1/r$ velocity fluctuation.

(iv) The relative velocity of an isolated pair of settling particles in an unbounded fluid is zero: they neither approach, recede from nor rotate about each other. If they start at the same height, they fall together (figure 2.5 (a)) at a speed greater than that of an isolated single particle subjected to the same force. If they are initially separated both vertically and horizontally, their center of mass falls not vertically but obliquely with the velocity pointing in a direction between the vertical and the vector joining the upper particle to that at the lower position (figure 2.5 (b)).

(v) The dynamics of three or more particles is complex and chaotic (Jánosi et. al. (1997)).

2.6 Velocity fluctuations in hard-sphere sedimentation

An approximate theory in sedimentation begins with the pioneering work by Batchelor (Batchelor (1970)). He computed the particle sedimentation velocity by assuming a homogeneous spatial distribution in the dilute limit to get the mean particle sedimentation velocity. The theory predicts that at small volume fraction, ϕ the sedimentation velocity will be:

$$U(\phi)/U_0 = 1 - 6.5\phi + O(\phi^2) \tag{2.4}$$

with U_0 being the equilibrium velocity of a sphere.

In general, this problem reveals a very complicated multi-body interaction due to the long-range hydrodynamic interaction that decays for a sphere as $1/r$ (Batchelor (1970)) where r is the distance from the particle for a spatially infinite system at small Reynolds number. The particle velocities can fluctuate around the mean, both along the gravity (the vertical) and the perpendicular direction (horizontal plane). Very little is understood about the nature of these velocity fluctuations Ramaswamy (2001).

Apart from recent advances in the field this old subject of suspension dynamics poses exciting problems in the frontiers of non-equilibrium statistical physics. Much progress has been made on this problem both experimentally and theoretically. At the same time, several puzzles remain as diverging views do on the basic issues. We describe each problem first and outline the progress made.

2.6.1 Caflisch and Luke's work

A severe problem in the statistical physics of sedimentation was pointed out by Caflisch and Luke (hereafter CL Caflish and Luke (1985)). A very brief resume is given here. Consider a steadily sedimenting fluid-like suspension (see section 1.3) of hard spheres. A concentration fluctuation near the origin in this suspension is a point-like force density and in three dimension, gives rise to a velocity fluctuation decaying as $1/r$ with r being distance from the origin. The linearity of Stokes flow implies that the velocity field resulting from many spatially distributed concentration fluctuations is simply the sum, $\sum v_i$ of the individual contributions. If these fluctuations take place in a random and spatially uncorrelated manner throughout the suspension, the resulting variance in velocity, σ_v^2 at any point in the suspension would be clearly the sum of the squares of the individual contributions. This $\sum v_i^2$ has $N \approx L^3$ terms if there are N solute particles in a container of linear dimension, L in all directions. The $1/r$ form mentioned above for the velocity fluctuation produced by a localized concentration fluctuation means that $\langle v_i^2 \rangle \approx L^{-2}$ so that $\sigma_v^2 \approx L$. Such a diverging variance in the infinite L limit, poses serious problems in the calculations (Batchelor (1970)), of the mean settling speed in an unbounded suspension. Most experiments find size independence unlike the prediction by Caflisch and Luke but there are serious questions (Brenner (1999)), that can be asked about the interpretation of the measurements. It is fair to say that experiments have neither confirmed the CL predictions nor definitely ruled them out. It should of course be noted that $CL's$ 'predictions'

say that if the concentration fluctuations are statistically independent from one point to another in space then the velocity variance diverges. Sufficiently strong anticorrelations in the particle concentration field at large length scales will suppress the CL divergence. Clearly what is necessary is a theory that tackles concentration and velocity fluctuations on the same footing instead of postulating the one and inferring the other.

2.6.2 Resume of experiments and simulations

Experiments on the velocity-fluctuations problem use a wide range of techniques including tracking the velocity field by particle imaging (Segré et. al. (1997)), direct counting of the particles in an illuminated region (Tory et. al. (1992) and Lei et. al. (2001)), diffusing-wave spectroscopy (Xue et. al. (1995)), tracking the motion of individual 'tagged' particles in a suspension of otherwise index matched spheres (Tory et. al. (1992, Nicolai et. al. (1995)) and single as well as multiple sound-scattering (Cowan et. al. (2000)). It has been claimed by Segré et. al. (1997) and Nicolai and Guazelli (1995), with one significant exception of Tory et. al. (1992), that the fluctuations saturate to a size-independent value but this interpretation has been criticized by Brenner (1999). Numerical simulations by Ladd (1996) show clear evidence of size-dependence over the range of L explored, although it is argued by Segré et. al. (1997) that this was because these studies were probing scales smaller than a large screening length. Höfler (2000) pointed out that the smallest dimension of the container control the magnitude of the velocity fluctuations. If the smallest dimension is increased, the velocity fluctuations increase up to a limit and are independent of the container size.

There is also a class of experiments by Rouyer et. al. (1999), which separates the problem of hydrodynamic diffusion and non-equilibrium statistical behavior in fluidized beds from the question of whether the velocity variance diverges. This is accomplished by working with a suspension in an effectively two-dimensional geometry, i.e. with length, L and width, W much larger than the thickness, δ, and δ slightly larger than the particle size. This yields a system whose local hydrodynamics is three dimensional, so that hydrodynamic dispersion take place with long-range effects including any possible Caflisch Luke divergence screened out on lateral scales $>> \delta$. The measurements of the probability distribution of the velocity fluctuations of hyperdiffusive particle in these experiments still lack a theory. The work of Xue et. al. (1995) using diffusing-wave spectroscopy and the particle-imaging velocimetry of Segré et. al. (1997) also broadly fall in this category. But these interesting and important experiments do not specifically concern themselves with the question of the divergent velocity variance. The confined experimental geometry however, is of relevance since the development of our simulations are made based on that and the notion (Segré et al. (2001)) of an effective temperature is central to the stochastic PDE approach of Levine et. al. (1998).

2.6.3 Some theoretical approaches

Apart from the ideas involving particle or fluid inertia which experiments by Cowan et. al. (2000) seem to have ruled out pretty conclusively, there have been precisely four the-

oretical attempts to go beyond what Caflisch and Luke, CL have done. Koch and Shaqfeh (KS) (Koch and Shaqfeh (1991)) were the first to argue that a mechanism analogous to screening of the Coulomb interaction in electrolytes might work in sedimenting suspensions. They started from a microscopic statistical description of the sedimenting hydrodynamically interacting particles and showed that three-particle encounters could lead to a screening of the CL divergence. They have not, however, mentioned that independent measurements could predict whether a given suspension is screened or not. Brenner (1999) assumed the CL mechanism but questioned the evidence in favor of screening, arguing that the interpretation of the experiments by Segré et. al. (1997) are greatly complicated by the proximate walls of the container. The coarse-grained approach of Levine et. al. (1998) consists of the stochastic equations of motion for the concentration and velocity fields of a sedimenting suspension. This retains only those terms which dominate at large length scales assuming no relations amongst the phenomenological parameters other than those forced by the symmetries of the problem. The spirit is identical to those underlying theories of dynamical critical phenomena (Halperin and Hohenberg (1977)), the hydrodynamics of ordered phases (Martin et. al. (1972)) or indeed the fluctuating Navier-Stokes equations (Landau and Lifshitz (1969)).

The important difference is that sedimentation is a non-equilibrium steady state, where stationary configuration probabilities are not given by a Boltzmann-Gibbs distribution with respect to an energy function but can be obtained by solving the equations of motion.

This approach yields a phase diagram for steady sedimentation containing an 'unscreened' phase in which the velocity variance $2v$ diverges as l as observed in CL, and a 'screened' phase in which $2v$ saturates for 'L' greater than the screening length ξ. Finally, Tong and Ackerson (1998) made an intriguing observation that the model equations for sedimentation at large Pe and small Reynolds number Re are identical to those for thermal convection at large Prandtl and Rayleigh numbers. The sedimentation problem deals with the concentration field where as the convection problem deals with the temperature field. They then transcribed results from Kraichnan's mixing-length theory for Rayleigh-Bernard turbulence to argue for screening and hence, for a finite velocity variance in steady low Reynolds-number sedimentation. An important difference between Tong and Ackerson (1998) and the experiments is that the latter were undertaking with an uniform concentration, while whereas convection is driven by an imposed temperature gradient.

2.7 Non-Spherical particles

As mentioned above, many of the investigations have been made on spheres and in a reduced manner on slender bodies, (e. g. fibers) by Ramaswamy (2001) and Batchelor (1970). Ellipsoidal particles (figure 1.6), have found an application in the modeling of the blood flow Olla (1999). Fibers, on the other hand, have numerous technological applications, the paper manufacturing, transport and refining petroleum, pharmaceutical processing and environmental waste treatment.. They show orientational transition for smaller volume fractions which is characterized by the sedimentation velocity that has a

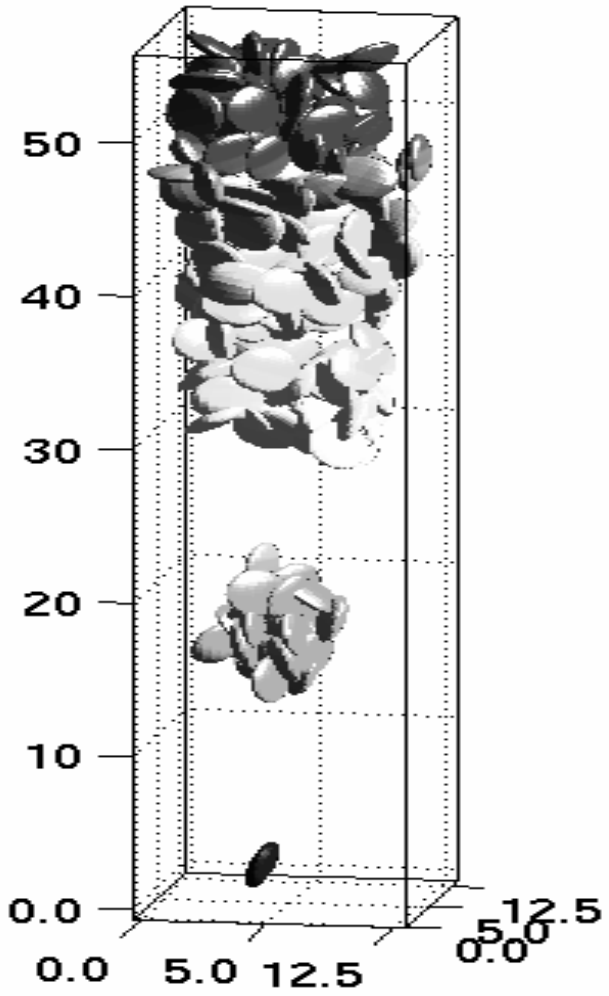

Figure 2.6: Snapshot of the oblate ellipsoids falling in a fluid. The picture shows the "cluster" formation along the falling. The ellipsoid aspect-ratio is $\Delta r = 0.4/1.5$, the distance is given in units of the larger radius, R_M and the Reynolds number is $Re = 4 * 10^{-2}$.

global maximum around the transition in stationary state, Kuusela et. al. (2003).

With this background, the investigation of the sedimentation of non-spherical particles is fundamental. An understanding of the settlement movement, orientation and spatial distribution of particles in driven flows is crucial for this task.

2.8 Overview

In this thesis I present a numerical study of the dynamics of one and many falling oblate ellipsoids particle in a viscous fluid, in three dimensions, using a constrained-force

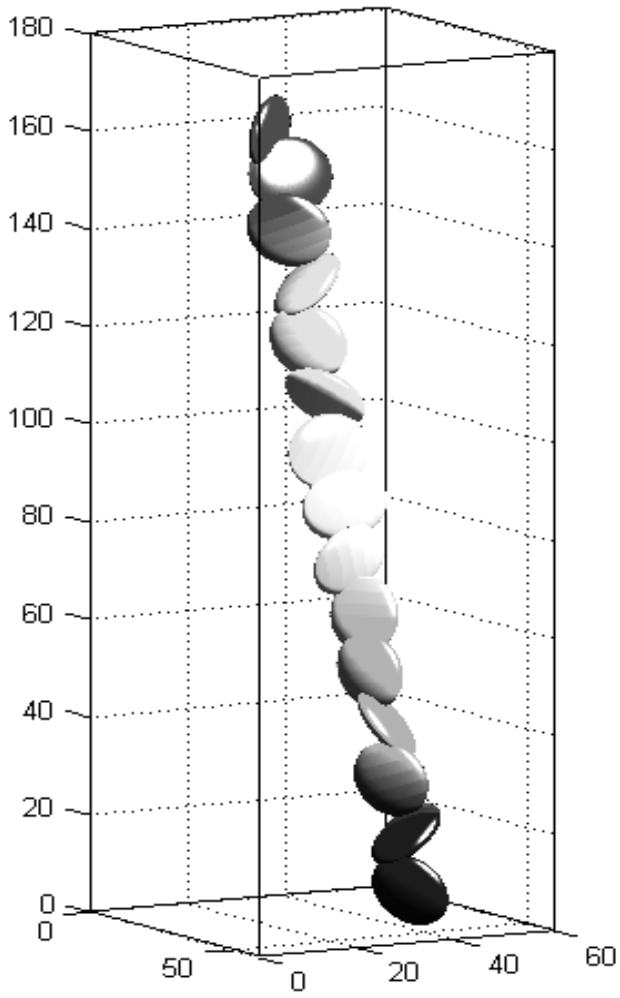

Figure 2.7: A section of a tridimensional falling oblate ellipsoid. The system size is $50 \times 180 \times 50$ the oblate aspect-ratio is $0.2/1.0$ in units of the larger ellipsoid radius. The Reynolds number is $2 * 10^{-2}$, and the ratio of the fluid density over the ellipsoid density is 3.5.

technique (Höfler and Schwarzer (2000); Höfler (2000); Kuusela et. al. (2001)), under gravity. We study the dynamical behavior for a typical downward motion, fig. 1.7, establishing the types of falling motions and finding a similarity law for regular motions. We propose a mechanism for understand the transitions between the differents types of motion. In many-particles (ellipsoids) sedimentation (figure 1.6), I study the settling velocity and the average orientation of the ellipsoids as a function of the volume fraction. We also investigate the diffusive behavior of a sedimenting ellipsoid at low and moderate Reynolds number. Finally, we show the dependence of the sedimentation dynamics of ellipsoids and spheres on the size container.

In chapter 2 we briefly present the fluid dynamical basis of the model and we explain the basic ingredients of the model. In chapter 3 we show the basic phenomenology of the falling of one oblate ellipsoid in each regime (steady-falling, periodic-oscillation and chaotic motion) of the system and we compare our results with previous works. In chapter 4 we investigate the dynamics behind each regime. For the periodic and steady-falling regime we find a similarity law derived from the invariance of the Reynolds and Froude number. In the chaotic regime the trajectory of the oblate ellipsoid is characterized by a high sensitivity to tiny variations in the initial orientation.

In chapter 5 a phase diagram is presented and compared to the results of Field et. al. (1997). The transition from oscillatory to steady-falling occurs at $Re_c = 355$, where the transient time of oscillation in the steady-falling regime tends to infinity, beyond this value the system is oscillatory. The transient time has a power law divergence at Re_c with an exponent of 0.5. The transition from steady-falling to chaotic regime becomes abrupt, for a certain value of the ellipsoid radii.

In chapter 6 we study the settling velocity and the average orientation of the ellipsoids as a function of volume fraction. We see that the settling velocity shows a local maximum at the intermediate densities unlike the spheres. The average orientation of the ellipsoids also shows a similar local maximum and we observe that this local maximum disappears as the Reynolds number is increased. Also, at small volume fractions, we observe that the oblate ellipsoids exhibit an orientational clustering effect in alignment with gravity accompanied by strong density fluctuations. The vertical and horizontal fluctuations of the oblate ellipsoids are small compared to that of the spheres.

In chapter 7 we investigate the diffusive behavior of sedimenting ellipsoids at low and moderate Reynolds number. We begin introducing the common theoretical tools used to study the diffusive behavior of sedimenting particles. We also discuss the results for ellipsoids in comparison to the equivalent spheres. Moreover, we study the behavior of the sedimenting spheres and ellipsoids under variations of the kinematic viscosity, ellipsoid density and aspect-ratio. Furthermore, we present the orientational diffusion behavior. Additionally, we show the anomalous diffusion for ellipsoids.

Finally in chapter 8 we present the dynamical behavior of sedimenting ellipsoids and spheres under variations of the container size. We study the influence on the spatial correlations as the particulate volume fraction is changed, comparing the results for ellipsoids and spheres. We also present the study of the velocity fluctuations as a function of the volume fraction. After that, we investigate the divergence of the velocity fluctuations as the container size is changed.

Chapter 3

Model

This chapter lays out the general technique used for modeling the physics of one and many sedimenting ellipsoids. We introduce the important quantities and terminologies that are employed in the rest of the thesis. In the first section we present basic results of fluid dynamics. Next, a description of fluid and particle coupling is presented. Finally, the ellipsoid contact method for the ellipsoid-ellipsoid interaction is sketched.

3.1 Navier-Stokes equations

Fluid is defined as the state of matter that cannot sustain any shear stress. For an elastic solid, the strain increases with time and attains a steady value where as, for a fluid it increases indefinitely with time. In the mathematical description of a fluid flow, the flow quantities such as velocity, pressure are assumed to vary continuously. In view of the particle nature of matter, the validity of this assumption can be questioned. If the mean free path of the molecules is comparable with the characteristic dimension of the macroscopic flow, the continuous approximation breaks down. Standing by this continuous hypothesis, one can derive the conservation of mass in the fluid flow by writing the global equation for the mass of the fluid inside a fixed volume. Consider an arbitrary volume V, fixed in a reference frame used for describing the flow of fluid and bounded by a closed surface S. At every instant of time, fluid enters and exits from this volume. The rate of change of the mass, m contained within the volume is equal and opposite to the flux leaving the boundary surface. Then we have

$$\frac{dm}{dt} = \frac{d}{dt}\iiint_V \rho_f dV = -\iint_S \rho_f \mathbf{v}\cdot\mathbf{n}dS \tag{3.1}$$

where $\mathbf{n}$ is the outward unit vector normal to the surface, S of the boundary and V is the volume. Since V is fixed we can interchange the order of integration and differentiation with respect to time. Further, by applying the Gauss's divergence theorem, we obtain:

$$\frac{\partial \rho_f}{\partial t} + \nabla\cdot(\rho_f \mathbf{v}) = 0 \tag{3.2}$$

Making an explicit differentiation of the term $\nabla \cdot (\rho_f \mathbf{v})$ and grouping we get,

$$(\frac{\partial \rho_f}{\partial t} + \mathbf{v} \cdot \nabla(\rho_f)) + \rho_f \nabla \cdot (\mathbf{v}) = 0 \tag{3.3}$$

The first term of the above equation is known as the convective derivative corresponding to the Lagrangian description and therefore we can rewrite 3.3 as

$$\frac{d\rho_f}{dt} + \rho_f \nabla \cdot (\mathbf{v}) = 0 \tag{3.4}$$

which shows conservation of mass.

3.1.1 The general equation for the dynamics of the fluid

We solve Newton's equation of motion

$$\frac{d}{dt} \iiint_V \rho_f \mathbf{v} d\tau = \iiint_V \rho_f \mathbf{f} d\tau + \iint_S [\boldsymbol{\sigma}] \cdot \mathbf{n} d\Sigma \tag{3.5}$$

where $d\tau$ is the differential volume of fluid, $d\Sigma$ is the surface element of the closed surface, S that bounds V, and $[\boldsymbol{\sigma}]$ is the tensor of all the (pressure and viscosity) forces acting on $d\Sigma$. The volume force $\mathbf{f}$ per unit mass of fluid could be the gravitational force.

The derivative d/dt is a Lagrangian derivative, evaluated in the reference frame moving with the fluid, then the product $\rho_f d\tau$ is constant, as it moves along the local velocity field of the flow. Applying Gauss divergence theorem to the second term on the right hand side

3.5

we can write equation 3.5 as

$$\iiint_V \frac{\rho_f}{dt} \mathbf{v} d\tau = \iiint_V \rho_f \mathbf{f} d\tau + \iiint_V \nabla \cdot [\boldsymbol{\sigma}] d\tau \tag{3.6}$$

Taking the limit as volume tends to zero and dividing by the value of the volume element, we obtain the local equation of motion for a particle of fluid:

$$\frac{\rho_f}{dt} \mathbf{v} = \rho_f \mathbf{f} + \nabla \cdot [\boldsymbol{\sigma}] \tag{3.7}$$

$[\boldsymbol{\sigma}]$ can be written as $[\boldsymbol{\sigma}] = [\boldsymbol{\sigma}'] - p\delta_{ij}$.

Then we have

$$\nabla \cdot [\boldsymbol{\sigma}])_i = \nabla \cdot [\boldsymbol{\sigma}']_i - \frac{\partial p \delta_{ij}}{\partial x_j} \tag{3.8}$$

Then equation 3.7 becomes

$$\rho_f \frac{d\mathbf{v}}{dt} = \rho_f \mathbf{f} - \nabla p + \nabla \cdot [\boldsymbol{\sigma}'] \tag{3.9}$$

This equation is applicable to any fluid. If we study the motion of a Newtonian fluid then we can express $\sigma^{'}$ as

$$\nabla \cdot [\boldsymbol{\sigma}'] = \mu \frac{\partial^2 v_i}{\partial x_i \partial x_j} + (\xi + \frac{\mu}{3}) \frac{\partial}{\partial x_i} \frac{\partial v_l}{\partial x_l} \tag{3.10}$$

On substituting in eq. 3.6, we obtain the equation of motion for a compressible or incompressible Newtonian fluid:

$$\rho_f \frac{\partial \mathbf{v}}{\partial t} + \rho_f (\mathbf{v} \cdot \nabla)\mathbf{v} = \rho_f \mathbf{f} - \nabla p + \mu \nabla^2 \mathbf{v} + (\xi + \frac{\mu}{3}) \nabla (\nabla \cdot \mathbf{v}) \tag{3.11}$$

If the compressibility effects are negligible in the fluid flow then $\nabla \cdot \mathbf{v} = 0$. The resulting equation is the Navier-Stokes equations:

$$\rho_f \frac{\partial \mathbf{v}}{\partial t} + \rho_f (\mathbf{v} \cdot \nabla)\mathbf{v} = \rho_f \mathbf{f} - \nabla p + \mu \nabla^2 \mathbf{v} \tag{3.12}$$

3.1.2 The dimensionless form of the Navier-Stokes equation

We can also write the Navier-Stokes equation, eq. 3.12, in terms of dimensionless parameters (that are labeled with 'primes'). Let L and U be the respective scaling factors for the spatial characteristic length (particle diameter) and velocity of the sedimenting particle. Then we have:

$$\mathbf{r}^{'} = \frac{\mathbf{r}}{L}, \mathbf{v}^{'} = \frac{\mathbf{v}}{U} \tag{3.13}$$

and

$$t^{'} = \frac{\mathbf{t}}{L/U}, p^{'} = \frac{p - p^{'}}{1/2 \rho_f U^2} \tag{3.14}$$

In defining $p^{'}$, the value of p_0 has been subtracted, which is the hydrostatic pressure. After dividing each side by $\rho_f U^2 / L$, the Navier-Stokes equation becomes:

$$\frac{\partial \mathbf{v}^{'}}{\partial t^{'}} + (\mathbf{v}^{'} \cdot \nabla^{'})\mathbf{v}^{'} = -\nabla p^{'} + \frac{1}{Re} \nabla^2 \mathbf{v}^{'} + Fr^2(-\mathbf{g}) \tag{3.15}$$

In the above equation, the inverse of the Reynolds number $Re = LU\rho_f/\mu$ associated with the flow appears as a factor of the term $\nabla^2\mathbf{v}'$. It is found that this number represents the ratio of the non-linear convective term $(\mathbf{v}' \cdot \nabla')\mathbf{v}'$ to the viscous term $\mu\nabla^2\mathbf{v}'$. We define $Fr^2 = gL/U^2$ as the Froude number. From the above equation, the velocity and pressure fields ($\mathbf{v}'$ and p') that satisfy the appropiate boundary conditions for a given problem, are of the form:

$$\mathbf{v}' = \mathbf{F}(x', y', z', t', Re, Fr) \tag{3.16}$$

$$p' = G(x', y', z', t', Re, Fr) \tag{3.17}$$

where F and G are functions that are dependent on the flow. We make use of this in Chapter 5.

3.2 Boundary conditions

The complete solution for the motion of a fluid velocity field, $\mathbf{v}(\mathbf{r}, t)$ includes both, the integration of the equation of motion of the fluid particles and the specification of boundary conditions; i.e., the value of the variables at all the boundaries of the fluid.

Boundary conditions vary depending on whether the boundary is solid or a fluid. In the case of a solid wall being a boundary, the fact that the fluid cannot penetrate into the solid requires that the component of the velocity normal to the boundary surface should be equal for the fluid and the solid:

$$\mathbf{v}_{\mathbf{solid}} \cdot \mathbf{n} = \mathbf{v}_{\mathbf{fluid}} \cdot \mathbf{n} \tag{3.18}$$

3.3 The model

The general idea of our approach, proposed by Fogelson and Peskin (Fogelson (1988)), is to work with a simple grid by resolving the fluid motion at all times and represent the particles not as boundary conditions to the fluid, but by a volume force term or Lagrange multipliers in the Navier-Stokes equations. This technique was developed in the work by Schwarzer et. al. (Höfler and Schwarzer (2000)), Höfler (2000), Kuusela et. al. (Kuusela et. al. (2001)), Wachmann, et al. (Wachmann and Schwarzer (1998)). This employs a numerical solver for the dynamical simulation of three-dimensional rigid particles in a Newtonian fluid, bounded by a rectangular container. The equation 3.12 is discretized on a regular, marker-and-cell mesh to second order precision in space. For the time evolution, we employ an operator-splitting-technique which is explicit and accurate to first order. The suspending fluid is subjected to no-slip boundary conditions at the surface of the particles. More details are presented in Kuusela et. al. (2001), Höfler and Schwarzer (2000), Höfler (2000).

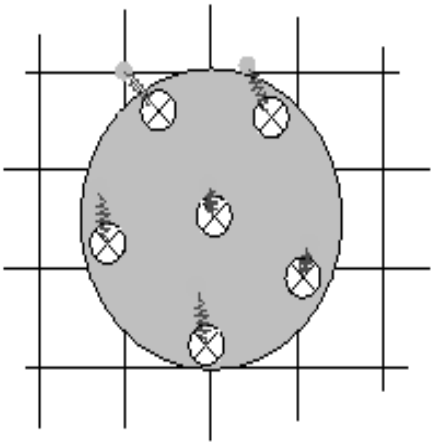

Figure 3.1: The picture shows the distribution force between particle and the fluid

An oblate ellipsoid is represented by a rigid template connected to the fluid tracer particles. This is done by the body force term, in the Navier-Stokes equation as a constraint on the fluid in order to describe the oblate ellipsoid. The force density $\mathbf{f}^c$, is chosen to be springlike. We define this force density $\mathbf{f}^c$ as:

$$\mathbf{f}^c = f^c(\mathbf{x_{ij}} + \boldsymbol{\epsilon}(\mathbf{x_{ij}})) = -k\boldsymbol{\epsilon}(\mathbf{x_{ij}}) \tag{3.19}$$

where $\mathbf{x_{ij}}$ is the displacement field of the separation between the markers i and their corresponding reference point j. The stiffness constant k, must be chosen large enough so that $\mid \boldsymbol{\epsilon}(\mathbf{x_{ij}}) \mid \ll h$, h being the size of the grid, holds for all iterations.

In general, the displacement field $\boldsymbol{\epsilon}(\mathbf{x_{ij}})$ is defined as:

$$\boldsymbol{\epsilon_i}(\mathbf{x_{ij}}^m) = \mathbf{x_{ij}}^m - \mathbf{x_{ij}}^r \tag{3.20}$$

The vector, $\mathbf{x_{ij}}^m$ is the position of a fluid tracer whose motion is determined by the local fluid velocity, i.e.,

$$\dot{\mathbf{x_{ij}}}^m = \mathbf{u}(\mathbf{x}_{ij}^m) \tag{3.21}$$

The $\mathbf{x_{ij}}^r$ are the reference points associated with the template having the shape of the physical particle:

$$\mathbf{x_{ij}}^r = \mathbf{x}_i + O_i(t).\mathbf{r}_{ij} \tag{3.22}$$

Here $\mathbf{x}_i$ is the center of mass of the template, $O_i(t)$ is the rotation matrix that describes the instantaneous orientation of the oblate ellipsoid and $\mathbf{r_{ij}}$ denote the initial positions

of the reference points with respect to the center of mass. Rotation is described by the quaternion formulation as in Allen and Tilsdesley (1987). The equations of motion of the particle template are:

$$\dot{\mathbf{U}} = \frac{\mathbf{F}}{M} \tag{3.23}$$

and

$$\mathbf{I}\dot{\mathbf{\Omega}} = \mathbf{T} \tag{3.24}$$

where M is the mass of the template particle; $\mathbf{U}$ and $\mathbf{\Omega}$ are the linear and angular velocities of the template particle, respectively; $\mathbf{I}$ is the moment of inertia of the oblate ellipsoid with only three non-zero elements, I_{11}, I_{22}, I_{33} where $I_{11} > I_{22} = I_{33}$ (Goldstein et. al. (2002)) and $\mathbf{T}$ is the torque, (Kuusela et. al. (2001), Höfler and Schwarzer (2000)). The boundary conditions near the container wall are: the normal velocity component of the fluid is zero, the walls are assumed to be impenetrable, because of a no-slip condition for the tangential component (Höfler and Schwarzer (2000), Wachmann and Schwarzer (1998)). The interaction between the oblate ellipsoid and the walls is defined through a contact force (Perram and Rasmussen (1996) and Kuusela et. al. (2001)), where the walls are treated as a particle with infinite mass and infinite radius. A velocity-Verlet integrator (Press et. al. (1992)) serves to integrate the equations of motion for the translation and a Gear-predictor integrator (Allen and Tilsdesley (1987)) for the rotation of the template:

$$\mathbf{F} = -Mg\hat{j} + \rho_f V g\hat{j} + \sum_i \mathbf{f}_i^c + \mathbf{f}_i^p \tag{3.25}$$

where $\hat{j}$ is the unit vector along the vertical w.r.t the template's center of mass $\mathbf{r}_{cm}$.

$$\mathbf{T} = \sum_i (\mathbf{x_i} - \mathbf{x_{cm}}) \times \mathbf{f}_i^c \tag{3.26}$$

with respect to the template's center of mass $\mathbf{r}_{cm}$.

The geometry of the oblate ellipsoid is characterized by Δr, its aspect-ratio which is defined as the ratio of the smallest radius, R_m to the largest radius, R_M:

$$\Delta r = \frac{R_m}{R_M} \tag{3.27}$$

We define an equivalent sphere for the oblate ellipsoid, as the sphere that has the same volume, with an equivalent radius:

$$R_{equi} = \sqrt[3]{R_m R_M^2} \tag{3.28}$$

The respective Stokes velocity:

$$v_s = \frac{2gR_{equi}^2(\frac{\rho_{ellip}}{\rho_f} - 1)}{9\nu} \tag{3.29}$$

with ρ_{ellip}, the ellipsoid density, ρ_f being the fluid density, ν the fluid kinematic viscosity and g the gravity.

We define the unit Stokes time t_s as the time needed for an isolated ellipsoid to goes over a distance of one-ellipsoid larger radius, R_M with a velocity v_s, as:

$$t_s = \frac{R_M}{v_s} \tag{3.30}$$

3.4 Contact function

There is a considerable amount of literature in which models for soft potentials between nonspherical particles (e.g., oblate ellipsoids) are employed in order to simulate the behavior of simple molecules and liquid crystals. The interest in the potential arises because it is necessary to determine the force, F_i^p due to the ellipsoid-ellipsoid contacts.

The lubrication contact theory at low Reynolds number establishes that the presence of fluid smoothly avoids the touching of ellipsoid-ellipsoid surfaces. In the algorithm these forces are captured correctly only on scales larger than the grid resolution. Since we are working with dilute systems at very low volume fraction, close encounters between ellipsoidal surfaces are rare. With the aim of restricting significant particle overlapping a repulsive force is introduced between the ellipsoids and is chosen to be proportional to their overlap. If the oblate ellipsoids are non-overlapping, the force is zero and at intermediate distances the hydrodynamic forces describing the existence of the fluid avoid the contact between the particles (Kuusela et. al. 2001).

We consider two ellipsoids labeled A and B with semi-axes a_1,b_2,c_3 and a_1,b_2,c_3, respectively. The rotational state of the ellipsoid is expressed by the sets, u_1,u_2,u_3 and v_1,v_2,v_3 of orthonormal unit vectors along the principal axis of the two ellipsoids. If the centers are at $\mathbf{r_a}$ and $\mathbf{r_b}$ respectively, the intercenter vector is defined as:

$$\mathbf{R} = \mathbf{r_a} - \mathbf{r_b} \tag{3.31}$$

and the matrices A and B are:

$$A = \sum_k a_k^{-2} \mathbf{u_k} \mathbf{u_k^T} \tag{3.32}$$

$$B = \sum_k b_k^{-2} \mathbf{v_k} \mathbf{v_k^T} \tag{3.33}$$

In the case where none of the semi-axes vanishes, these matrices have the inverses

$$A^{-1} = \sum_k a_k^2 \mathbf{u_k} \mathbf{u_k^T} \tag{3.34}$$

$$B^{-1} = \sum_k b_k^2 \mathbf{v_k} \mathbf{v_k^T} \tag{3.35}$$

Perram and Wertheim have derived the object function, $S(\lambda)$ (Perram and Rasmussen 1996) and (Kuusela et. al. 2001):

$$S(\lambda) = \lambda(1-\lambda)R^T[(1-\lambda)A^{-1} + (\lambda)B^{-1}]^{-1}R \tag{3.36}$$

$$S(\lambda) = \lambda(1-\lambda)R^T[(1-\lambda)A^{-1} + (\lambda)B^{-1}]^{-1}R \tag{3.37}$$

where λ is a parameter. $S(\lambda)$ is non-negative for $\lambda \in [0,1]$. Then the contact function $F(A,B)$ for the two ellipsoids is

$$F(A,B) = [max\ S(\lambda) \mid \lambda \epsilon [0 \quad 1]] \tag{3.38}$$

If $F(A,B) < 1$, the two ellipsoids overlap, if $F(A,B) > 1$, they do not and if $F(A,B) = 1$, the two ellipsoids are externally tangent.

Chapter 4

Phenomenology

In the preceding chapter we have presented the model of the sedimenting ellipsoids. In this chapter we will apply this model and see the common physical phenomena associated to the falling oblate ellipsoids. We will present the three phases that we found, and the terminologies that will be used in the next chapters. We also compare this model with the bidimensional one elaborated by Mahadevan. The velocity field for the fluid around the falling ellipsoid is shown and compared with the work by Belmonte et. al. (1998). We present in a qualitative way the presence of vortices in the fluid.

4.1 Trajectories of a falling oblate ellipsoid

We found three different kinds of motion in our simulations: steady-falling, side-to-side or periodic-oscillation, known as flutter (Belmonte et. al. (1998)) and a chaotic motion, which are shown in fig. 4.1. These kinds of motion are called patterns, regimes, or phases in the literature and we shall use the term phase in this thesis.

In general, the number of phases depends on the specific model and the conditions of the experimental setup. But it is possible to classify the phases into two large sets namely, a) regular and smooth oscillations and b) irregular and chaotic oscillations. For example, Tanabe and Kaneko (1994,95), identified five falling phases using a simplified bidimensional model: three regular and two chaotic. In an experimental work with dropping disks, Field et. al. (1997) reported four phases of which three were regular and one was chaotic as shown in fig. 4.2. And lastly, Belmonte et. al. (1998), observed a regular oscillatory and rotational phase in their experiments with thin strips.

In the majority of cases, the trajectories in our simulations depend strongly on the initial conditions and the properties of the system (oblate's initial orientation Θ_o, kinematic viscosity ν and the oblate aspect-ratio Δr). In order to reduce the parameter space in our system, we fix $\rho_{fluid} = 1\frac{g}{cm^3}$ and $\rho_{oblate} = 3.5\frac{g}{cm^3}$ in our simulations.

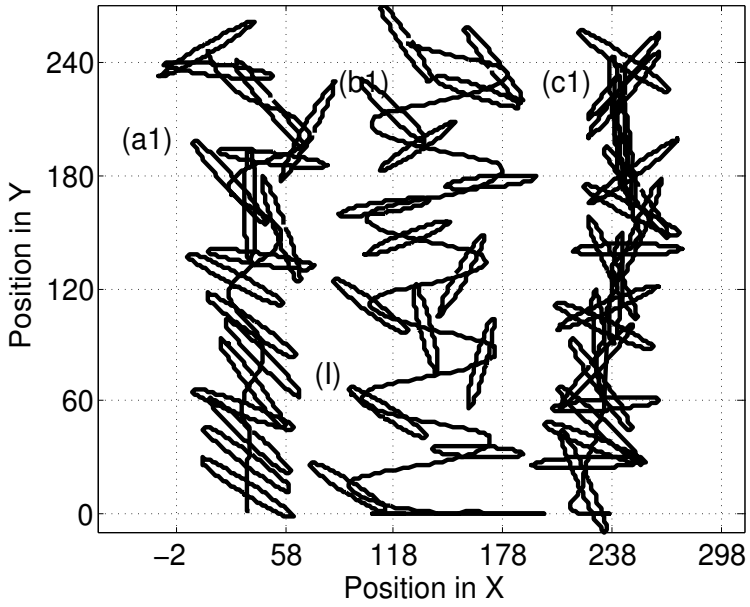

Figure 4.1: Typical falling trajectories obtained in our simulations. Figure I shows the components $Y(vertical) - X(horizontal)$ in the steady-falling regime, $(a1)$, with initial conditions $\theta_o = 26.6^0$, $\Delta r = 0.25$, $\nu = 0.033$ and $(a) h_o = 240$; $(b1)$ periodic-oscillation with initial conditions: $\nu = 0.025$, $h_o = 240$, $\Delta r = 0.133$ and $\theta_0 = 63.4^o$. $(c1)$ chaotic motion, with initial conditions $h_o = 240$, $\Delta r = 0.25$, $\nu = 0.033$ and $(a) \theta_0 = 26.6^o$.

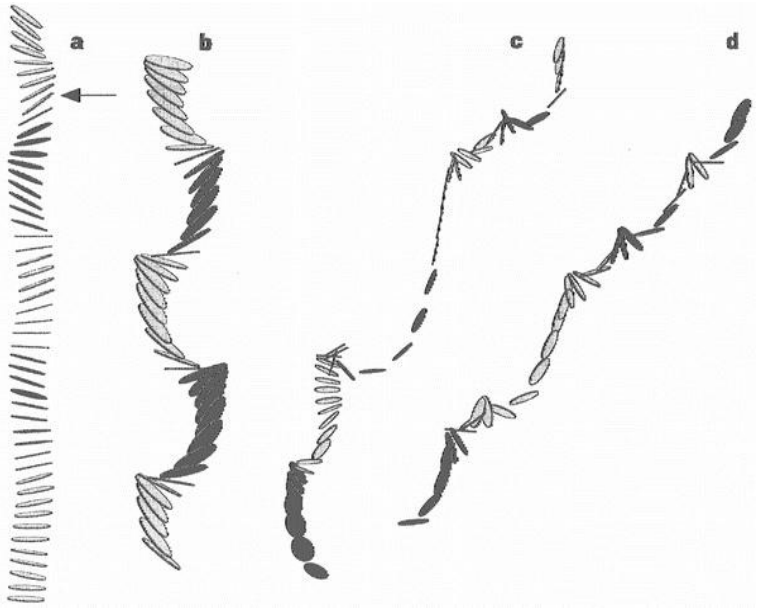

Figure 4.2: Trajectories of falling disks, presented in the work by Belmonte et al, (1998). The images were obtained from the side by using a video camara. The trajectory in (a) corresponds to the steady-falling regime, (b), periodic-oscillating motion, (c) chaotic motion and (d) the tumbling motion.

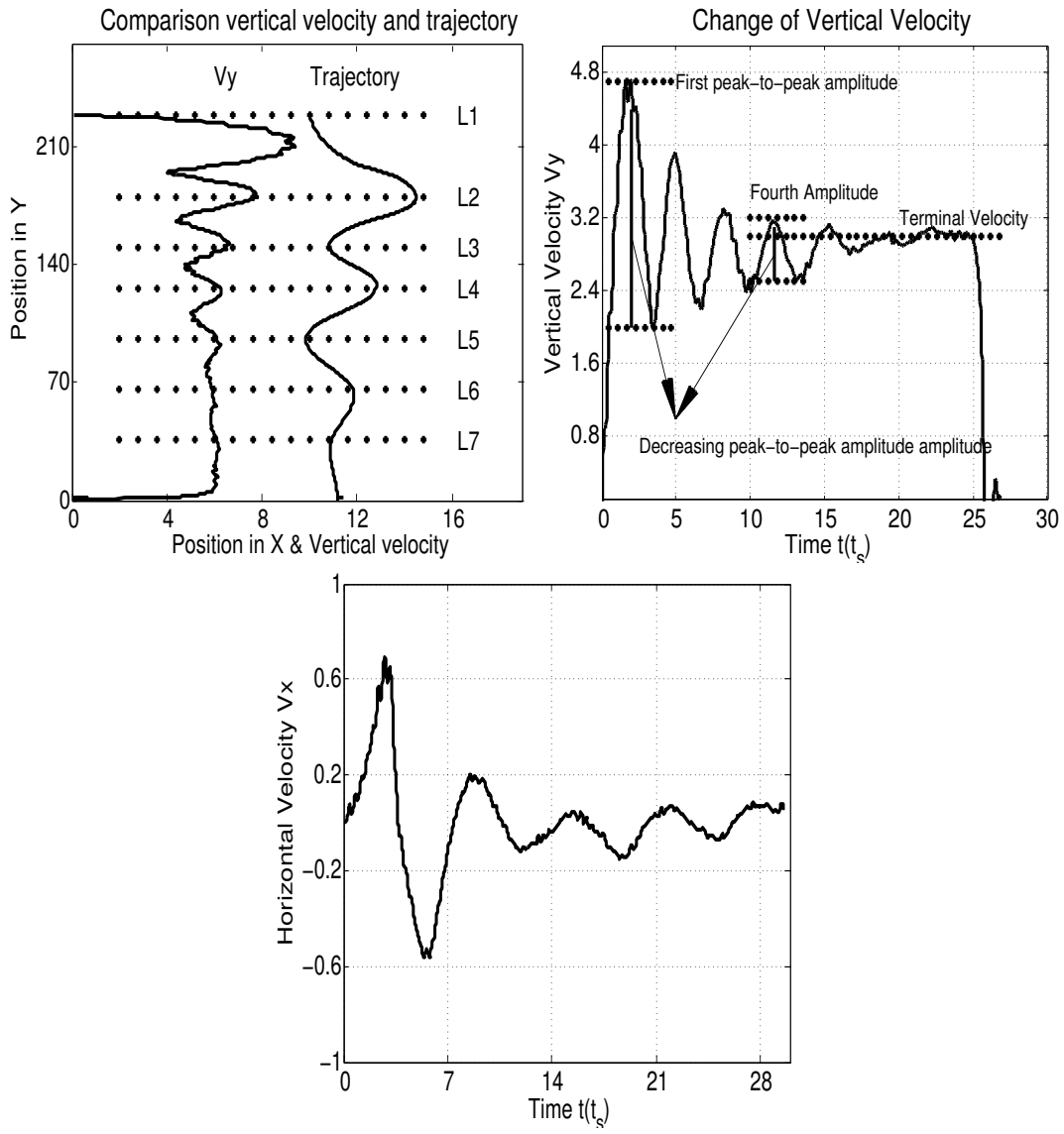

Figure 4.3: (Left) Comparison between the vertical velocity and the spatial trajectory at the same height. (Right) Decreasing amplitude of the vertical velocity. Initial conditions of the system are $\theta_o = 26.6^0$, $\Delta r = 0.25$, $\nu = 0.033$. Falling initial height $h_o = 228$ in the steady-falling regime.

4.2 Steady-falling oblate ellipsoid

When the ellipsoid begins to fall, the vertical velocity is characterized by a damped wavering (transient oscillation) in time resembling the behavior of a damped oscillator (Goldstein et. al. (2002)). At a very long time, the vertical component of velocity becomes constant. The amplitude of the vertical component of velocity decreases as the oblate ellipsoid approaches the bottom of the container fig. 4.3. The vertical trajectory fig. 4.3 (right), also shows the damped wavering. This wavering in the trajectory curve is composed of successive turning points. Each one of them, in turn, corresponds to points

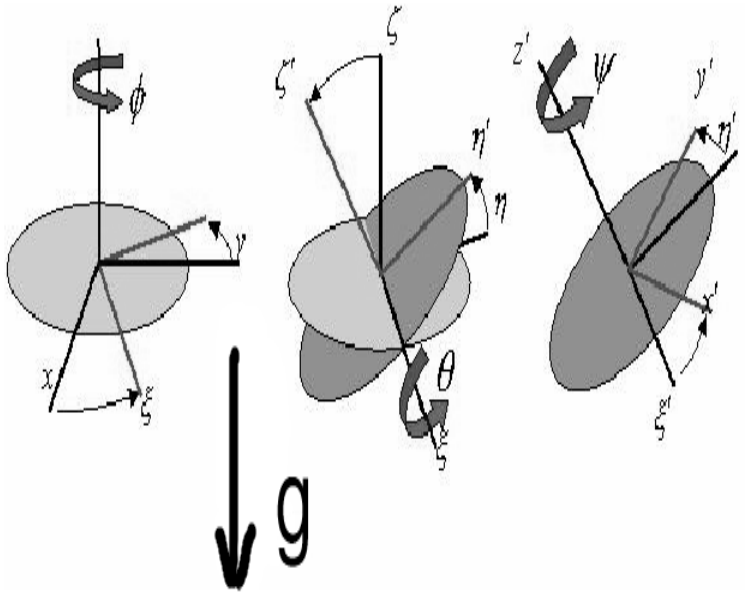

Figure 4.4: Euler angles ϕ, θ and ψ used for the description of the oblate's orientational behavior.

where the rate of change in the vertical velocity is zero. This vanishing value in the rate of change of the vertical velocity is evident in figure 4.3 (left), by the intersection of the horizontal lines L2, ... L5, with vertical velocity. There is an interesting relation between the number of turning points in the trajectory and the vertical velocity (see fig. 4.3, left). For every two successive turning points in the vertical trajectory there are four turning points in the vertical velocity. If a characteristic length is associated with the vertical trajectory, then the characteristic length corresponding to the vertical velocity is reduced. The horizontal components of the velocity follow a similar behavior as the vertical ones and in general they have regular oscillations (see fig. 4.3, bottom).

The oblate's orientation is described through the three rotational degrees of freedom, called the Euler angles, fig. 4.4. We present the time evolution of the angle between the oblate's normal and the vertical direction. This we call the vertical orientation, fig. 4.5 (top). $\Theta = 0$ implies that the oblate's principal axis will be parallel to the container's bottom fig. 4.5 (bottom). At the beginning of the movement, there is a large angular change of the oblate's normal with the vertical, $\Delta\Theta$ fig. 4.5 (bottom), which is characterized by a large peak-to-peak amplitude Θ_{p-p}. in fig. 4.5 we illustrate the definition of the peak-to-peak amplitude as the distance between successive turning points, which decreases as the oblate sinks. In the steady-falling regime, both the peak-to-peak amplitude, Θ_{p-p} and the change $\Delta\Theta = \Theta_f - \Theta_i$, decays as the oblate approaches the bottom of the container. The oblate tends to align its major axis along the vertical(Huang et. al. (1998)) having a very low resistance to its descent in the fluid acquiring the terminal velocity fig. 4.3 (top).

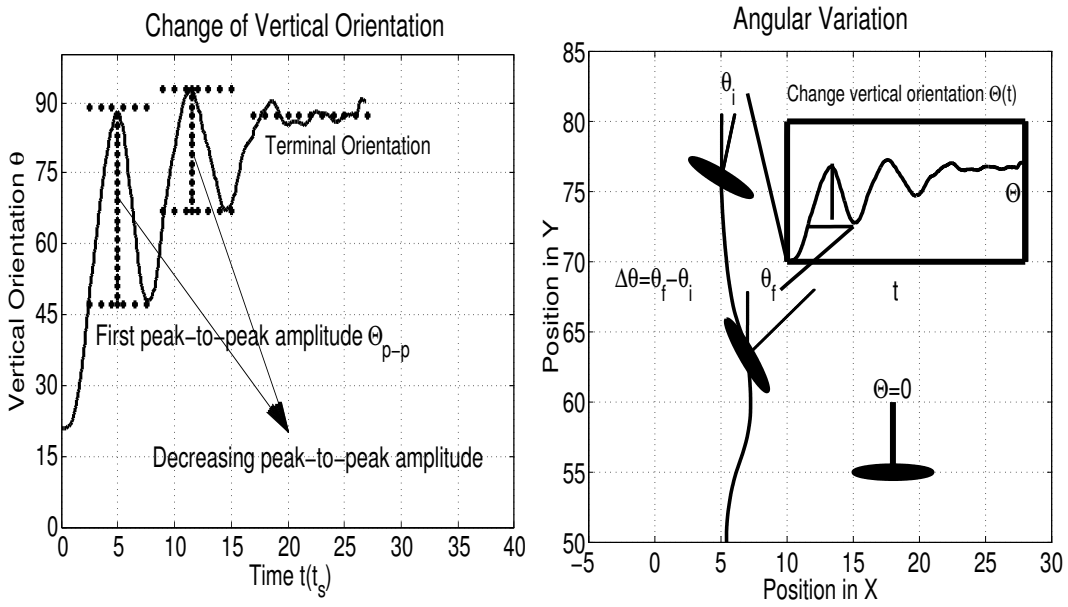

Figure 4.5: (left) Decreasing peak-to-peak amplitude in the angular oscillation. (right) Angular change $\Delta\Theta$ along a segment of the vertical trajectory. Initial conditions of the system $\theta_o = 26.6^0$, $\Delta r = 0.25$, $\nu = 0.033$ and $h_o = 228cm$.

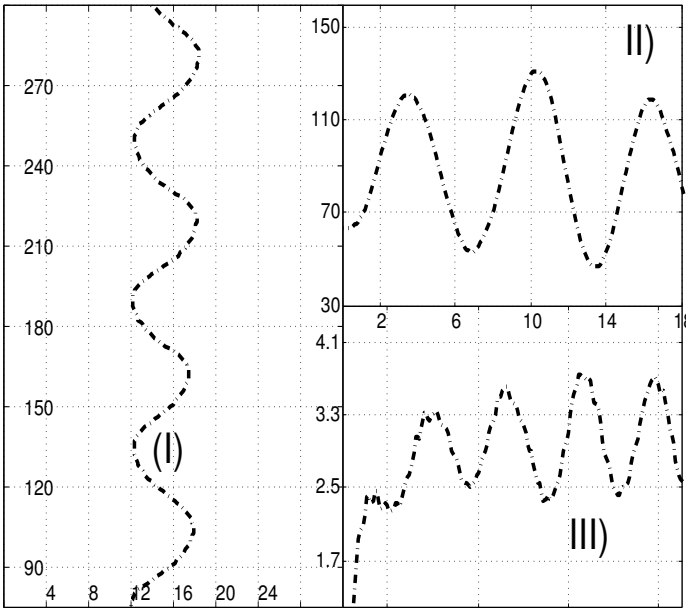

Figure 4.6: Initial conditions $h_o = 230$, $L_x \times L_z = 25 \times 25$, $\Delta r = 0.133$, $Re = 435$. Initial orientation $\Theta_0 = 63^o$. I) Vertical trajectory II) The vertical velocity. III) The vertical orientation.

4.3 Oscillatory oblate ellipsoid

In the oscillatory phase, the ellipsoid is characterized by a regular oscillation in all the dynamical variables. We observe such a behavior in our simulations at small kinematic

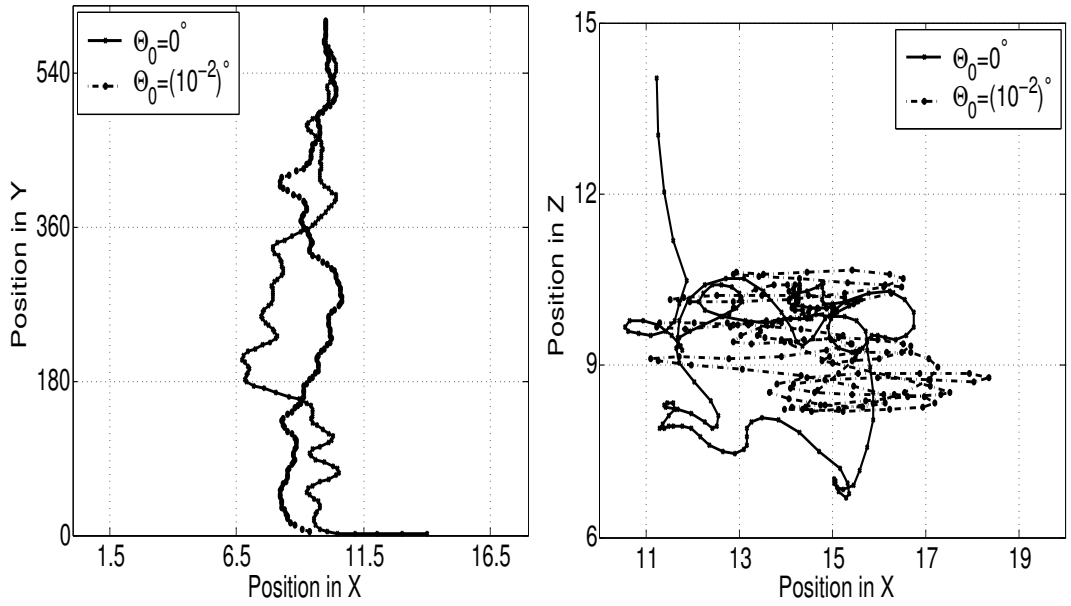

Figure 4.7: The left picture shows the change in the vertical trajectory when the initial orientation changes $\Delta\Theta_0 = 10^{-2}$. The right picture shows the horizontal components. The initial conditions $h_o = 640$, $L_x \times L_z = 25 \times 25$, $\Delta r = 0.43$, $Re = 225$.

viscosity and small aspect-ratios. In fig. 4.6 we show the ellipsoid's vertical trajectory, velocity and orientation. This oscillatory phase has been studied experimentally by Belmonte et. al. (1998). This phase has a distinctive character that the period of oscillation of the vertical velocity is half the period of oscillation of the vertical orientation. Our simulation agrees very well with the experiment which will be discussed in the fourth section of chapter 4.

4.4 Chaotic oblate ellipsoid

We observe chaotic behavior for variations in the ellipsoid's initial orientation as shown in fig. 4.7. The fig shows the prominent change in the vertical and horizontal trajectories as the initial orientation changes by the order of 10^{-2}. In our simulations the chaotic phase has been found for large aspect-ratios eq. 3.28 and for all Reynolds numbers. It is important to point out that the sensitivity to small variations in the initial conditions of falling bodies (in our case the ellipsoidal orientation Θ_o) has not been reported neither by simulations, theory nor by experiments until now.

4.5 Comparison with Mahadevan´s model

As mentioned in chapter 1, there are several models (Tanabe and Kaneko (1994,95),Mahadevan et. al. (1995) and Mahadevan (1996)) that have given good insight to the prob-

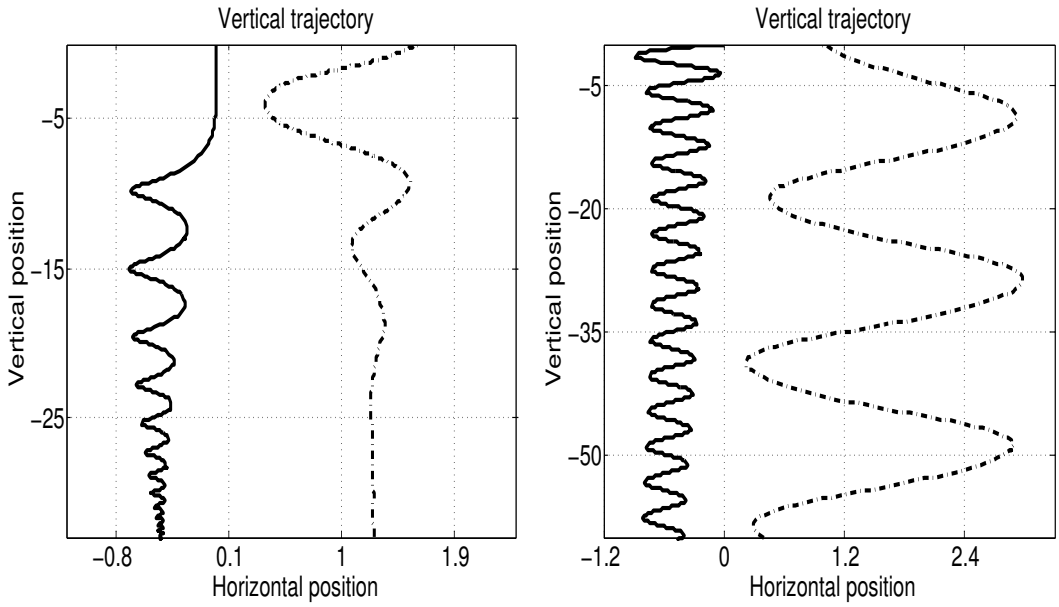

Figure 4.8: Steady-falling initial conditions $\Delta r = \beta = 0.25$, $\alpha = 0.29$, $\nu_1 = 0.1$,$\nu_2 = 0.6$,$\nu_3 = 0.7$, $\nu_i = 0.0$, $\lambda = 0.006$, $\Theta_o = 26.6^o$. For the oscillatory regime: $\Delta r = \beta = 0.25$, $\alpha = 0.29$, $\nu_i = 0.033$, $\nu_i = 0.0$, $\lambda = 6 * 10^{-7}$, $\Theta_o = 90^o$. The solid and dotted lines show Mahadevan's and our results, respectively.

lem. We use a simplified model formulated by Mahadevan (1996) that offers a good qualitative comparison to our simulations in the oscillatory and steady-falling phase. The absence of quantitative agreement has to be understood in terms of the difference between the two models. Mahedevan describes the motion of a falling strip of paper in an infinite sized cylinder, where the cylinder axis is assumed to be perpendicular to the vertical. The system is assumed to be bidimensional with an incompressible fluid in a gravitational field. The viscosity is taken into account in terms of the generalized Rayleigh dissipation function. This work is a continuation of the method used by Kelvin and Kirchhoff and applied also by Lamb (1932), whose the central approach consisted in ignoring the vortices and assuming that the fluid has zero viscosity. The new equations become complex since there are 20 newly 'added mass' terms (Lamb (1932), Mahadevan (1996)). In our case, we have a three dimensional model with boundaries as explained in chapter 2.

The equations of motion for this model are solved by using Runge-Kutta fourth order integrator and we use the initial conditions for which steady-falling and oscillatory regimes are observed, fig. 4.1. The results are shown in fig. 4.8.

4.6 Vortex

The vortex production is an important part of the fluid dynamics that must be taken into account in the formulation of a theory for falling bodies. Willmarth et. al. (1964) made a pioneering work where dye-ladden disks were dropped into water and vortices were

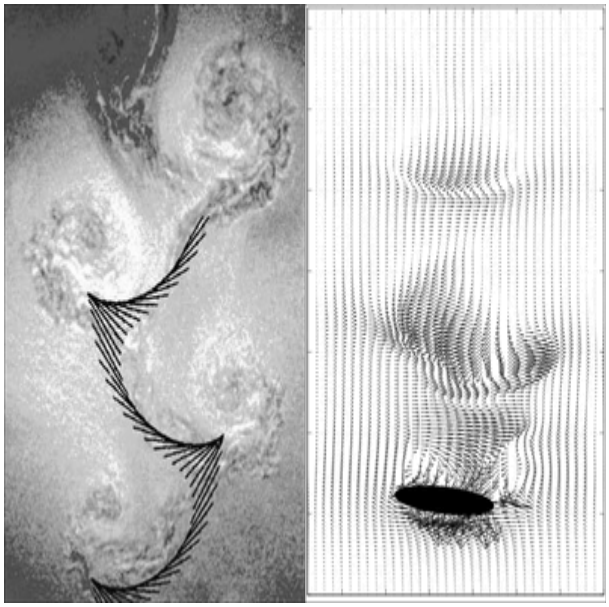

Figure 4.9: The right picture shows the vortex structure of the vertical and horizontal components of the fluid velocity field (u, v) generated by the falling oblate with a diameter 3.2 in a container of $200 \times 30 \times 30$ and Reynolds number, $Re = 128$, aspect-ratio, $\Delta r = 0.5$. The left picture shows shedding vortices reported by Belmonte et. al., ref.[12], for a falling strip.

clearly observed. In our simulations the falling ellipsoid generates shedding vortices in the fluid along its trajectory as shown in figure 4.9 (right).It shows the fluid velocity field around the oblate and the vortex is localized just in the region above the oblate and where it experiences a large angular change, $\Delta\Theta$ as shown in fig. 4.5 (top). The Reynolds number calculated from the oblate's diameter and terminal velocity, $Re = 128$. We point out that the vortex is obtained also in the work by Belmonte et al (Belmonte et. al. (1998)) where a shedding vortex is created by the zigzag motion of the falling strip as shown in the left of figure 4.9.

A systematic study of the boundary layer of the ellipsoid is not presented in the thesis and it will remain as a future work.

4.7 Conclusions and Outlook

The motion of a single oblate ellipsoid settling in a fluid in a three dimensional container has been studied. We found three basic regimes for the dynamics of the system (steady-falling, oscillatory, and chaotic). We found that our results are in good qualitative agreement with the simplified model proposed by (Mahadevan (1996)). The same initial conditions have been used in our work in the study of oscillatory and stead-falling regimes. More work has to be realized in future in order to understand the role of the fluid pressure and velocity fields better.

Chapter 5

Phases

In this chapter we investigate the dynamics of the phases introduced in the previous chapter. We explore each phase by changing different parameters in the system. We introduce some important concepts and definitions which we will use in the next chapter. In the first section, we discuss the steady falling phase when the initial height of the fall, aspect ratio of the ellipsoid and the kinematic viscosity are changed. Next, we depict the oscillatory phase. Furthermore, we study the effect on the dynamics due to changes in the initial orientation of the ellipsoid. A comparison with the experiments by Belmonte et. al. (1998) has been made and our simulations agree quite well with the experiments. Finally, we present the chaotic regime, which is highly sensitive to the change in the initial orientation of the ellipsoid, as shown in the Lyapunov exponent.

5.1 Steady-Falling Phase.

5.1.1 Change in the initial falling height.

Figure 5.1(I), shows the trajectories for different initial falling heights by fixing all other parameters. It is evident from the figure that there is no change in the peak-to-peak amplitude. For all the heights, the trajectories behave like that of a damped oscillator.

In fig. 5.1(II), we see that the ellipsoid approaches the same terminal velocity independent of the falling height, at the same time. Also, the vertical velocity sharply converges to zero as the oblate touches the bottom of the container which is independent of the falling height.

Figure 5.1(III) shows the vertical orientational behaviour of the ellipsoid with the change in the initial falling height. For all the trajectories shown in fig. 5.1(I), we see in fig. 5.1 (III) that the orientation of the ellipsoid offers minimum resistance against the fluid, which is seen by the semi-major axis getting aligned with gravity.

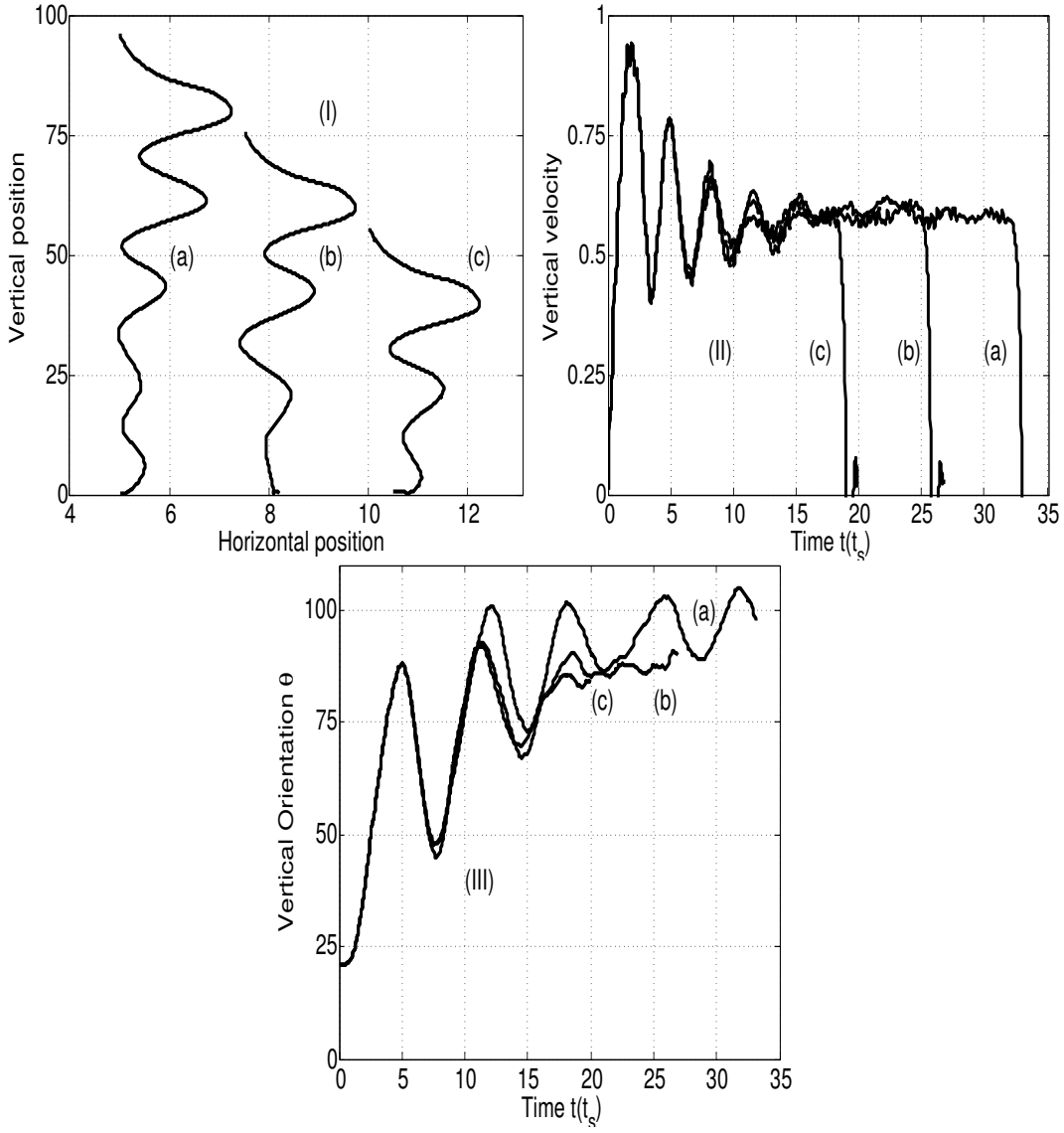

Figure 5.1: Initial conditions of the system. $\theta_o = 26.6^0$, $\Delta r = 0.25$, $\nu = 0.033$. Each Trajectory has different initial height $(a)h_o = 96$, $(b)h_o = 76$, $(c)h_o = 56$. I) The spatial trajectory in the vertical plane. II) Vertical velocity vs. time. III) Vertical orientation vs. time.

5.1.2 Dependence on the kinematic viscosity.

In this section, we study the dynamics of the steady-falling ellipsoid as the kinematic viscosity is changed. The ellipsoid starts its swinging motion with a given initial orientation, $\theta_0 = 26.6^o$. It glides downwards and to the side acquiring some amplitude, while the kinematic viscosity ν acts, thereby, reducing the subsequent amplitudes of oscillation as shown in fig. 5.2(I).

Fig. 5.2(I, II, III) show the trajectory, vertical and horizontal velocities and the vertical orientation of the ellipsoid for different kinematic viscosities, respectively. Curve a with

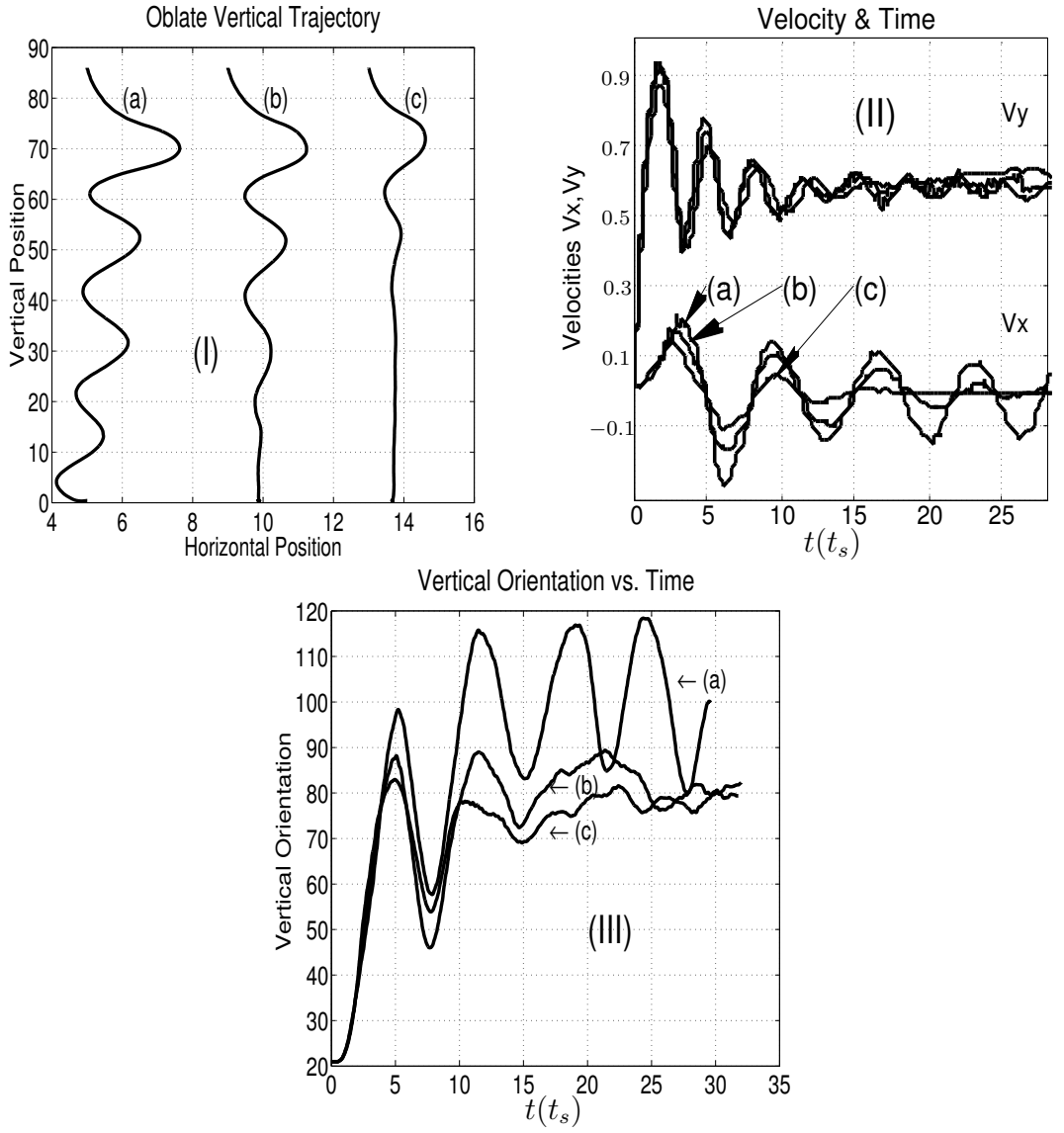

Figure 5.2: Initial conditions in the system. $\theta_o = 26.6^0$, $h_o = 80$, $\Delta r = 0.25$. Each trajectory has a different kinematic viscosity $(a)\nu = 0.025$, $(b)\nu = 0.033$, $(c)\nu = 0.100$. (I) Projection of the trajectory in the vertical plane. (II) Vertical (top) and horizontal (bottom) velocities vs. time. (III) Vertical orientation vs. time .

$\nu = 0.025$, curve b with $\nu = 0.033$ and curve c with $\nu = 0.1$. We observe from all the three plots that as viscosity increases, the attenuation becomes stronger thereby behaving like a damped harmonic oscillator.

The attenuation in the amplitude of the vertical velocity with time and the time period between two consecutive turning points are not very different from each other as the viscosity changes. Also, we see that both the horizontal and vertical velocities converge to the same value (eg. $v_x \approx 0$ and $v_y \approx 0.6$) for all the values of viscosity.

This strong attenuation for large viscosity is high in the horizontal component of the

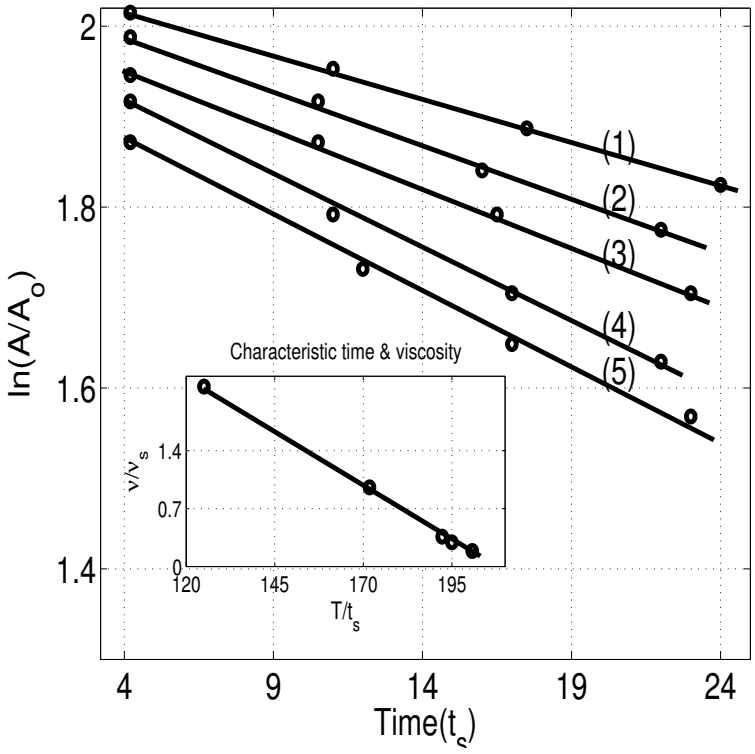

Figure 5.3: Initial conditions of the system. $\theta_o = 26.6^0$, $h_o = 220$, $\Delta r = 0.15$. In the figure each line shows the decreasing logarithmic amplitude of oscillation against time for different values of kinematic viscosity $\nu_1 = 0.04$, $\nu_2 = 0.07$, $\nu_3 = 0.08$, $\nu_4 = 0.2$ and $\nu_5 = 0.5$. In the inset we plot the characteristic time τ of each line vs the kinematic viscosity.

velocity as seen in the figure. This can be explained by the fact that the interaction between the walls and the oblate is less when the fluid is less viscous Brenner (1961). This is also true for large angular variations $\Delta\Theta$ in fig. 5.2(II) c for small values of viscosity.

In fig. 5.2 (III) we see the orientational behaviour as the viscosity changes. The first peak-to-peak amplitudes are nearly the same for all viscosities. For $\nu = 0.025$ the subsequent peak-to-peak amplitudes approach a constant value of $\Theta_{p-p} \sim 15^o$ while for higher viscosities, the oscillations get damped and the ellipsoid reaches a constant orientation. We also observe that the final orientation of the ellipsoid gets aligned with gravity.

Figure 5.3 explains that the amplitude of oscillation decays exponentially with time which is revealed by the log linear plot. The dimensionless characteristic time, $\frac{\tau}{t_s}$ decays linearly with the dimensionless kinematic viscosity, $\frac{\nu}{\nu_s}$ as shown in the inset of figure 5.3. The solid line in the inset shows a linear fit with equation, $\frac{\tau}{t_s} = -0.03\frac{\nu}{\nu_0} + 5.5$. The figure clearly shows that viscosity plays the role as a damping factor that determines the decay rate of the vertical velocity and position.

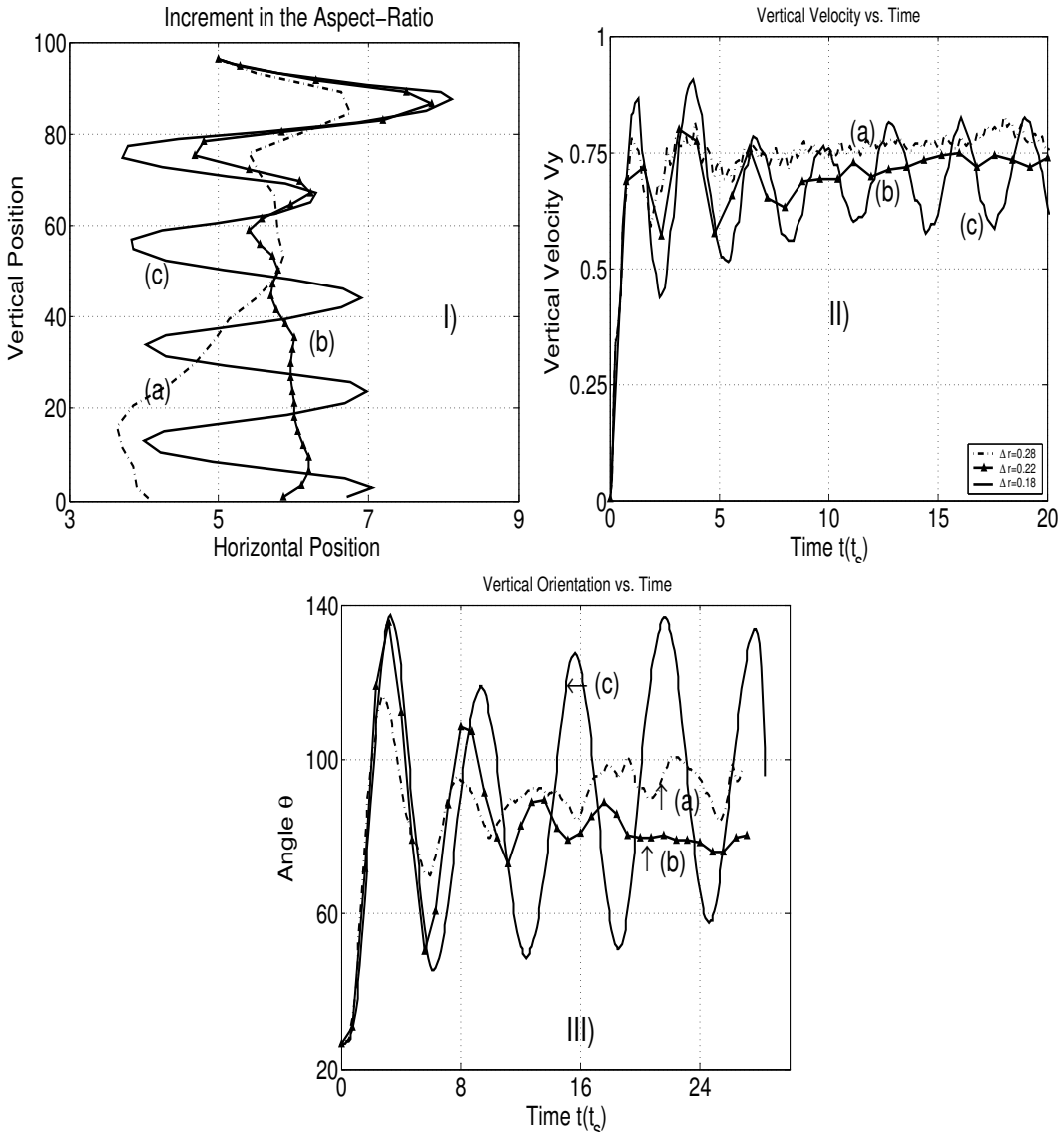

Figure 5.4: Initial conditions of the system. $\Theta_o = 26.6^0$, $h_o = 96$, $L_x \times L_y \times L_z = 10 \times 100 \times 10$, $\nu = 0.033$. Each trajectory has different aspect-ratio $(a)\Delta r = 0,29$, $(b)\Delta r = 0,22$, $(c)\Delta r = 0,18$. I) Trajectory for the vertical plane. II) Vertical velocity vs. time. III) Vertical orientation vs. time.

5.1.3 Change in the ellipsoid aspect-ratio.

When the ellipsoid begins to fall, it gains a large amplitude of oscillation. The trajectory (c), plotted in the figure 5.4 I, is for an ellipsoid with aspect ratio, Δr=0.18. We see an oscillatory trajectory characterized by a constant peak-to-peak amplitude of 3. As the aspect ratio is increased to 0.22, i.e., trajectory (b) in the figure, shows a steady falling behavior. If the aspect ratio is further increased, the trajectory shows irregular oscillations. At the beginning of the fall, the ellipsoid with large aspect ratio (trajectory a), shows a rapid damping amplitude in the first half of the trajectory but in the second half, doesn't

show any steady falling behavior, instead changes abruptly into a non-stationary state.

In figure 5.4(I), for all trajectories, the first amplitude, A_0 decreases from 3.0 to 1.8 as the aspect ratio, Δr increases from 0.18 to 0.29.

As the aspect-ratio, Δr is increased from 0.18 to 0.29, the oblate's area becomes small (minor axis of the oblate is fixed in our simulations) thereby providing less resistance to the fluid. Therefore, the final vertical velocity decreases as the aspect-ratio is increased, fig. 5.4II. Also as the aspect-ratio is increased the peak-to-peak amplitude of the vertical velocity decreases.

The peak-to-peak amplitude for the vertical orientation Θ_{p-p} increases when the aspect-ratio decreases or the oblate's area increases. For $\Delta r = 0.29$ the peak-to-peak amplitude is $\Theta_{p-p} = 15^o$, fig. 5.4 (IIIa), and much smaller compared to $\Theta_{p-p} = 70^o$, fig. 5.4 (IIIc), for $\Delta r = 0.18$. In all cases the oblate at the end orients vertically fig. 5.4 (III). As the ellipsoid aspect ratio, Δr increases, the system transits from regular to irregular dynamics which will be discussed in detail in chapter 5.

5.2 Periodic Phase.

We find periodic behavior for smaller kinematic viscosity ($\nu_2 = 0.025 \rightarrow Re = 480$) and smaller aspect-ratio ($\Delta r = 0.133$). The dynamics of the falling ellipsoid is governed by inertial effects. In figure 5.5 (I), we show the transition from a quasi-periodic, or a long steady-falling trajectory ($\nu_1 = 0.100$), to a periodic behavior fig. 5.5 (I,$\nu_2 = 0.025$), when the kinematic viscosity is varied from $\nu_1 = 0.1$ to $\nu_2 = 0.025$. The trajectory presented in fig. 5.5I, with kinematic viscosity $\nu_2 = 0.025$ has a wave length of 20.

The vertical velocity shown in fig. 5.5 (II), has the same transition from a long steady-falling regime with a final average velocity of 3.0 to the periodic regime where the velocity has a oscillation period of 3.3.

The vertical orientation shown in fig. 5.5 (III) has also the same transition from a long steady-falling regime to periodic behavior with a period of 6.6 s, and the angular values oscillate around $\Theta_0 = 90^o$ with angular peak-to-peak amplitude $\Theta_{p-p} = 60^o$.

The decreasing in the kinematic viscosity, for a much smaller aspect-ratio $\Delta r < 0.1$, takes the system from steady-falling to oscillatory phase. We will investigate this transition in chapter 5.

5.2.1 Change in the initial orientation

In this section, we investigate the periodic phase with different initial orientations. The corresponding trajectories are shown in fig. 5.6(I) for $\Theta_0 = 26^o$ and for $\Theta_0 = 90^o$ and the peak-to-peak amplitudes are 2.3 and 0.4, respectively and show an oscillatory

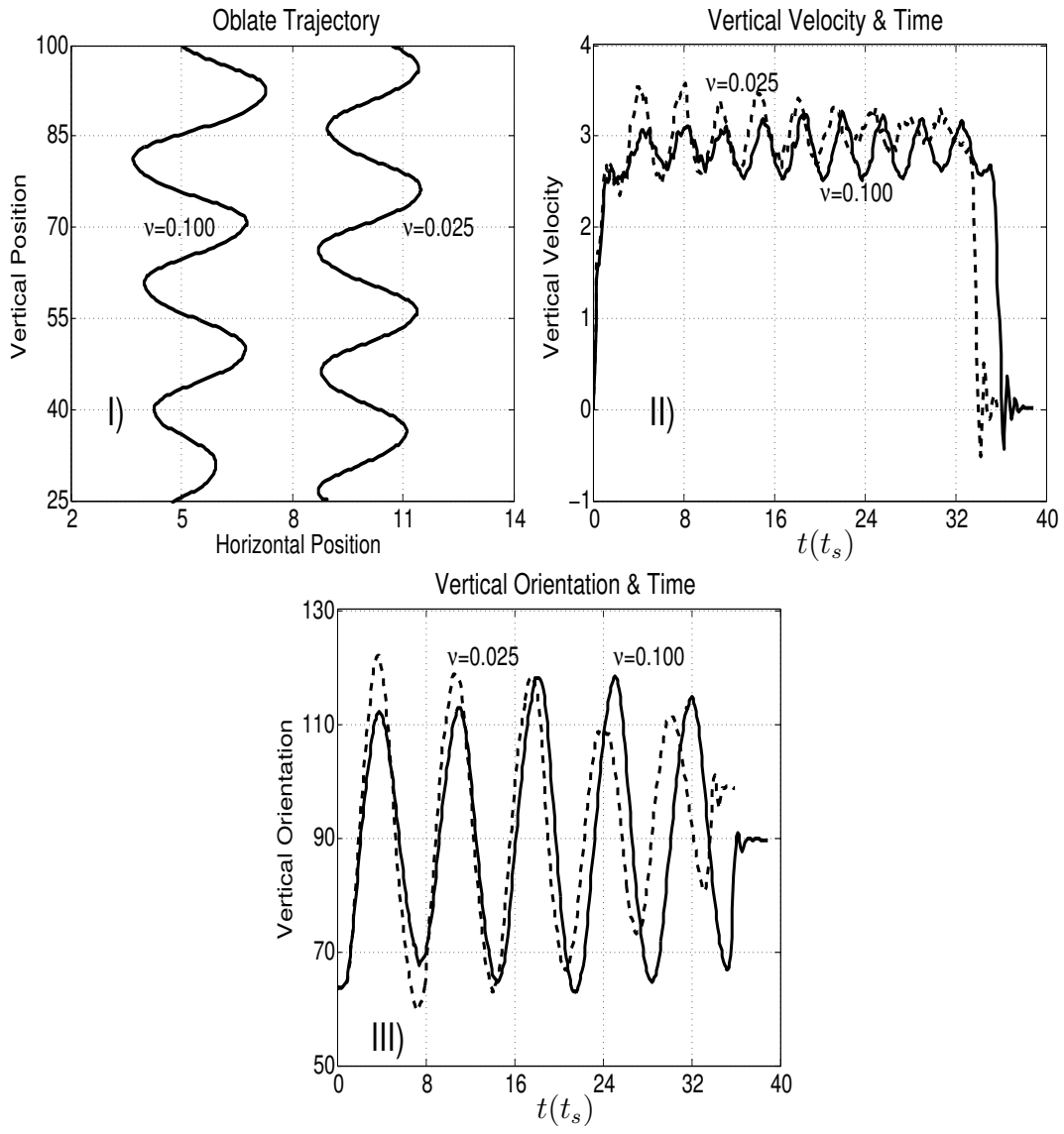

Figure 5.5: Trajectories generated for $\nu_1 = 0.100$, $\nu_2 = 0.025$. (I) Trajectory in vertical and horizontal position. (II) Vertical orientation Θ vs time. (III) Vertical velocity v_y vs time. The initial conditions are $h_o = 96$, $\Delta r = 0.133$, $\theta_0 = 63.4^o$.

behavior. The peak-to-peak amplitude of the oscillation in the trajectory vertical velocity and orientation fig. 5.6 (I,II,III) decreases as the initial angle of orientation increases.

The final vertical velocity and orientation for all the three initial orientations is on an average 0.6 and 85^o, respectively. This means that the average limiting values of the vertical velocity and orientation are not affected by the variation of the initial orientation Θ_o.

We observe a large peak-to-peak amplitude of oscillation in the vertical velocity and vertical orientation, equal to 1.0 and 70^o, respectively, with an initial orientation, $\Theta_0 = 26^o$ and it reduces as the oblate's initial orientation, Θ_0 tends to 90^o.

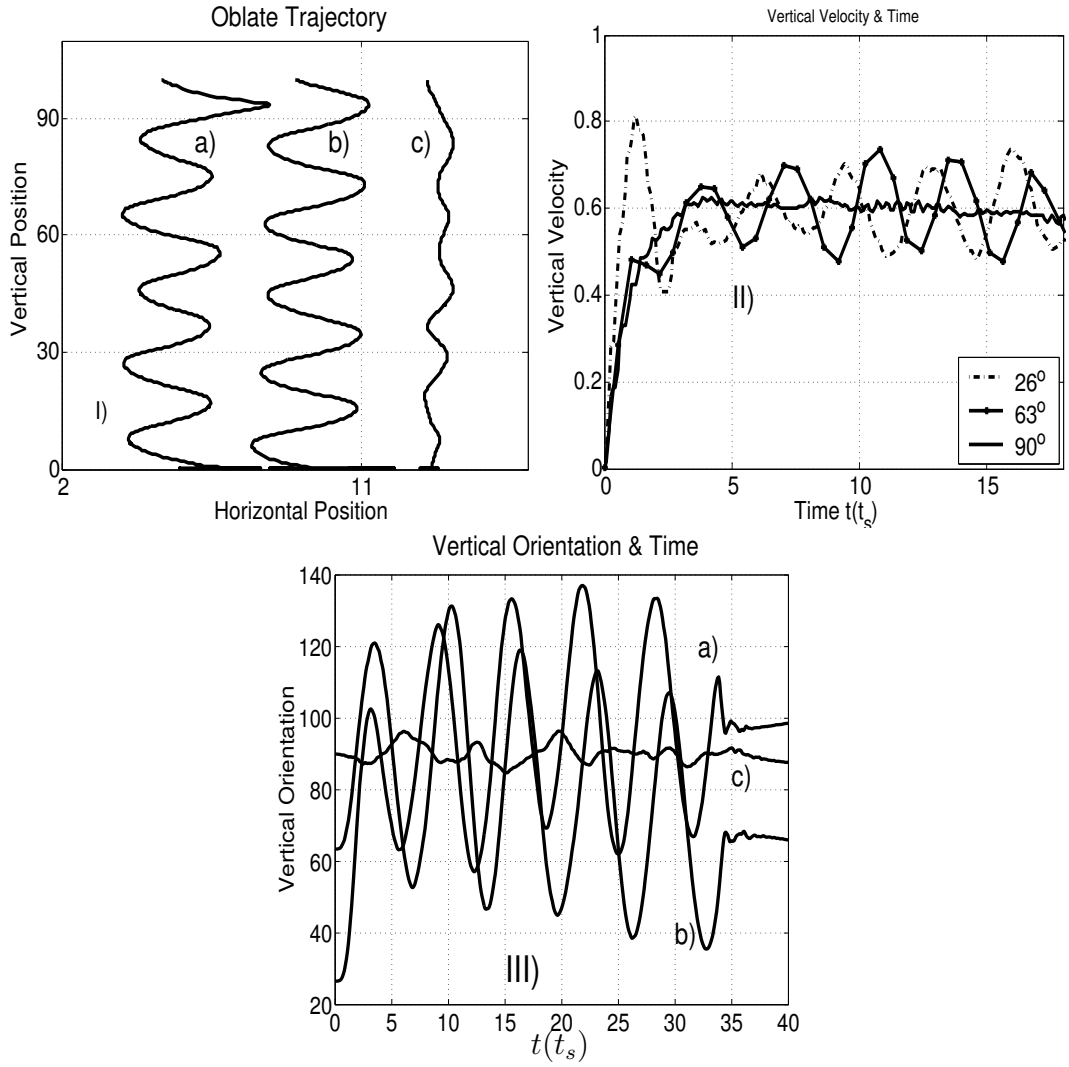

Figure 5.6: I) Trajectories for three initial orientations. (a) $\Theta_0 = 26^o$ (b) $\Theta_0 = 63^o$ (c) $\Theta_0 = 90^o$. II) The corresponding vertical velocities. III) The vertical orientations. Initial conditions $h_o = 100$, $L_x \times L_z = 10 \times 10$, $\Delta r = 0.133$, $Re = 435$.

5.2.2 Comparison with Belmonte's results.

In this section, we compare our results with Belmonte's results. Figure 5.7(a) (simulation) shows the time dependence of the vertical orientation with $\nu_2 = 0.025$ and the value of the peak-to-peak amplitude is $\Theta_o = 60^o$.

The vertical velocity as shown in fig. 5.7(b) (simulation) reaches its maximum value 3.6 as Θ approaches Θ_{max} thereby, showing a minimum drag. The minimum vertical velocity $v_y = 2.5$ is achieved at $\Theta_{min} \sim 70^o$.

The butterfly shaped curve (fig. 5.7(b)) was also measured in the experimental work by Belmonte et. al. (1998) in which the vertical orientation Θ oscillates with twice the period

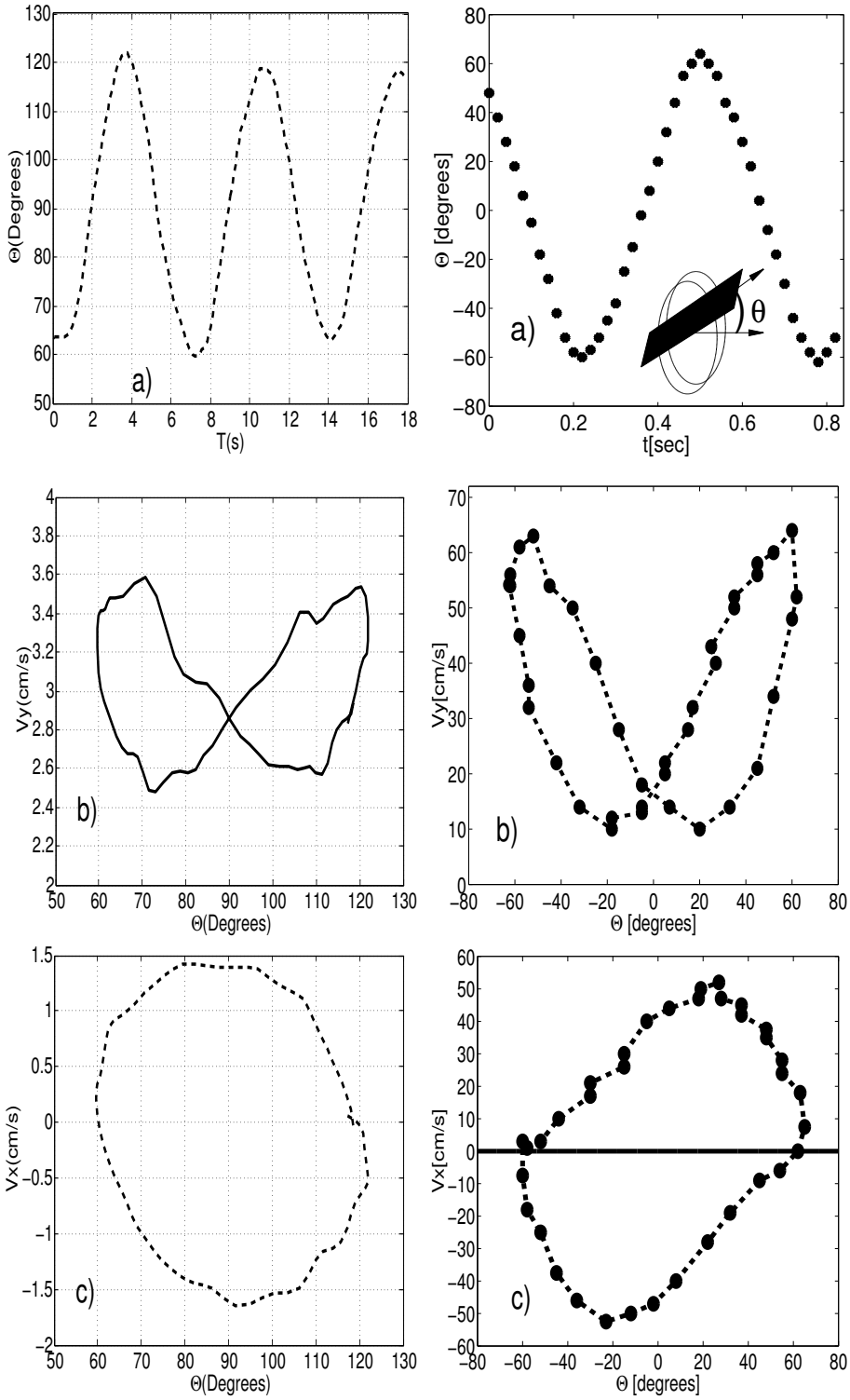

Figure 5.7: Comparison with the results of Belmonte et al. ref[12] for a falling strip in the periodic regime, for the (a) Vertical orientation Θ vs time. (b) Vertical velocity v_y vs Θ. (c) Horizontal velocity v_x vs Θ. The initial conditions are $h_o = 96$, $\Delta r = 0.133$, $\nu_1 = 0.025$, $\theta_0 = 63.4^o$.

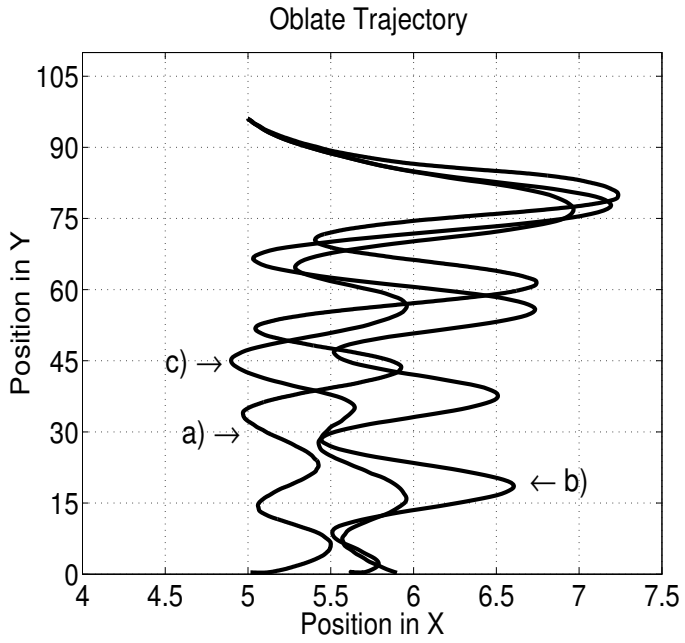

Figure 5.8: Initial conditions $h_o = 96$, $\Delta r = 0.25$, $\nu = 0.033$ and tiny variations of the initial orientation $(a)\theta_0 = 26.6^o$, $(b)\theta_o = 26.6001^o$, $(c)\theta_o = 26.6000001^o$.

of v_y.

The horizontal velocity oscillates around zero with constant period of oscillation and its maximum value $v_{x,max} = 1.5$ and the minimum $v_{x,min} = -1.5$ at $\Theta \sim 90^o$ as seen in fig. 5.7(c). When the horizontal velocity is zero the oblate takes its maximum (120^o) and minimum (60^o) values in Θ with a non-zero vertical velocity $v_y = 3.2$.

5.3 Chaotic regime.

5.3.1 Sensitivity to the change in the initial orientation

We now discusss the sensitivity of the dynamics to tiny changes in the initial orientation. We have simulated three trajectories shown in fig. 4.8, which have slightly different initial orientation. A tiny variation in the relative orientation ($\Delta\theta_o = 10^{-3}$) produces a significant variation in the shape of all the curves. These changes are appreciated in the lower part of the trajectories.

In order to get a better picture of sensitivity, we have incremented the fall height h_o to 166. The resulting four trajectories for four slightly different initial orientations in the vertical plane are plotted in fig. 4.9 and we observe high sensitivity to the initial orientation. For the four trajectories the relative angular variation is $\Delta\theta_o = 10^{-3}$.

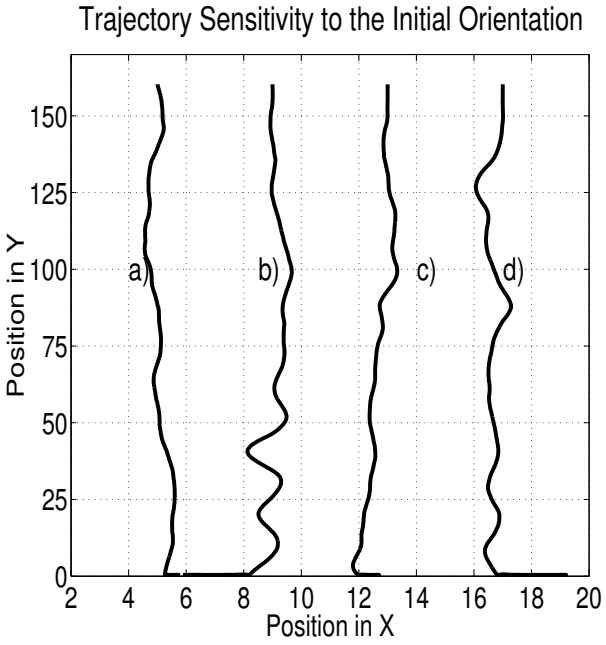

Figure 5.9: Initial conditions $h_o = 166$, $\Delta r = 0.25$, $\nu = 0.033$ and tiny variations of the initial orientation $(a)\theta_0 = 45.384^o$, $(b)\theta_o = 45.033^o$, $(c)\theta_o = 44.981^o$, $(d)\theta_o = 44.976^o$.

5.3.2 Power spectra, autocorrelation, Poincare section.

Due to the sensitivity to small changes in the initial orientation, we proceed to analyse the system by the Fourier power spectrum time series of the horizontal coordinate $x(t), x(t + \delta t), x(t + 2 * \delta t), ...$ and in our case $\delta t = 0.053566$. A broad spectrum of frecuencies appears as shown in fig. 5.10II thereby, indicating a chaotic motion.

The autocorrelation function, for the same time series (fig. 5.10I), does not fall quickly to zero rather decreases linearly with time and the points are not independent of each other.

In the figure 5.10III, we present slices or Poincaré sections (p_x, x), corresponding to the trajectories in fig. 4.9a which are quite irregular. The orbits are quasi-periodic in the sense that they pass repeatedly and irregularly through the whole domain. The orbits are not closed and are not associated with a particular time period. The sensitivity to initial conditions is clear in these four figures. A small change in the initial orientation results in large changes in position and velocity.

5.3.3 Lyapunov number.

We now investigate quantitatively, this sensitivity by studying the increment in the Euclidean distance, $d_{p_1p_2} = \sqrt{(x_1 - x_2)^2 + (y_1 - y_2)^2}$ between the curves presented in fig. 4.9 (a) and (c). Figure 4.11, shows that the distance between nearby points has an overall exponential time dependence $d(t) \sim \exp(\lambda t)$ and the fit gives an estimate for the

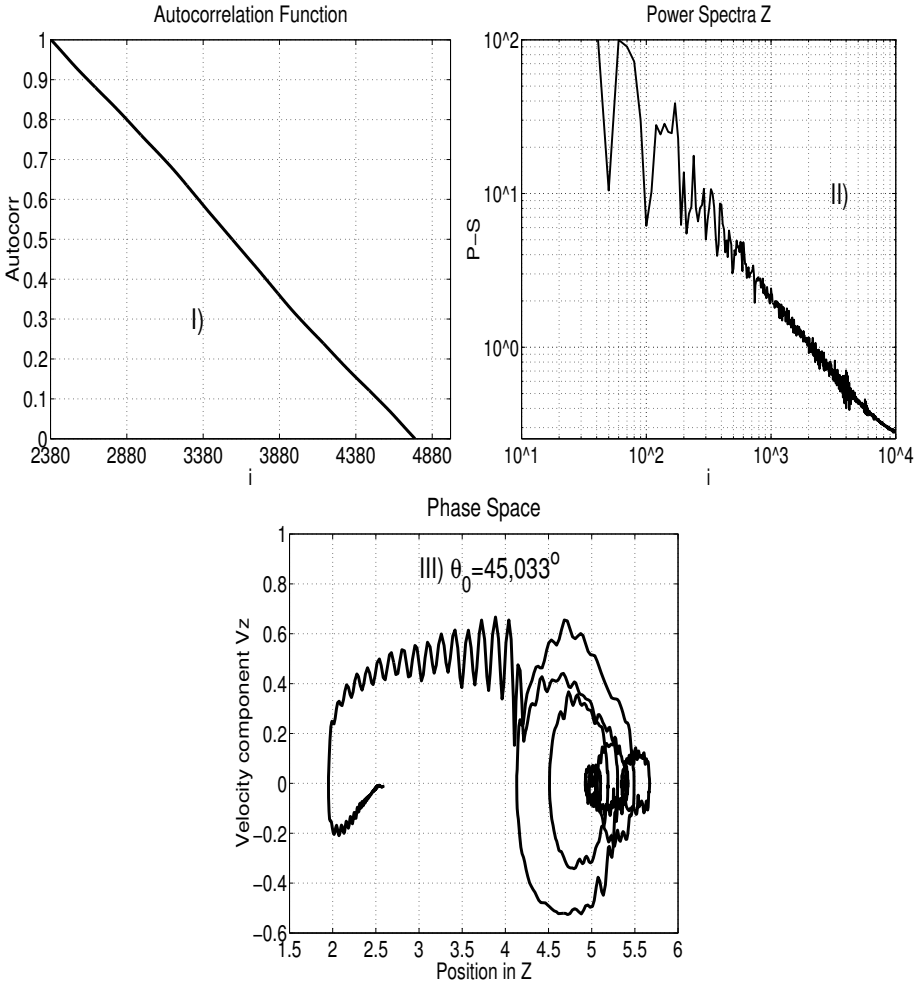

Figure 5.10: Detection of chaos. I) Autocorrelation function for the time series of $x(t)$ for the trajectory of fig. 14a. II) Power Spectra of fig. 14a III) Poincare section (p_x, x) for the trajectory of fig. 14a.

Lyapunov exponent $\lambda = 0.052 \pm 0.005$. The positive Lyapunov exponent gives a clear indication of Chaos.

5.4 Conclusions and Outlook

We have observed three phases of the dynamics of the system namely, steady-falling, oscillatory(periodic), and chaotic regimes. The steady-falling and the periodic regime exhibit a similar physical behavior as observed for flattened bodies by Field et. al. (1997), Belmonte et. al. (1998). We have characterized the dynamics of the steady-falling regime when the kinematic viscosity, dropping height, and oblate's aspect-ratio are changed. Some conclusions can be drawn from this part of the work.

(a) The spatial trajectories (x, y) are composed of oscillations that correspond to a damped

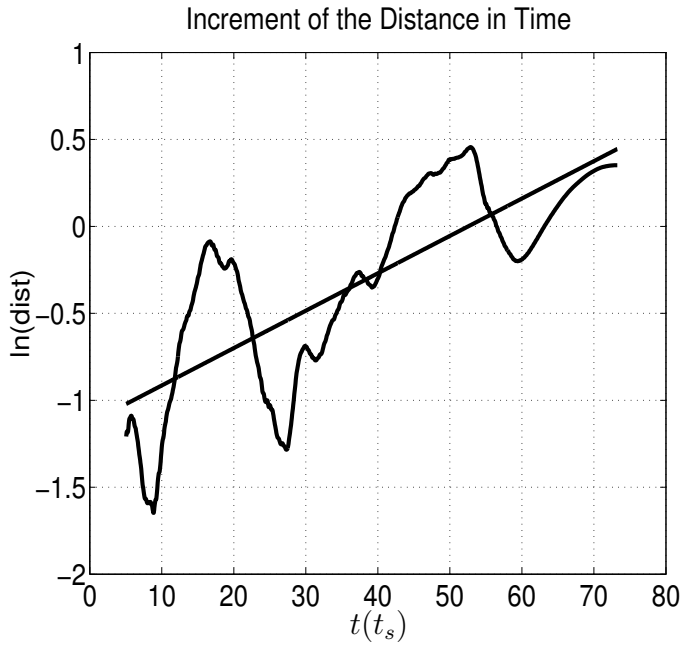

Figure 5.11: Increasing logarithmic behavior for the separation distance between the trajectories (a) and (c) in fig. 14, that slightly differ in the initial orientation angle by $\Delta\Theta = 0.403^o$.

harmonic motion. This regime is present for small values of $I^\star \approx 0.5 - 1$, $Re \approx 100$ and is shown in fig.5.1-5.4 There is no variation in the trajectories when we increase the initial height. The viscosity, for a constant small aspect-ratio, determines the decay of the position and the velocity of the ellipsoid as shown in fig. 5.2. When the aspect-ratio is changed, the trajectories vary significantly (fig.5.4).

(b) The final vertical velocity, v_y does not depend on the initial falling height and the kinematic viscosity.

(c) The vertical orientation, Θ of the ellipsoid, undergoes a rotational motion untill its major axis gets aligned with gravity. This tendency of exhibiting minimum resistance against the fluid exists for all Reynolds numbers in the range $Re \approx 1 - 500$.

The periodic behavior in our simulations is found for $Re \sim 400$ and small aspect ratios $(\Delta r \leq 0.1)$. The vertical orientation, Θ oscillates with twice the period of oscillation of the vertical velocity v_y and at the same period of the horizontal velocity v_x. This periodic motion has also been observed by (Belmonte et. al. 1998) and this shows that our simulations are essentially correct. In this regime the initial orientation determines the value of the amplitude of oscillation in the spatial trajectory (x, y), velocity v_y and orientation Θ, and plays the same role as the phase angle in the oscillatory motion. For $\Theta_o = 90^o$, the amplitudes of the above quantities approach a small value.

The chaotic behavior is present for larger aspect-ratios ($\Delta r \geq 0.3$) and in the entire range of Reynolds numbers used in the simulation. The separation between the spatial trajectories of the falling oblate ellipsoid diverges for small variations in the initial orientation

Θ_o, and grows exponentially in time. The value found for the Lyapunov exponent is $\lambda = 0.052 \pm 0.005$.

Chapter 6

Similarity law and phase transitions

In the two preceding chapters we have seen the characteristic phenomenology of each phase and the variation in each phase with respect to the physical parameters. In the first section of this chapter, we discuss the similarity law that describes intrinsically the dynamics of the steady-falling and oscillatory regime. A phase diagram has been compared to the results of Field et. al. (1997). Furthermore, we present a novel mechanism that explains the transition from the oscillatory to the steady-falling phase and then to the chaotic phase.

6.1 Steady-Falling Oblate Ellipsoid: Similarity law.

It is well known for large velocities that the inertial drag is given by,

$$F_d = C\rho_f V^2 S \tag{6.1}$$

where C is the form factor of the inertial drag, S is the cross-sectional area of the oblate ellipsoid, ρ_f the fluid density and V the ellipsoid velocity. The weight of the oblate ellipsoid is proportional to

$$F_i \approx \rho_{ell} R_M^2 R_m g \tag{6.2}$$

with ρ_{ell} being the ellipsoidal density, R_M and R_m being the minor and major radius, respectively. The terminal downward velocity is determined by the equilibrium between these two forces and since both densities are fixed, the terminal downward velocity is given by,

$$F_i = F_d \Longrightarrow V \sim \sqrt{gR_m} \tag{6.3}$$

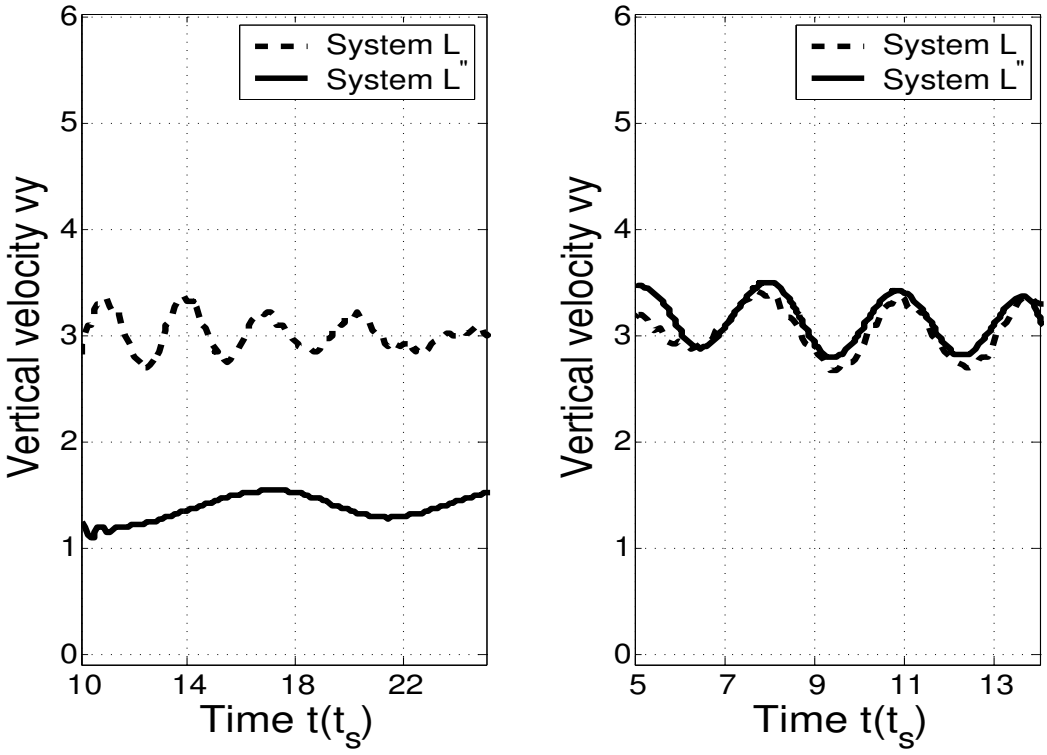

Figure 6.1: Initial conditions in the system. $\theta_o = 26.6^0$, $h_o = 86$, $\Delta r = 0.15$ and kinematic viscosity $\nu = 0.1$. In the figure (left) we plot the vertical velocity against time in both systems L (solid line) and $L^{'}$ (dotted line), and the superposition (right) performed applying the inverse transformation of table 1.

We suppose that the characteristic period of oscillation depends on the lateral dimension which in our simulations is $L_{hor}(= 25)$ and independent of the vertical dimension (falling height). Therefore, we assume that the period of oscillation should change as,

$$T^* \sim \frac{L_{hor}}{V} \tag{6.4}$$

The dynamics of the system, in general, depends on the Reynolds and the Froude numbers (Sec.2.1.2, Belmonte et. al. (1998)). We can rescale the parameters of a system of size L to a system of size $L^{'}$ through

System L	$\rightarrow$	System $L^{'}$
L_{hor}	$\rightarrow$	$n * L_{hor}$
R_M	$\rightarrow$	$n * R_M$
R_m	$\rightarrow$	$n * R_m$
g	$\rightarrow$	$\frac{g}{4*n}$

Table 1. Transformations rules.

The transformations presented in table 1 keep the Froude and Reynolds numbers constant and the dynamics in the two systems become equivalent if the velocity components change as in table 2. As a consequence of this transformation, the dynamics in system $L^{'}$ undergoes a change in the ellipsoid period, the vertical and horizontal components of the velocity, as shown in table 2.

System L	$\rightarrow$	System $L^{'}$
T^{*}	$\rightarrow$	$n * T^{*}$
V_{hor}	$\rightarrow$	$\frac{V_{hor}}{n}$
V_{vert}	$\rightarrow$	$\frac{V_{vert}}{n}$

Table 2. Period and velocity applying the transformation rules in Table 1.

In fig. 6.1 we present the superposition of the vertical velocity by applying an inverse transform in $L^{'}$ with n=2. The three curves coincide quite well in agreement with the scaling.

6.2 Periodic behavior: Similarity law.

Figure 6.2 shows the vertical velocity against time for the three systems L (solid line) and $L^{'}$ (n=2) and $L^{''}$ (n=4), respectively. We apply the transformation rules of table 1, ($n = 2$), and as in the case of the steady falling regime, the dynamics for the systems L and $L^{'}$, in the oscillatory regime, are related by a similarity law.

6.3 Phase Diagram.

In phase space, we define a dimensionless moment of inertia I^{*} which is the ratio of the moment of inertia of the oblate ellipsoid to that of its spherical equivalent at same Reynolds number. We do a similar analysis for our results as done by Field et. al. (1997). It is important to remark that the experiment was for a falling disk, with small aspect-ratio and we expect the dynamics of the system to be close to that of an oblate ellipsoid.

The definitions of the dimensionless variables for our system are:

$$I^{\star} = \frac{I_{oblate}}{I_{sphere}} = \frac{5}{4}\frac{r_m}{r_M}\frac{\rho_{ellip}}{\rho_{fluid}} = \frac{5}{4}\frac{\rho_{ellip}}{\rho_{fluid}}\Delta r \tag{6.5}$$

$$Re = \frac{U(2r_M)}{\nu} \tag{6.6}$$

Figure 6.3 left , shows the results in the log-log scale. At low values of I^{*} and small Reynolds numbers (high kinematic viscosity), the motion is over-damped and the oblate

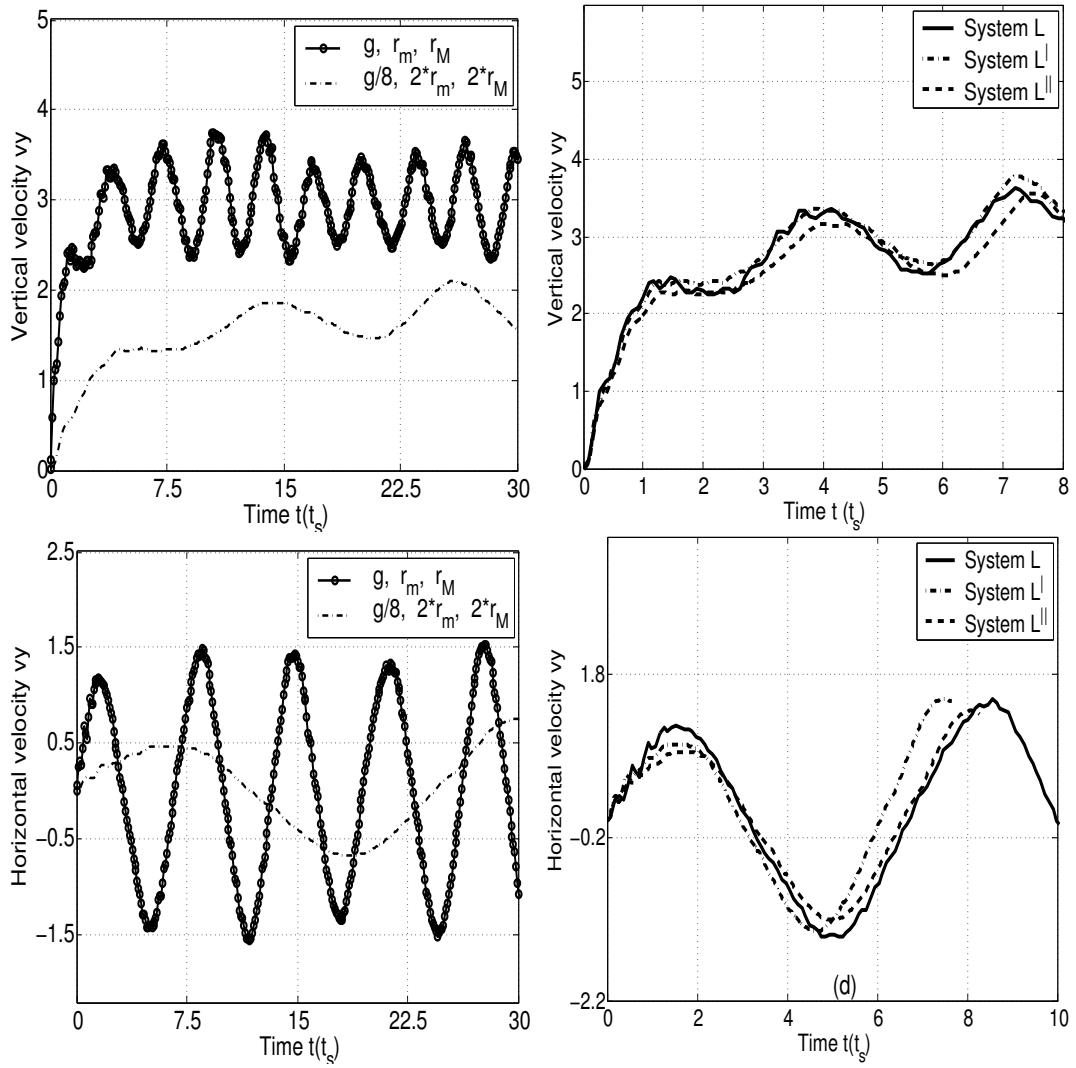

Figure 6.2: Initial conditions in the system. $\theta_o = 26.6^0$, $h_o = 86$, $\Delta r = 0.15$ and kinematic viscosity $\nu = 0.029$. In figure (left) we plot the vertical velocity against time for systems L (solid line) and $L^{'}$ (dotted line). The right figure shows the superposition applying the inverse transformation of table 1.

ellipsoid drops to the bottom of the container without any oscillation and this is the beginning of the steady falling regime. This is seen in the left hand bottom corner of the diagram. When the Reynolds number is increased $(Re \geq 10^2)$ and I^* is fixed, the trajectory is composed of successive oscillations that decrease in amplitude and eventually the oblate reaches the bottom of the container. This is the steady falling regime.

For small values of $I^\star \sim \Delta r < 1$, we have a flat ellipsoid. For Reynolds number, $Re \geq 400$, the trajectory, velocity and the orientation are characterized by oscillations that are periodic in time and space. This phase is called as the oscillatory regime. As we increase $I^\star$, the object becomes a sphere that is slightly flattened at the poles and its dynamics becomes sensitive to small variations in the initial orientation thereby exhibiting a chaotic trajectory.

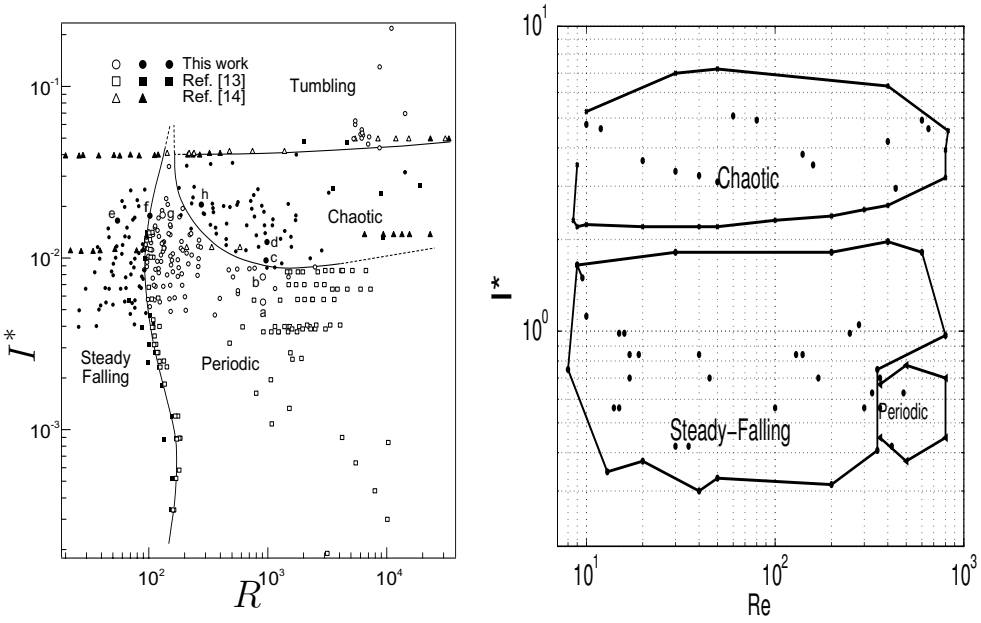

Figure 6.3: The left picture shows the phase diagram of falling disks reported in Field et. al. (1997). In the right plot we present the regimes of the phase space for the falling oblate ellipsoid obtained in our simulations. In both pictures, the vertical axis is the dimensionless moment of inertia I^*, and the horizontal axis Re is the Reynolds number.

If we compare our diagram with the experimental results obtained by Field et. al. (1997), fig. 6.3 left we see that in both pictures, the distribution of phases is equivalent. The differences in our diagram with that of Field's are that they use disks and not oblate ellipsoids and the tumbling regime is not present in our results. The coexistence of the dynamical phases as explained above is independent of the initial orientation of the oblate ellipsoid.

6.4 Transition from Steady-falling to Oscillatory phase

In fig. 6.4 we show the behavior of the characteristic time T^*/T (Sec. 4.1.2), adimensionalized using eq. 5.4, as we increase the Reynolds number Re, the characteristic time goes to zero at $Re_c \approx 355$, in fig. 6.3. Beyond this point we find the oscillatory regime, that behaves like a steady-falling regime with an infinite characteristic time.

Therefore, we can consider T^*/T as the order parameter and the control parameter is the Reynolds number for this transition. This transition is like a second order phase transition. The inset exhibits the power-law behavior with a critical exponent ≈ 0.5. In the case of the upper part of the transition, in fig. 6.3, the variation in the oblate ellipsoid aspect-ratio implies the change from steady-falling to oscillatory regime, which is also supported in fig. 5.4 where the trajectories vary from steady-falling to oscillatory as the aspect-ratio is decreased.

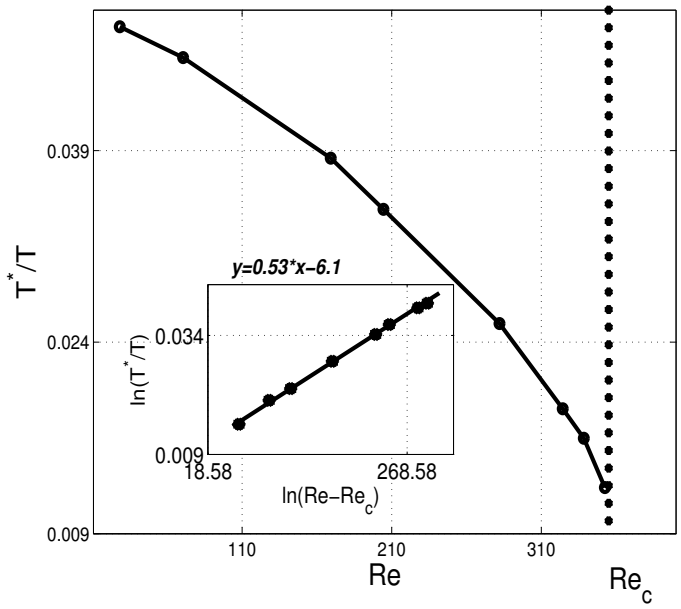

Figure 6.4: The order parameter T^*/T vs. the control parameter Re, with $Re_c \approx 355$. The inset shows the power-law behavior with an exponent close to 0.5

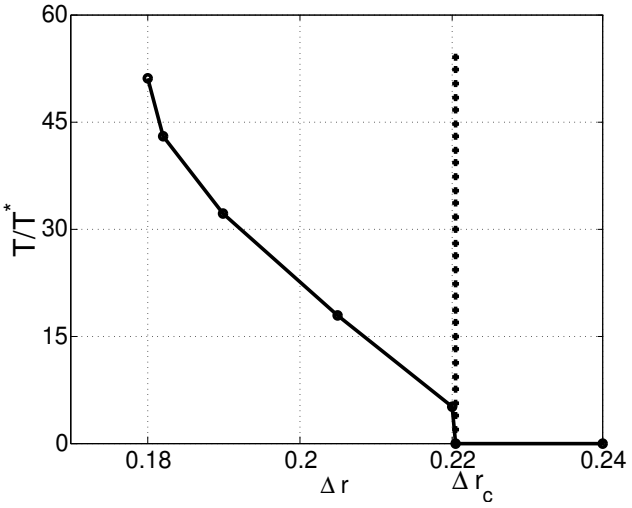

Figure 6.5: The order parameter T/T^* vs. the control parameter Δr, with $\Delta r_c \approx 0.22$.

6.5 Transition from Steady-falling to chaotic phase.

The transition from steady-falling to chaotic regime is presented in fig 6.5. We use the order parameter T/T^*, i.e., the inverse of the one used before in order to describe the transition, and the control parameter is the aspect-ratio Δr. At Δr_c a finite jump in the order parameter is observed. The characteristic time T/T^* disappears due to the non-regular oscillations that are very sensitive to small variations in the initial orientation. This transition seems to be therefore of first order.

6.6 Conclusions and Outlook

For the steady-falling and oscillatory regime we obtain a similarity law expressed in tables 1 and 2, which is a direct consequence of the invariance of the Reynolds and Froude numbers.

The construction of the phase diagram shows three well-defined dynamic regions as shown by Field et. al. (1997). The difference in the above reference is that the chaotic behavior is associated with the transition to chaos through intermittency which is not seen in our simulations. The phase diagram is independent of the initial orientation.

Our simulations show that the transition from steady-falling to oscillatory and the transition from steady-falling to chaotic regime can be understood as second and first order phase transition, respectively and the characteristic transient time being the order parameter.

Chapter 7

Many Particles

In the preceding chapters we presented the physics behind the falling of one oblate ellipsoid. Now, in this chapter we are going to expose the dynamics of many sedimenting ellipsoids in a fluid and under the action of gravity using the model given in chapter 2, at small and moderate Reynolds numbers. We study the settling or sedimenting velocity as function of the volume fraction. Also, we examine the vertical and horizontal fluctuations of the ellipsoids compared to spheres. Additionally, we consider the behavior of pair correlation functions as a function of the volume fraction. Next we present an orientational study using the Euler angles, and the angular distributions and the orientational behavior with volume fraction. The same study for the sedimenting velocity and orientation are made as the Reynolds number increases ($Re \approx 7$). Furthermore, we present the behavior of the orientational order parameter with the volume fraction. Finally, a conclusion is given.

7.1 Results

7.1.1 Sedimentation velocity for oblate ellipsoids

In fig. 7.1 we show the mean vertical sedimentation velocity $v(t)_{\|}$ as a function of the volume fraction Φ_V, within a range of 0.01 to 0.21, for oblate ellipsoids and spheres and then compare it to the phenomenological Richardson-Zaki law $\frac{v(\Phi)}{v_0} = (1 - \Phi_V)^n$ Richardson and Zaki (1954) with $n = 5.5$. The limit of $\Phi_V \rightarrow 0$ corresponds to the single falling ellipsoid which we studied in the previous chapter. It is interesting to point out that the sedimentation velocity of the ellipsoid, is small compared to that of the equivalent sphere, eq. 2.28, which follows the phenomenological Richardson-Zaki law. This is not the case for fibers (elongated ellipsoids), where it is found that the sedimentation velocity has a maximum for smaller volume fraction which can exceed the terminal velocity of a single fiber Kuusela et. al. (2003).

For oblate ellipsoids the mean vertical sedimentation velocity passes through a local maximum at $\Phi_V \approx 0.05$. This maximum is quite interesting since it is not observed for

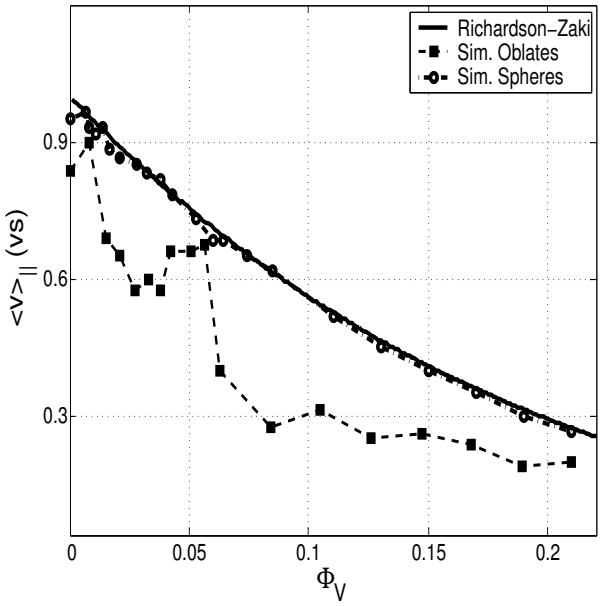

Figure 7.1: Mean sedimentation velocity $v(t)_{\|}$ for the oblate ellipsoid (dash-squared line) and sphere (dash-dot line), as function of the volume fraction Φ_V. The oblate ellipsoid aspect-ratio is $\Delta r = 0.25$, the radius of the equivalent sphere $R_{equi} = 0.97$ and the Reynolds number $Re = 4 * 10^{-2}$.

spheres. Similar non-monotonic sedimentation of non-spherical bodies (e. g. fibers) has been reported experimentally by Herzhaft and Guazzelli (1999) and for prolate ellipsoids in simulations by Kuusela et. al. (2001) due to an orientation parallel to gravity.

We choose the density of the fluid, the Stokes velocity and the larger radius of the ellipsoid equal to unity in our system. In all cases the container has a height, $L = 85$ and a base of 10×10, and the lattice constant, $h = 0.3$. We change Φ_V adding ellipsoids and the maximum number of ellipsoids in our simulations is of the order of several thousands. The ratio between the density of the oblate ellipsoids and the fluid is 4.

In fig. 7.2 we present the parallel ($\|$) and perpendicular ($\perp$) components of the velocity fluctuations with respect to gravity as a function of the volume fraction Φ_V which are defined as:

$$\delta v_{\|}^2 =< v_{\|}^2 > - < v_{\|} >^2 \tag{7.1}$$

$$\delta v_{\perp}^2 =< v_{\perp}^2 > \tag{7.2}$$

The angular brackets indicate averaging over the ellipsoids that have not reached the final bottom position at the container. The averages were made over at least 50 realizations starting with different random positions and orientations. In fig. 7.2 the vertical (parallel to gravity) fluctuations for spheres and for ellipsoids are much larger than the respective horizontal components. The fluctuations for ellipsoids decrease with the volume fraction. For an equivalent system of spheres, the fluctuations show a maximum at intermediate volume fractions ($\Phi_V \approx 0.07$) (Kalthoff et. al. (1996) and Nicolai et. al. (1995)). In all cases the fluctuations for the spheres are considerably larger than the fluctuations for oblate ellipsoids.

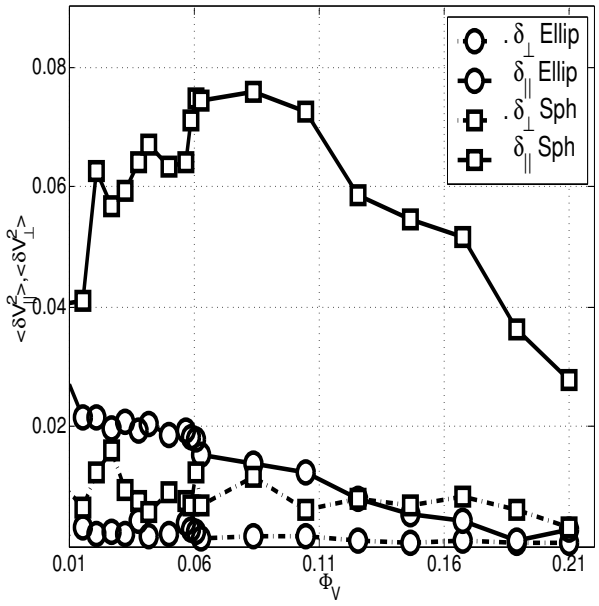

Figure 7.2: Velocity fluctuations for ellipsoids (circle-line) and spheres (squared-line) for the vertical (solid line), and horizontal (dash-dot line) components corresponding to fig. 1. The oblate ellipsoid has an aspect-ratio of $\Delta r = 0.25$, the equivalent radius of a sphere is $R_{equi} = 0.97$, and the Reynolds number $Re = 4 * 10^{-2}$.

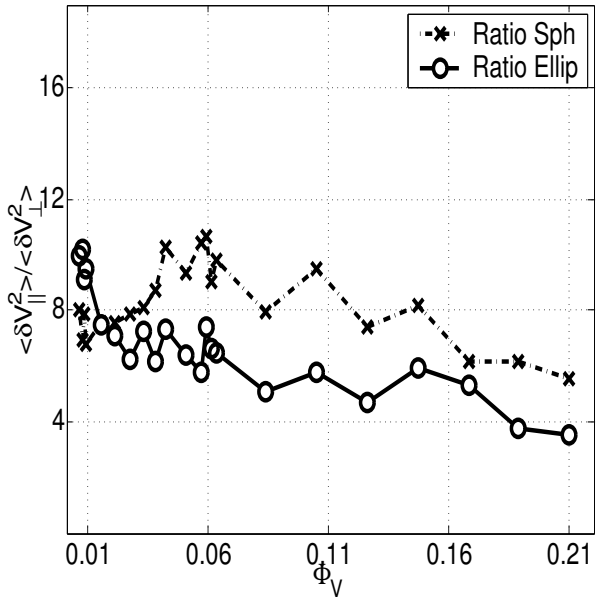

Figure 7.3: Ratio of the vertical to the horizontal velocity fluctuations for spheres and oblate ellipsoids as function of the volume fraction, Φ_V. The oblate ellipsoid aspect-ratio is $\Delta r = 0.25$, and the Reynolds number $Re = 4 * 10^{-2}$.

In fig. 7.3 we present the ratio, $\delta v_{\|}^2 / \delta v_{\perp}^2$ for spheres and oblate ellipsoids. For spheres the ratio shows a maximum around $\Phi_V \approx 0.07$ (Kalthoff et. al. (1996) and Nicolai et.

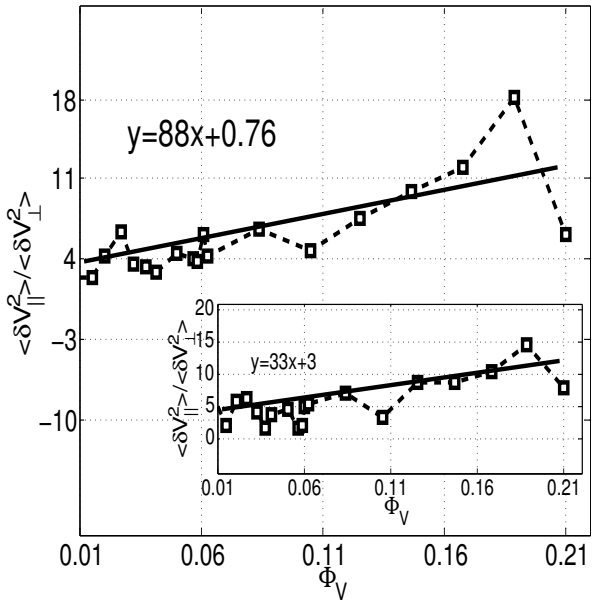

Figure 7.4: Ratio of the vertical velocity fluctuations for spheres to that of the oblate ellipsoids as function of the volume fraction, Φ_V. The inset shows the corresponding ratio for the horizontal fluctuations. The oblate ellipsoid aspect-ratio is $\Delta r = 0.25$, and the Reynolds number $Re = 4 * 10^{-2}$.

al. (1995)). For ellipsoids the ratio shows a slightly larger value than that of the spheres for very small volume fractions and has an overall monotonic decrease with the volume fraction.

We display the ratio of the vertical velocity fluctuations for spheres to that of the ellipsoids in fig. 7.4. The quotient exhibits a linear behavior with the volume fraction following approximately the relation $(\delta v^2_{vert,sph}/\delta v^2_{vert,ellip}) = 88 * \Phi_V + 0.76$. The inset shows the horizontal case, also a linear behavior $(\delta v^2_{hor,sph}/\delta v^2_{hor,ellip}) = 33 * \Phi_V + 3$ is found.

In figure 7.5 we present the parallel, $\tau_\parallel$ and perpendicular, $\tau_\perp$ components of the autocorrelation time for both ellipsoids and spheres. We use the definition of the correlation time as:

$$\tau_c = \frac{1}{C(0)} \int_0^\infty C(t)dt \tag{7.3}$$

Where $C(t)$ is the particle velocity autocorrelation function which is defined as $C(t) =< \delta v(t)\delta v(0) >$. Here $\delta v(t) = v(t) - < v >$ is the local velocity fluctuation, where $< v >$ was taken as the mean (horizontal or vertical) velocity.

The vertical component shows an overall large value for the oblate ellipsoids compared to that of the spheres. The horizontal components of the autocorrelation time between oblate ellipsoids and spheres are indistinguishable.

In figure 7.5 the four curves decay as power laws given by $\tau \approx \Phi^{-\alpha}$, We see that the values of α for the parallel and perpendicular components for ellipsoids are $\alpha_\parallel \approx 0.11$ and $\alpha_\perp \approx 0.16$ respectively and that for the spheres are $\alpha_\parallel \approx -0.10$ and $\alpha_\perp \approx 0.22$

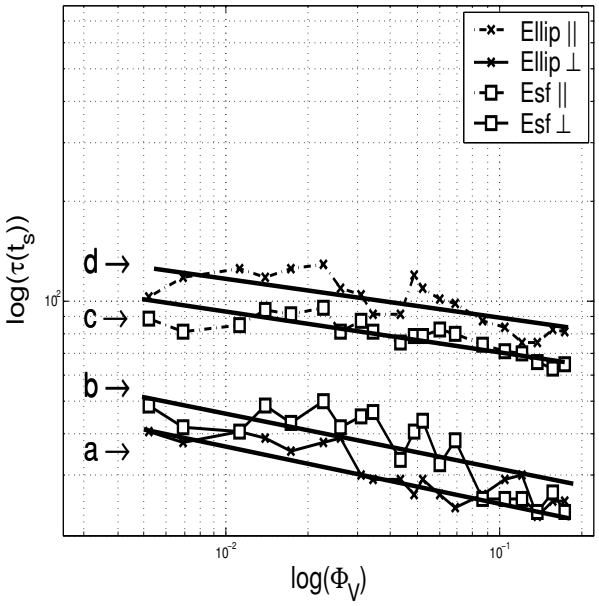

Figure 7.5: Autocorrelation times τ (in units of t_s) as function of the volume fraction Φ_V for oblate ellipsoids and the equivalent spheres split into components parallel ($||$) and perpendicular ($\perp$) to gravity. The oblate ellipsoid aspect-ratio is $\Delta r = 0.25$, the equivalent sphere system has a radius $R_{equi} = 0.97$ and the $Re = 4 * 10^{-2}$. The results are plotted in a log-log scale.

respectively. These exponents are valid in the dilute limit.

We calculate the pair correlation function for different volume fractions Φ_V and the results are shown in fig. 7.6. The pair correlation function, for smaller volume fractions $\Phi_V = 0.001$, clearly shows large inhomogeneities in the sense that there is a "packing formation" as seen in fig. 1.6, of oblate ellipsoids. These inhomogeneities disappear for large volume fraction $\Phi_V \geq 0,2$. Furthermore, in the intermediate case for $\Phi_V = 0.05$ we can see in the pair correlation function that the first peak is close to the origin, located at $r = 0.6$, which is also present at $\Phi_V = 0.2$ but smaller.

This additional larger peak at $\Phi_V = 0.05$ could be related to the local maximum in the sedimentation velocity fig. 7.1. By looking at the snapshots as the one shown in fig. 1.6 one sees that entire bundles of aligned particles seem to detach and move down faster which might well be the origin of this peak. This kind of "bundle behavior" has also been observed in the sedimentation of fibers, Herzhaft and Guazzelli (1999), where these bundles settle faster than the individual fibers.

7.1.2 Orientational behavior

For the measurement of the orientation we use the Euler angles described in fig. 4.4. The mean vertical orientation (MVO), θ , as a function of the volume fraction, is shown in fig. 7.7. For smaller volume fraction the MVO shows more alignment with gravity and in

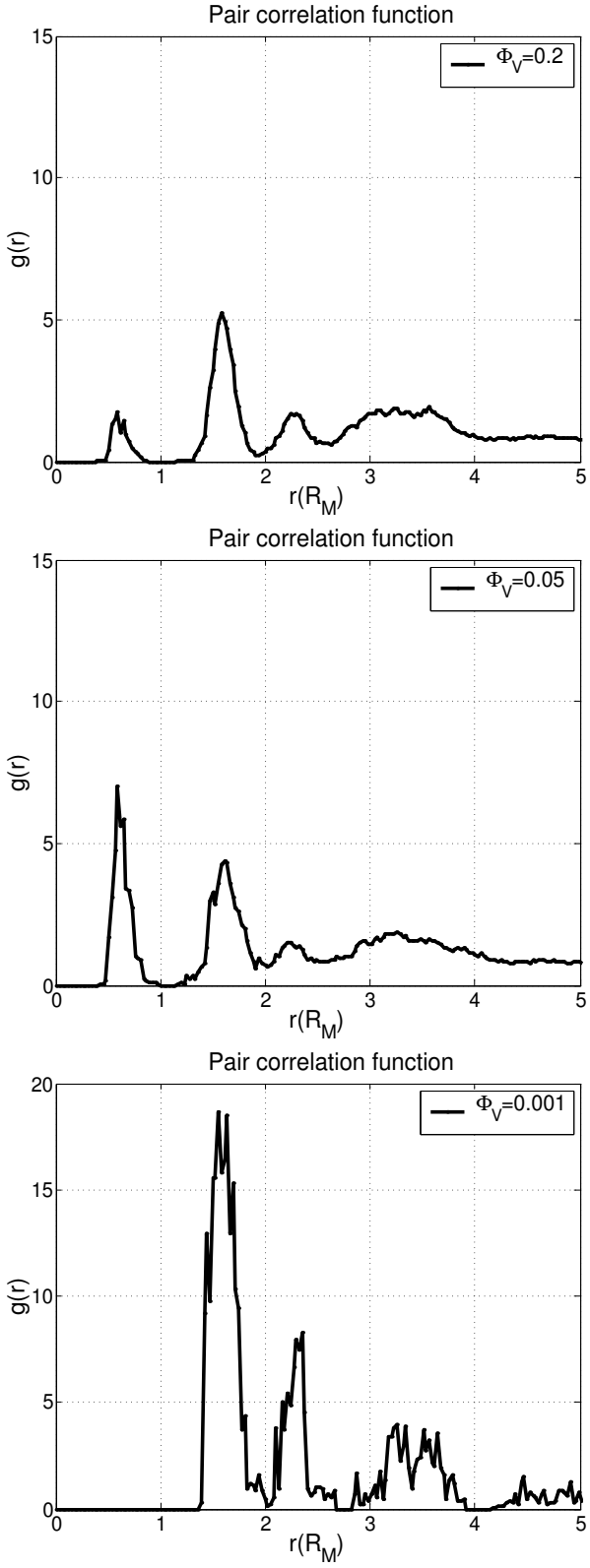

Figure 7.6: Pair distribution functions for oblate ellipsoids for different volume fractions, Φ_V. The Reynolds number $Re = 4 * 10^{-2}$.

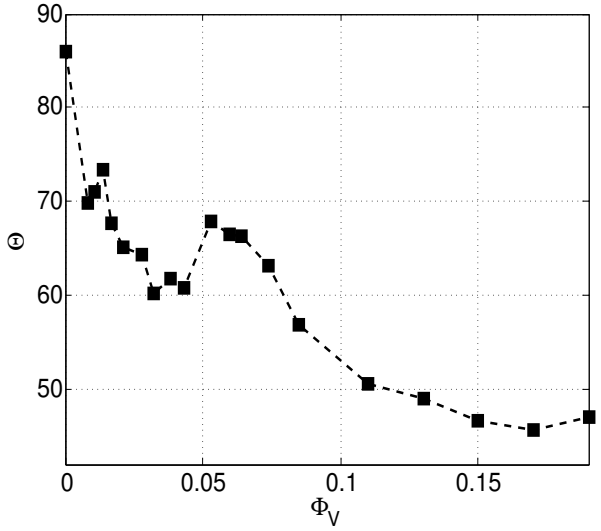

Figure 7.7: Mean vertical orientation θ for oblate ellipsoids as a function of the volume fraction Φ_V. The oblate ellipsoid aspect-ratio is $\Delta r = 0.25$, and the Reynolds number $Re = 4 * 10^{-2}$.

the limit $\Phi_V \rightarrow 0$ a closer alignment with gravity is observed which corresponds to the orientational behavior for one oblate ellipsoid observed in section $4.1.2; 4.1.3$.

We also see for the MVO an intermediate maximum, at $\Phi_V \approx 0.05$, which could explain the local vertical velocity maximum at the same volume fraction shown in fig. 7.1. This intermediate maximum is not present for spheres. For larger values of the volume fraction, $\Phi_V > 0.08$ the plot shows a monotonic decrease.

Figure 7.8 shows the orientational distribution function $P(cos(\theta))$ for the vertical angle, θ, for different volume fractions, Φ_V. For smaller volume fractions, $\Phi_V = 0.008$ the orientational distribution shows a maximum around $cos(\theta) \approx 0.1$ in agreement with fig. 7.7. The limiting case ($\Phi_V \rightarrow 0$), i.e., one sedimenting oblate ellipsoid, studied by us in section $4.1.2; 4.1.3$, presents a vertical alignment with gravity ($\theta \approx 90^o$), and in fig 7.7 we can see a value of $\theta \approx 85^o$.

As the volume fraction increases, the distributions flatten, and at $\Phi_V = 0.05$ the distribution shows a moderate maximum around $cos(\theta) \approx 0.45$, corresponding to the similar intermediate maximum in figures 7.7 and 7.1. We conclude that the vertical velocity is influenced significatively by the orientational behavior along gravity, as it is well known for other spheroid systems Kuusela et. al. (2003).

Figure 7.9 shows the orientational distribution function $P(cos(\phi))$ for the angle ϕ, for different volume fractions, Φ_V. The orientation around the vertical slightly increases for smaller volume fractions, and decreases with larger volume fractions. Similar behavior is also found for the third Euler angle ψ. We conclude that the Euler angles ϕ and ψ are not much influenced by the volume fraction.

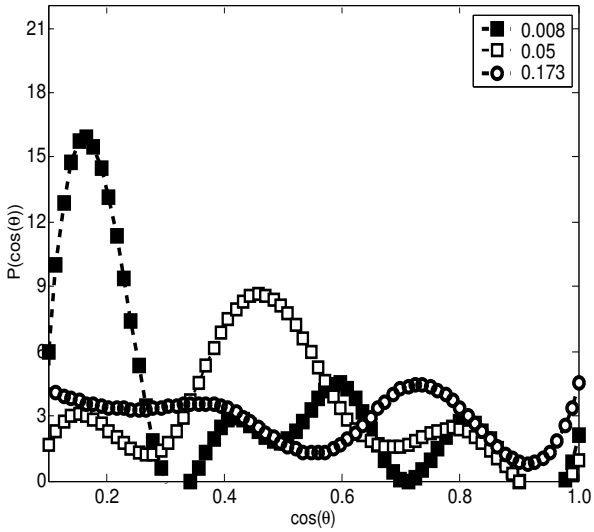

Figure 7.8: The distribution function $P(cos(\theta))$ for the mean vertical orientation θ for different volume fractions. The ellipsoid aspect-ratio is $\Delta r = 0.25$, and the Reynolds number $Re = 4 * 10^{-2}$.

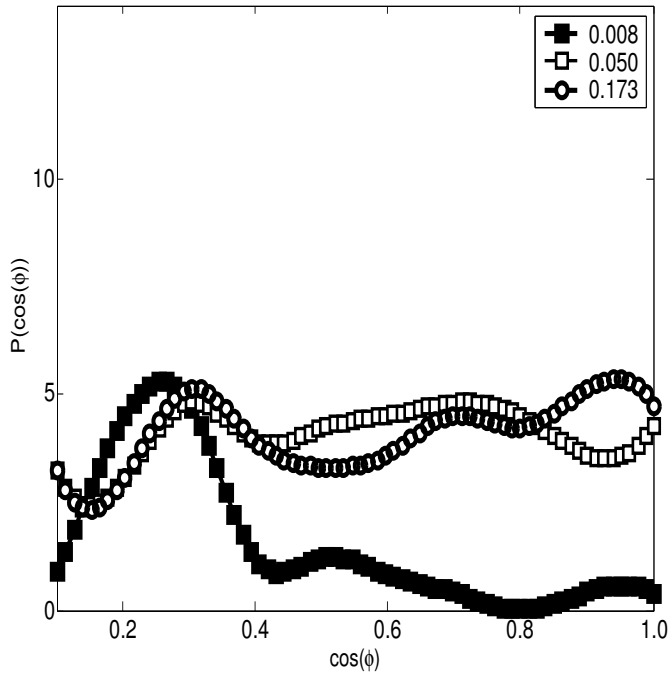

Figure 7.9: The distribution function $P(cos(\phi))$ for the mean vertical orientation ϕ for oblate ellipsoids. The aspect-ratio is $\Delta r = 0.25$, and the Reynolds number $Re = 4 * 10^{-2}$.

7.1.3 Orientational changes

To quantify the orientation of the oblate ellipsoids we introduce the quantity $\Psi = < 2cos(\theta) - 1 >$ that was also used in Kuusela et. al. (2003), Herzhaft and Guazzelli (1999)

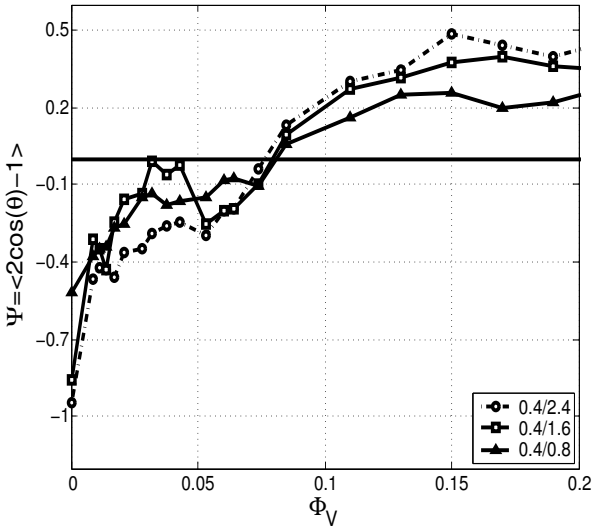

Figure 7.10: Order parameter Ψ as a function of the volume fraction, Φ_V for three different aspect-ratios $\Delta r = 0.4/2.4; 0.4/1.6; 0.4/0.8$.

as orientational order parameter. It would give -1, 0 or $+1$ if all the oblate ellipsoids were perpendicular to gravity, randomly oriented or aligned with gravity respectively.

Figure 7.10 shows the behavior of Ψ against Φ_V, for smaller volume fractions, $\Phi_V \approx 0.001 - 0.08$ the order parameter takes negative values evidencing the alignment along gravity and in agreement with the limit, $\Phi_V \rightarrow 0$ (one oblate ellipsoid, section $4.1.2; 4.1.3$). Approximately at $\Phi_V \approx 0.08$ the order parameter is zero. For larger $\Phi_V \geq 0.08$ a positive order parameter implies the orientation is perpendicular to gravity.

In the range of $\Phi_V \approx 0.001 - 0.08$, Ψ has a local minimum close to $\Phi_V \approx 0.05$ where we found a local maximum in fig. 7.7 and fig. 7.1. The simulations were repeated with two other different aspects ratios $\Delta_r = 0.4/0.8; 0.4/2.4$ and we observed similar behavior. In the case of one oblate ellipsoid ($\Phi_V \rightarrow 0$) the order parameter Ψ has a value very close to -1 as the ellipsoid aspect-ratio is increased.

7.1.4 Moderate Reynolds number

Figure 7.11 presents the mean vertical sedimentation velocity for oblate ellipsoids (□ squared line) and the equivalent spheres (○ circle lined) as a function of the volume fraction at moderate Reynolds number ($Re \approx 7$). In our previous work this simulation method has been used with success up to $Re \approx 10$ Höfler and Schwarzer (2000) and Kuusela et. al. (2003). The intermediate maximum for the ellipsoids is not observed in fig. 7.11 as seen in fig. 7.1 at low Reynolds number.

A comparison with the phenomenological Richardson-Zaki law (continous line in fig 7.11) shows an exponent around $n_{Sph} = 3.2$ for spheres and $n_{Ellip} = 4.0$ for ellipsoids. In both both cases, the data follow the Richardson-Zaki law rather closely. These

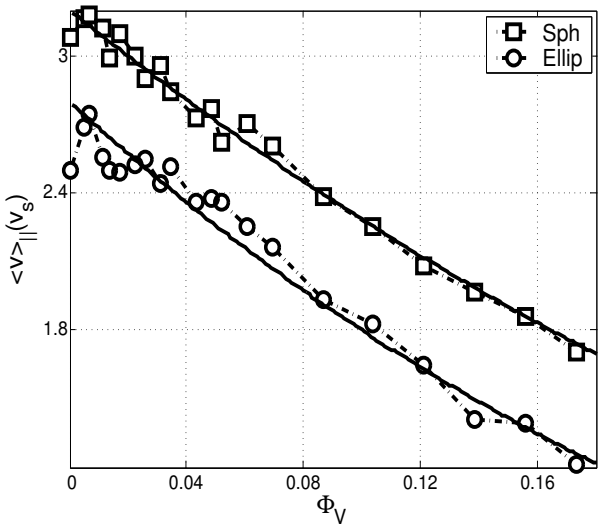

Figure 7.11: Mean sedimentation velocity $v(t)_{\|}$ for the oblate ellipsoid (dash-squared line) and a sphere (dash-circle line), as function of the volume fraction, Φ_V. The oblate ellipsoid aspect-ratio is $\Delta r = 0.4/1.5$, the equivalent sphere has $R_{equi} = 0.97$ and the Reynolds number $Re \approx 7$.

exponents ($n_{Sph} = 3.2$ and $n_{Ellip} = 4.0$) are between the low particle Reynolds number limit ($n \approx 4.5$) and a turbulent particle system ($n \approx 2.5$), Richardson and Zaki (1954).

Figure 7.12 (top) presents the vertical distribution function, $P(\cos(\theta))$ at moderate Reynolds number. For all volume fractions, $P(\cos(\theta))$ presents a larger distribution around $cos(\theta) \approx 0$ ($\theta \approx 90^o$), which tends to be much flatter ($cos(\theta) \geq 0.15$) than in fig. 7.8. For the other angular variables, ϕ and ψ, the distributions show a peak around $\cos(\phi) \approx 0$, $\cos(\psi) \approx 0$, and for larger volume fractions, they follow a constant behavior.

The bottom of fig. 7.12 shows the behavior of the orientational parameter Ψ at moderate Reynolds number. For one oblate ellipsoid ($\Phi_V \rightarrow 0$), the value of Ψ is closer to -1 (vertical alignment), as in the case of low Reynolds number fig. 7.9. The intermediate maximum, for $\Delta r = 0.4/1.5$, is not observed in figure 7.10, and the point at which the orientational parameter Ψ vanishes, is shifted slightly to the right ($\Phi_V \approx 0.1$) fig. 7.12 (bottom). This shift in Ψ is also seen in the case of fibers, when the Reynolds number increases, by a factor of 5, Kuusela et. al. (2003).

7.2 Outlook and Conclusions

We have simulated the sedimentation of oblate ellipsoids at small volume fraction ($\Phi_V \leq 0.2$) and small Reynolds number ($Re \approx 10^{-2}$). We have found that at intermediate volume fraction the settling velocity exhibits a local maximum which to our knowledge has never been reported in the literature. It would be desirable to experimentally verify this maximum.

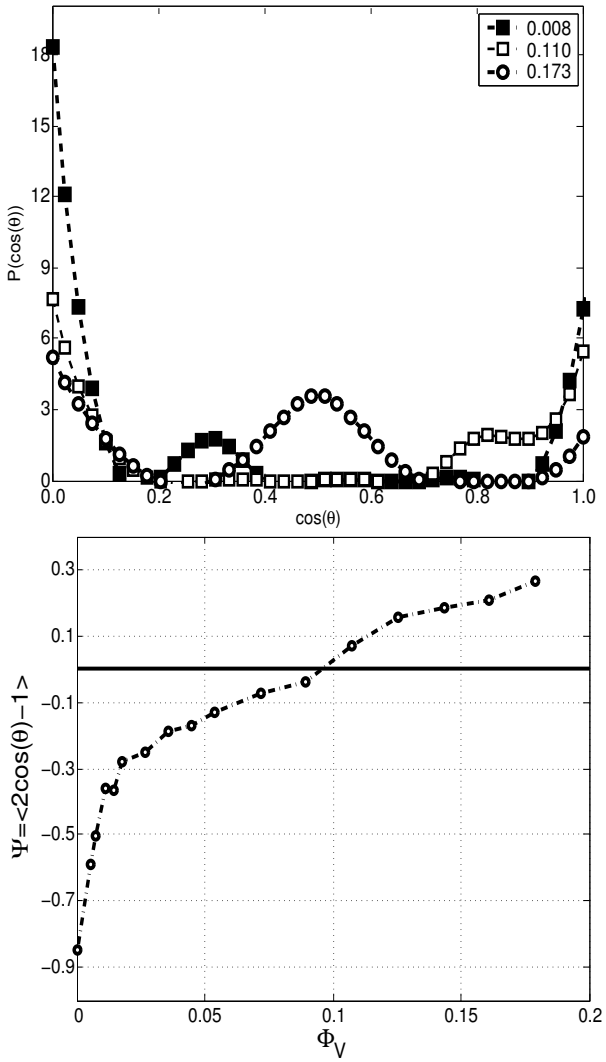

Figure 7.12: The top picture shows the distribution function, $P(cos(\theta))$ of the mean vertical orientation at different volume fraction Φ_V. The bottom picture shows how the order parameter behaves with the volume fraction Φ_V. The oblate ellipsoid aspect-ratio is $\Delta r = 0.4/1.5$, the equivalent sphere has $R_{equi} = 0.97$ and the Reynolds number $Re \approx 7$.

This local maximum in the velocity can be related to the non monotonic behavior of the vertical orientation of the oblate ellipsoids along gravity, which is shown in figures 7.7, and 7.8, and can be explained by the "cluster" formation shown in fig. 2.7, which is also found in fiber-like suspensions Herzhaft and Guazzelli (1999).

At low Reynolds number the orientational order parameter Ψ vanishes around $\Phi_V \approx 0.08$ fig. 7.7. As Φ_V decreases the orientational alignment with gravity increases as shown in fig. 7.7 and 7.12 (bottom), as for low and moderate Reynolds number and in the limit $\Phi_V \rightarrow 0$ a single ellipsoid aligns with gravity, which is a distinctive feature of the steady-state regime for a single oblate ellipsoid as reported in sections 4.1.2, 4.1.3 and Galdi et. al. (2001).

We also present data at moderate Reynolds number ($Re \approx 7$) for the sedimentation velocity of oblate ellipsoids as the volume fraction Φ_V is increased. As in the case of low Reynolds number the ellipsoids have a smaller sedimentation velocity than the equivalent spheres, fig. 7.1 and 7.11. The data for ellipsoids and spheres follow the Richardson-Zaki law Richardson and Zaki (1954) with exponents ($n_{Ellip} \approx 3.2$,$Re = 10^{-2}$) and ($n_{Sph} \approx 4.0$,$Re = 7$) respectively. The $P(\cos(\theta))$ distribution presents a larger alignment of ellipsoids with gravity compared to those with small Reynolds number. The vanishing of the order parameter is slightly shifted ($\Phi_V \approx 0.1$) to the right as the Reynolds number increases (see fig 7.12, bottom). The alignment with gravity is present for small and moderate Reynolds number as $\Phi_V \rightarrow 0$, as shown in fig. 7.12 (top) and fig. 7.8, which is in agreement with the orientational behavior of a single ellipsoid (section 4.1.2; 4.1.3). All the simulations in this work are located in the steady-falling regime, chapters 3 and 4, for a single oblate ellipsoid.

Chapter 8

Diffusion

This chapter is dedicated to the investigation of the diffusive behavior of sedimenting ellipsoids at low and moderate Reynolds numbers. We will begin with an introduction the common theoretical tools used to study the diffusive behavior of sedimenting particles. We discuss the results for ellipsoids in comparison to the equivalent spheres. Also, we explore the behavior of the system under variations of the dynamical viscosity, ellipsoid density and aspect-ratio. Furthermore, we give the orientational diffusion behavior. Additionally, we present the anomalous diffusion for oblate ellipsoids. Lastly, we summarize.

8.1 Introduction

As was explained in chapter 1, in a sedimenting suspension there are large changes in the concentration, that can either be temporal or spatial. This hydrodynamic-like diffusion dominates over the thermal Brownian diffusion, in the system considered here. The dimensionless quantity that accounts for the relative importance of this hydrodynamic difussion process over the thermal diffusion is the Péclet number Pe. When Pe is much larger than 1, Brownian motion can be neglected Ramaswamy (2001), Kuusela and Ala-Nissila (2001). For smaller values of $Pe << 1$, in turn, the hydrodynamic diffusion is not relevant.

In a regime where ($Pe >> 1$ and $Re << 1$), sedimenting spheres undergo long-ranged hydrodynamic fluctuations (see chapter 1, sec. 1.6). They cause in the long time limit, that the fluctuating particle motion becomes diffusive, Nicolai et. al. (1995). Therefore, we can determine the long time behavior of this random-like particle motions, by examining how the particle velocity becomes uncorrelated. This examination is realized by computing the particle velocity fluctuation autocorrelation function $C(t)$,(see Kuusela and Ala-Nissila (2001) and chapter 6, sec. 6.1). This quantity was defined in sec. 6.1, as follows:

$$C(t) =< \Delta v(t) \Delta v(0) > \tag{8.1}$$

where the average is taken over all the particles in motion. Here $\delta v(t) = v(t) - < v >$ is the local velocity fluctuation, whereas $C(t)$ is used to define the hydrodynamic diffusion coefficient D, in analogy with the Brownian tracer diffusion coefficient of Brownian particles immersed in a fluid (Kuusela and Ala-Nissila (2001)). D is defined by the Green-Kubo formula as:

$$D = \frac{1}{d}\int_0^\infty C(t)dt \tag{8.2}$$

where d is the spatial dimension, and for the discrete case as follows:

$$D = \frac{1}{d}[\frac{1}{2}C(0) + \sum_{n=1}^{\infty} C(n-\tau)] \tag{8.3}$$

where τ is the time step.

Another method to investigate the long time behavior of a sedimenting particles, is to compute the mean square particle displacement (hereafter M.S.D.), Kalthoff et. al. (1996), i.e. the second moment of the particle displacement, Herzhaft and Guazzelli (1999). It is calculated as follows:

$$< x^2(t) > := < [x(t) - (x(0) + < v > t)]^2 > \tag{8.4}$$

here the brackets indicate an average over the ensemble of those particles that are above the final bottom position in the container, and $< v >$ is their mean velocity taken of all particles with $v \neq 0$. A simple diffusive behavior is characterized by a linear growth with time. The self-diffusivity D, (Nicolai et. al. (1995)), can be determined from the slope of this line.

A large anosotropy between the M.S.D. for the parallel ($\|$) and perpendicular ($\perp$) components to gravity, has been reported by other authors (Nicolai et. al. (1995); Ladd (1996); Kalthoff et. al. (1996)), who found $D_\| >> D_\perp$. However, this anisotropy becomes less important for large Reynolds numbers and volume fractions (Kalthoff et. al. (1996), Nicolai et. al. (1995), Kuusela and Ala-Nissila (2001)).

Both, $D_\|$ and $D_\perp$ are obtained by examining long time behavior of the particle displacement by the following relations:

$$< x(t)_\perp >^2 \equiv 2D_\perp t \;\; ; \quad < x(t)_\| >^2 \equiv 2D_\| t \;\; . \tag{8.5}$$

Despite the clear evidence for normal diffusive behavior found in the current research, some experiments, (Rouyer et. al. (1999)) and simulations (Miguel and Pastor-Satorras (2001)), had shown that the velocities and trajectories of non-Brownian particles in a quasi bidimensional fluidized bed, exhibit a diffusive behavior along the perpendicular component and a superdiffusive behavior parallel to gravity. This latter superdiffusive

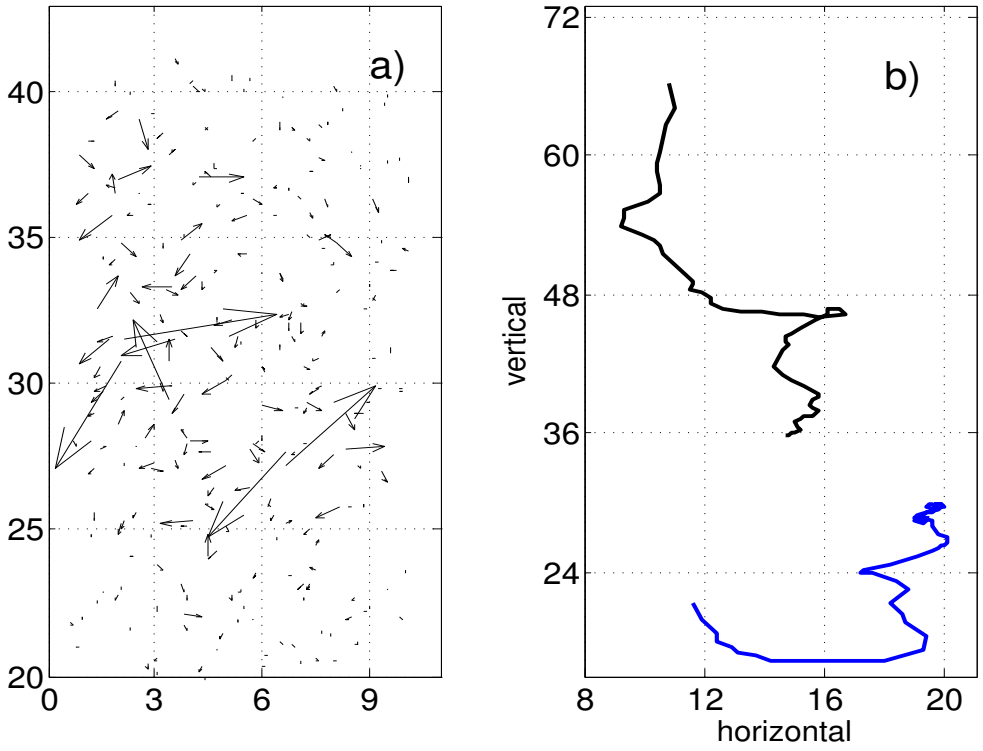

Figure 8.1: (a) A bidimensional velocity map showing faster and slower ellipsoids. (b) Typical Brownian-like trajectories in ellipsoids sedimentation in the laboratory reference frame. The Reynolds number is 2×10^{-2} and the ellipsoid aspect-ratio is $\Delta r = 0.4/1.6$.

behavior is also known as, "anomalous diffusion", and defined as the growth of the second order momentum by:

$$< x^2(t) > \equiv t^{\alpha} \tag{8.6}$$

with $\alpha \neq 1$.

Furthermore, we could extend equation 8.5 to the angular case, and define the M.S.D. as:

$$< \theta^2(t) > \equiv 2D_{\theta}t \tag{8.7}$$

With regard to sedimenting particles with non-spherical shape, apart, from a few exceptions (e.g. Kuusela et. al. (2001) and chapters $4, 5$), very little is known about the diffusive behavior, be it from simulation, experiment or theory. Non-spherical particles, with rotational symmetry around an axis (oblate or prolate ellipsoids), gives rise to rotational degrees of freedom, and generally plays an important role in the sedimentation, (Kuusela et. al. (2003) and chapter 6).

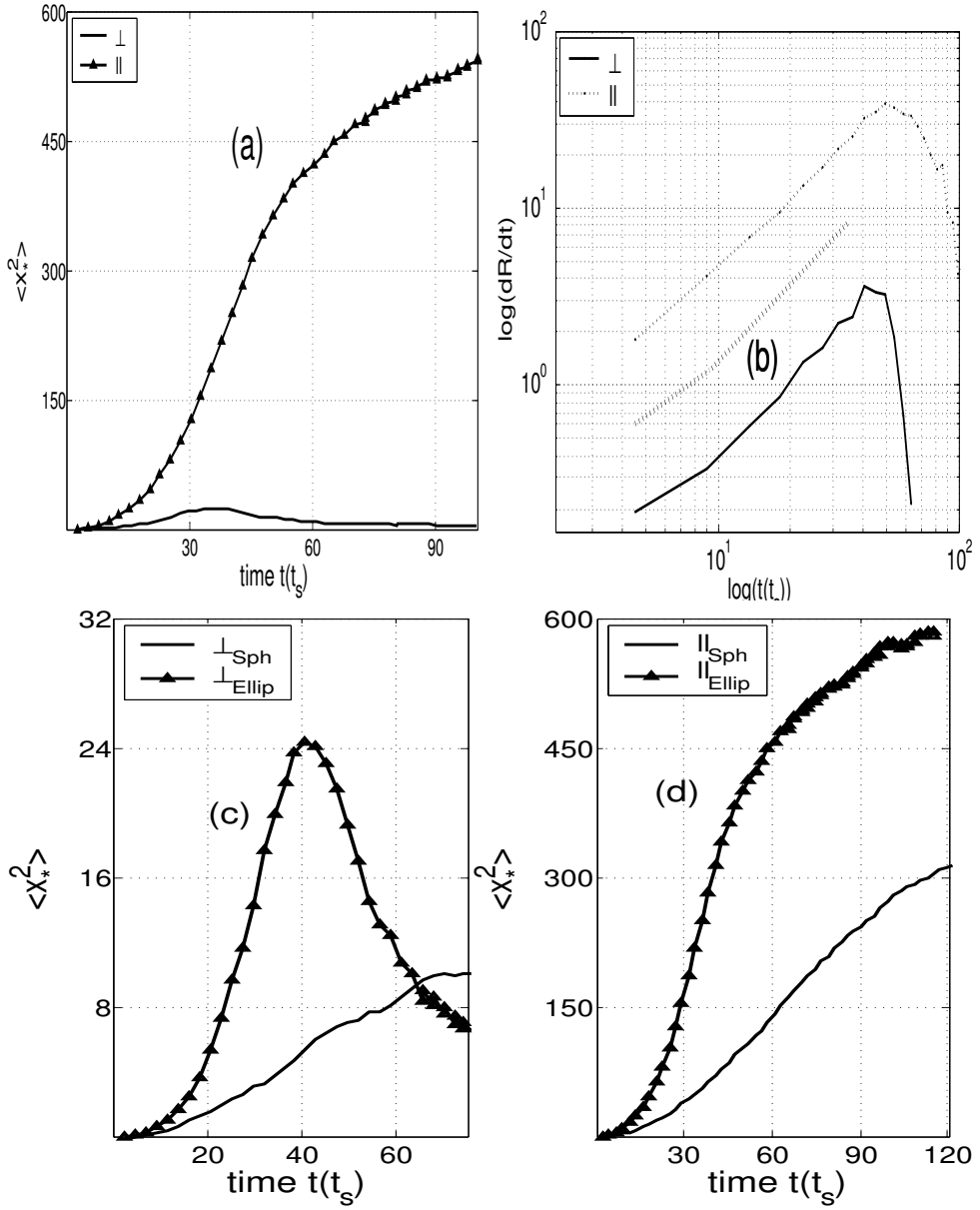

Figure 8.2: Figure (a) shows the parallel ($\|$) and perpendicular ($\perp$) components of M.S.D. for sedimenting ellipsoids. Picture (b) shows the slope behavior in time, of the curves in picture (a), in a log-log scale. The thick dotted lines in between, present the growth in the ballistic and non-diffusive regimes. The lower pictures, (c) and (d) show the comparison between ellipsoids and spheres with regard to the perpendicular $\perp$ (c) and parallel $\|$ (d) components of the M.S.D.. The sphere radius is $R_{equi} = 1.01$. The Reynolds number is 2×10^{-2} and the aspect-ratio $\Delta r = 0.4/1.6$. The number of ellipsoids is of the order of 10^3.

8.2 Results

In figure 8.1 (a), we present bidimensional snapshot of the velocity map for sedimenting ellipsoids. The map is characterized by complex and highly fluctuating velocity vectors

pointing in a wide range of directions, with very different magnitudes. The snapshot reflects the complexity of the swirls and channels that are very similar to those reported experimentally in Segré et al. (2001) and in simulations by Rouyer et. al. (1999). The volume fraction of the particles in the system is $\Phi_V = 0.2$.

In figure 8.1 (b) we present a typical ellipsoid trajectories in a container scaled in units of the mayor radii R_M. The trajectories are rather complicated and exhibit many of the characteristics observed by Nicolai et. al. (1995) and Peysson and Guazzelli (1999), such as the presence of loops and a strong anisotropy between the parallel and perpendicular fluctuations in the ellipsoid trajectory.

Pictures (a) and (b) in figure 8.2 show the M.S.D. for sedimenting ellipsoids. The graphics exhibit the large anisotropy between the parallel ($\|$) and perpendicular ($\perp$) components. In general, both components present an initial so called ballistic regime, as depicted in figure 8.2 (b), in a log-log scale, by a parallel thick dotted-line in between of the curves. This ballistic regime is proportional to $\approx t^2$. Then, we found a non-diffusive behavior which is quite interesting and will be discussed in section 5 of this chapter.

Another aspect of the long-time behavior is that, as a consequence of the finite size container, the ellipsoids reach a saturation regime. This is characterized by fluctuations around the final position of each ellipsoid in the container bottom (Kalthoff et. al. (1996)). The graphics are normalized in both components according to $\langle x_*^2 \rangle \equiv \langle x^2 / R_{equ}^2 \rangle$ and the time in units of t_s, (see eq. 2.30).

The comparison between the M.S.D. for ellipsoids and that for spheres is given in figure 8.2, in the $\perp$ (c) and $\|$ (d) components. In our simulations, we found at lower Reynolds number ($Re \approx 10^{-2}$) and for flat ellipsoids, that the components for ellipsoids are much larger than those for spheres. This phenomenon can be explained by the presence of a much larger net displacement for ellipsoids than spheres, as can be seen in figure 8.1.

It is interesting to point out, that the perpendicular component of the M.S.D., fig. 8.2 (c), for a very flat ellipsoid, experiences a peak which then decreases abruptly, before the saturation regime is reached. This behavior is completely new and can only be associated to the particle shape, since the spheres only echibit a monotonic increment, (see fig. 8.2 (c)). This large peak in the ellipsoid perpendicular component, is present in all simulations with a fixed aspect-ratio, but variable viscosity or particle density. .

8.2.1 Change in density, viscosity and aspect-ratio

The slope for each one of the curves in fig. 8.3 (a) and (b) becomes large as the ellipsoid density is increased, keeping constant the rest of parameters in the system, showing the increase of the inertia in ellipsoids and spheres. For ellipsoids, the slope in both components increases much faster than for spheres. For the parallel component to gravity, the denser ellipsoids diffuse much faster, quickly reaching the saturation regime. This can be seen by comparing the curves for $\rho_1 = 5.0$ and $\rho_4 = 11.0$ in figure 8.3 (a). In figure 8.3 (c) and (d) we present the M.S.D. behavior as the kinematical viscosity is changed. For all of the cases, the increament in the viscosity decreases the slope of each on the

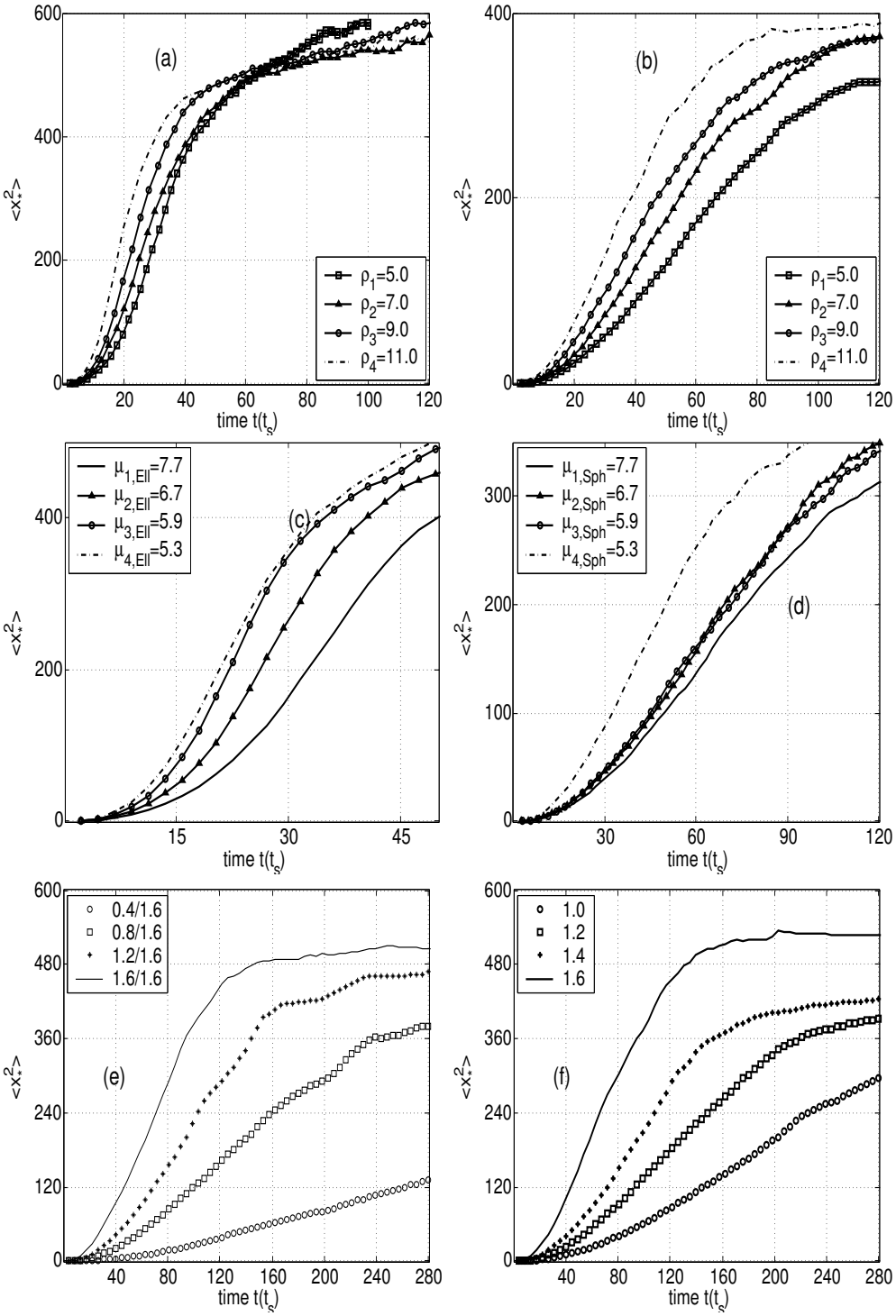

Figure 8.3: Figures a) show the parallel $\|$ component of the M.S.D. for ellipsoids and equivalent spheres b), as the particle density changes. Figures c) and d) present the variation for the dynamical viscosity and figures e) and f) show the change in the oblate aspect-ratio and the equivalent radius, respectively. The Reynolds number is $Re \approx 10^{-2}$, the spheres radius is $R_{equi} = 1.01$ and the ellipsoid aspect-ratio $\Delta r = 0.4/1.6$.

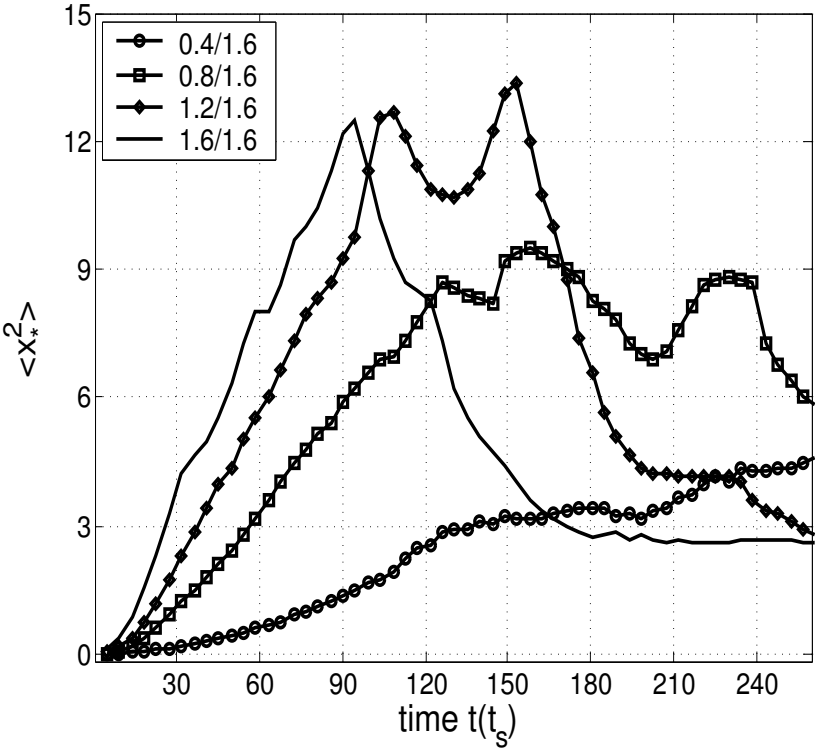

Figure 8.4: Behavior of the perpendicular component of M.S.D. for ellipsoids as the aspect-ratio changes ($\Delta r = 0.4/1.6$,$\Delta r = 0.8/1.6$ $\Delta r = 1.2/1.6$ and $\Delta r = 1.6/1.6$). The Reynolds number is $Re \approx 10^{-2}$.

curves In figure 8.3 (c) and (d). The increase of the viscosity reduces the M.S.D. in the suspension. Also, as for particle density variations, the changes in the viscosity lead, for lower Reynolds numbers, to a directly proportional increment in the M.S.D..

The peaks in the ellipsoid perpendicular component (see fig. 8.4), is present in all of the simulations where the kinematical viscosity or particle density are changed, with a fixed aspect-ratio and lower Reynolds number ($Re \approx 10^{-2}$).

Next, we present the M.S.D. for different ellipsoid aspect-ratios Δr and equivalent sphere radii R_{eq}. The variation in the aspect-ratio goes from a flat ellipsoid up to a sphere, while the volume fraction $\Phi \approx 0.2$ is kept constant. The response under variations of the oblate aspect-ratio, presents a linear increase in the slope of each curve, in both ellipsoids and spheres, as is shown in figures 7.3 (e) and (f), respectively.

The slope growing in the M.S.D. as the aspect-ratio increases, becoming one, shows that the spheres have a much larger M.S.D. than the ellipsoids. The ellipsoids, on the other hand, have more resistance to sediment. This characteristic is present in both components (see figure 8.3 (e) and 8.4). As for the parallel component fig. 8.3 (e) and (f), spheres and ellipsoids present the same monotonic behavior before they reach the saturation regime.

In figure 8.4, we can see how the perpendicular component of the M.S.D. approaches the saturation regime, as the aspect-ratio grows. The peak is shifted to the left and becomes

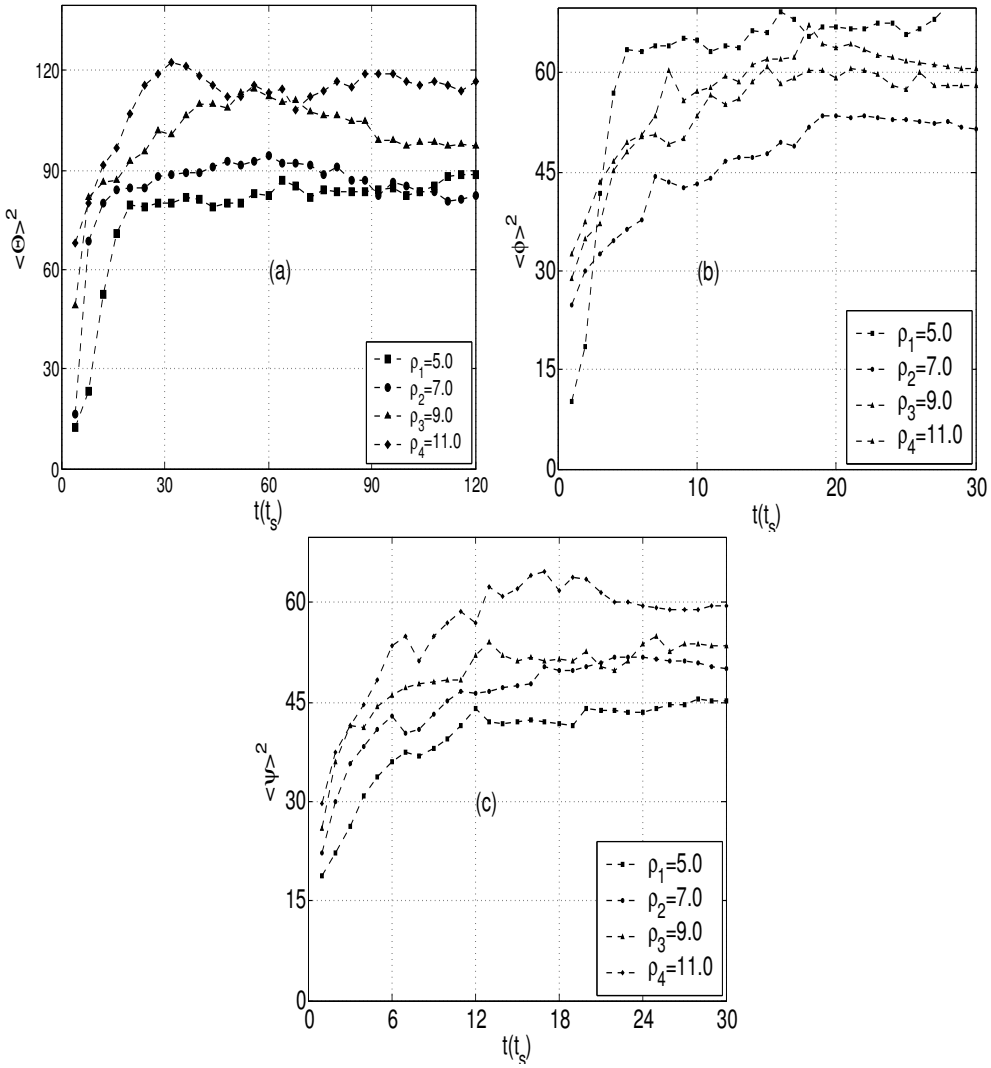

Figure 8.5: Angular M.S.D. for the Euler angles θ-fig. (a), ϕ-fig. (b) and ψ-fig. (c) under variations of ellipsoid density, $\rho_1 = 5, 7, 9, 11$. The Reynolds number is 2×10^{-2} and the ellipsoid aspect-ratio is $\Delta r = 0.4/1.6$.

much larger and sharper as the aspect-ratio becomes 1 (the sphere).

8.2.2 Orientational diffusion

Figure 8.5 shows the angular M.S.D., $< \Delta\Theta >^2$ for the three Euler angles (see figure 4.4 in chapter 3), under variations of the ellipsoid density, which correspond to the translational behavior shown in figure 8.3 (a).

It is interesting to note, that the angular M.S.D. follows a behavior which is similar to the corresponding translational degrees of freedom, in the sense that the angular M.S.D. exhibits at the beginning of the sedimentation a faster growth and then approaches to

the saturation regime. This approach to saturation is quite faster (see fig. 8.5), as it is compared to the translational components (see fig. 8.3 (a)), and is present for the three Euler angles.

As the oblate density is increased, the angular M.S.D. for each one of the Euler angles slightly increases. The relevant variation in the angular M.S.D. is present in the upward shifting in the final value of the saturation regime (see fig. 8.5). We can observe (approximately), that equal variations in ellipsoid density cause equal upward increments in the saturation value.

It is also interesting to observe, that the decrease of the kinematical viscosity gives rise to the same kind of upward shifting as described above, but with a smaller shifting value of the final saturation (see fig. 8.6).

Increasing the importance of inertial forces by using a higher mass of the ellipsoid or reducing the kinematical viscosity, increases the saturation state in the Euler angles.

8.2.3 Non-diffusive dynamical behavior

We now study the behavior of the time derivative of the M.S.D., defined as $dR(t)/dt$ with $R(t) =< x^2(t) >$, eq. (8.4). This type of characterization of the diffusive behavior in sedimentation is also used in the work of Rouyer et. al. (1999) and Miguel and Pastor-Satorras (2001). In a case where $dR/dt \equiv constant$, we have a simple diffusive behavior, whose constant value is equivalent to one half of the diffusion constant, (see eq. 8.5). If we find non-diffusive behavior, then $dR/dt \neq cte$ and the temporal behavior of the M.S.D. is given by eq. (8.6).

Change in the particle density

Figure 8.7 (a) presents the perpendicular component ($\perp$), if the sphere density is changed. For $\rho_1 = 5.0$ the evolution of the curve in time, exhibits the above regimes, ballistic, simple diffusive and saturation. An interesting aspect here consists in the fact that when the particle density ρ is increased ($\rho = 5.0 \rightarrow \rho = 11.0$) the simple diffusive regime is much shorter in time. Basically, the increment of the inertial forces, reduces the time of the simple diffusive regime. This general behavior for spheres is in agreement with the results presented by (Rouyer et. al. 1999) and (Miguel and Pastor-Satorras 2001).

For the parallel component ($\|$) figure 8.7 (b), all the curves exhibit a ballistic regime. After that, a non-diffusive behavior characterized by t^α, with an exponent $\alpha = 1.4$ can be observed (Rouyer et. al. (1999)). Like the perpendicular component, the length in time of the parallel component is reduced for large sphere densities, as shown in figure 8.7 (b).

In figure 8.8 (a) and (b) we can observe the behavior of the time derivative of the M.S.D. for ellipsoids. For the perpendicular and parallel components (see figure 8.8) we first find a ballistic regime and then a non-diffusive regime, which up to now is not known in the

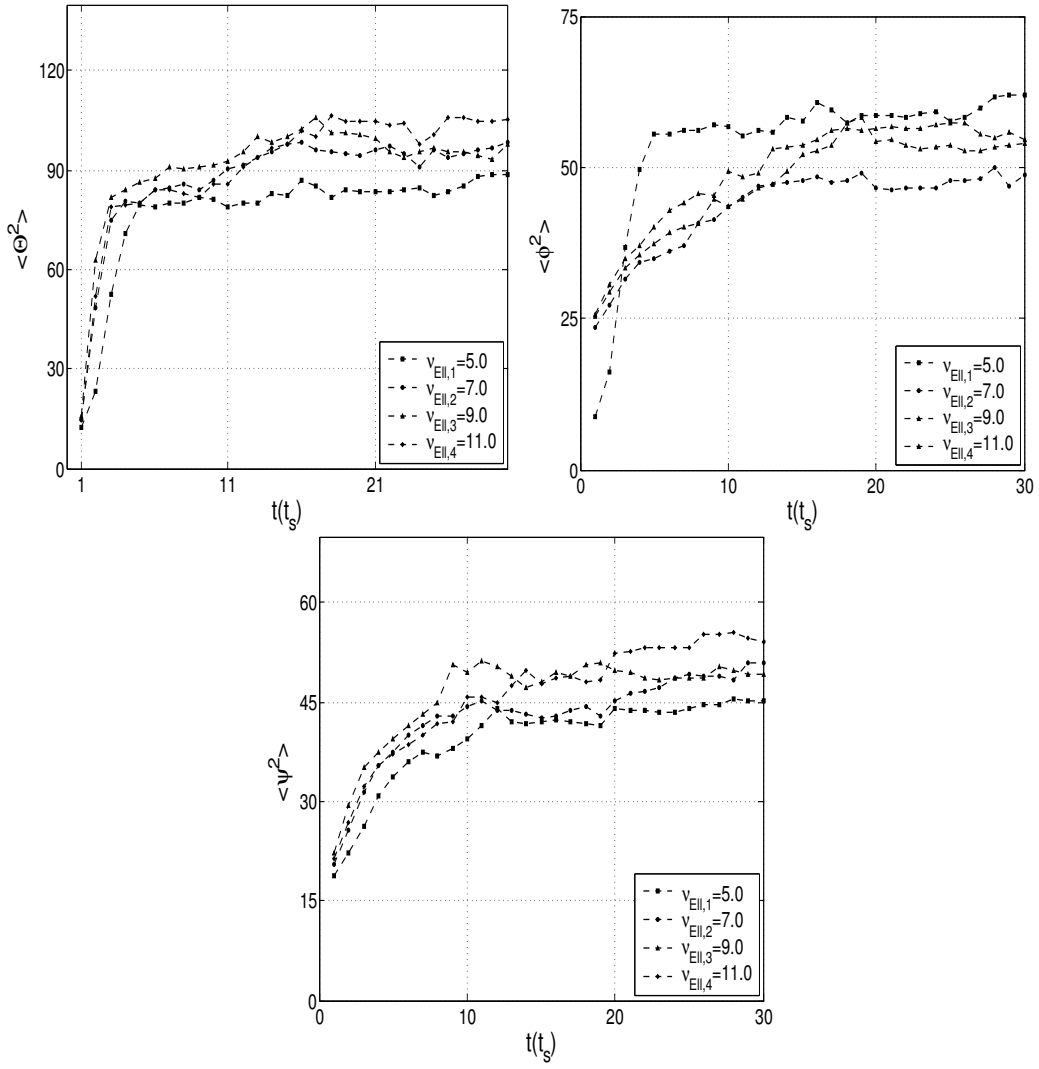

Figure 8.6: Angular M.S.D. for the Euler angles under variations in the kinematical viscosity. The Reynolds number is 2×10^{-2} and the ellipsoid aspect-ratio is $\Delta r = 0.4/1.6$.

literature. The exponents in both components are equal $\alpha_{parallel} = 2.5, \alpha_{perp} = 2.5$ and larger than the slope of the ballistic regime.

In contrast to the spheres, the density variation does not modify significatively the non-diffusive regime's characteristic time. This kind of behavior for the diffusion of nonspherical particles was never before reported up to now, and the experimental verification will be necessary. From the plot, we can also extract that $D_{vert} \gg D_{hor}$, therefore the diffusive regime is highly anisotropic.

For both ellipsoids and spheres, the M.S.D. in both components are displaced upward as the particle density grows. As expected at low Reynolds number, an increment in the inertial forces, produces a large growth of the M.S.D..

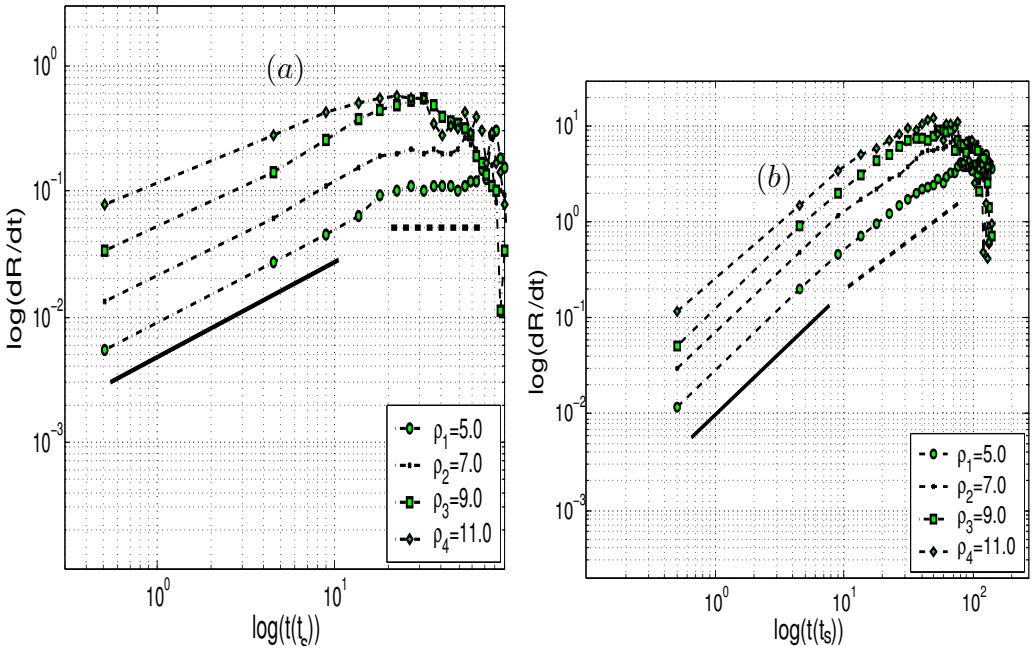

Figure 8.7: The figures show the perpendicular $\perp$ (a) and parallel $\parallel$ (b) components of the time derivative of the M.S.D. for spheres as the density is changed. The Reynolds number is 2×10^{-2}, the spheres radius $R_{equi} = 1.01$. The solid and dashed lines represent the diffusive and non-diffusive behavior, respectively.

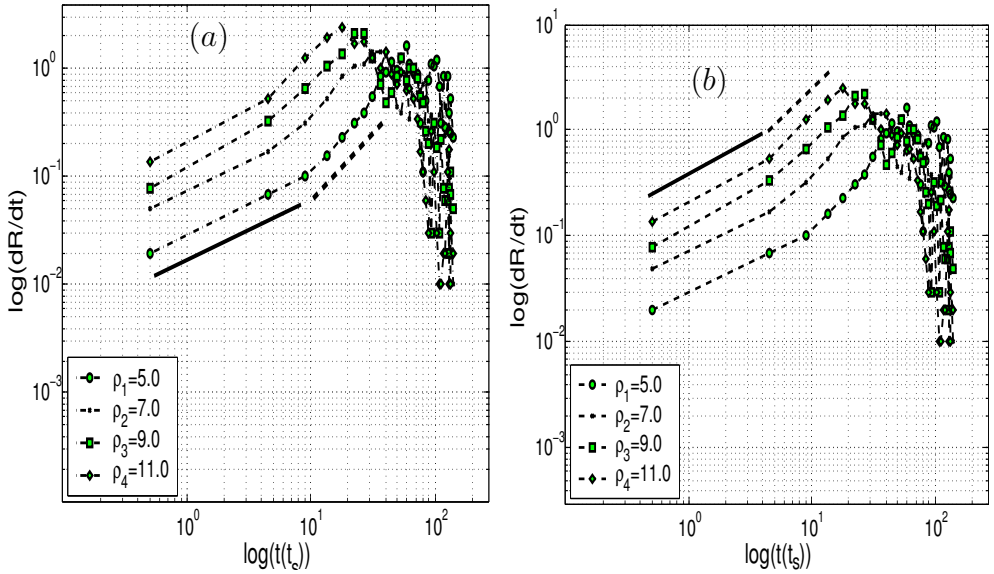

Figure 8.8: The figures show the perpendicular $\perp$ (a) and parallel $\parallel$ (c) components of the time derivative of the M.S.D. for ellipsoids as the density is changed. The Reynolds number is 2×10^{-2}, the ellipsoid aspect-ratio is $\Delta r = 0.4/1.6$. The solid and dashed lines represent, the diffusive and the non-diffusive behavior, respectively.

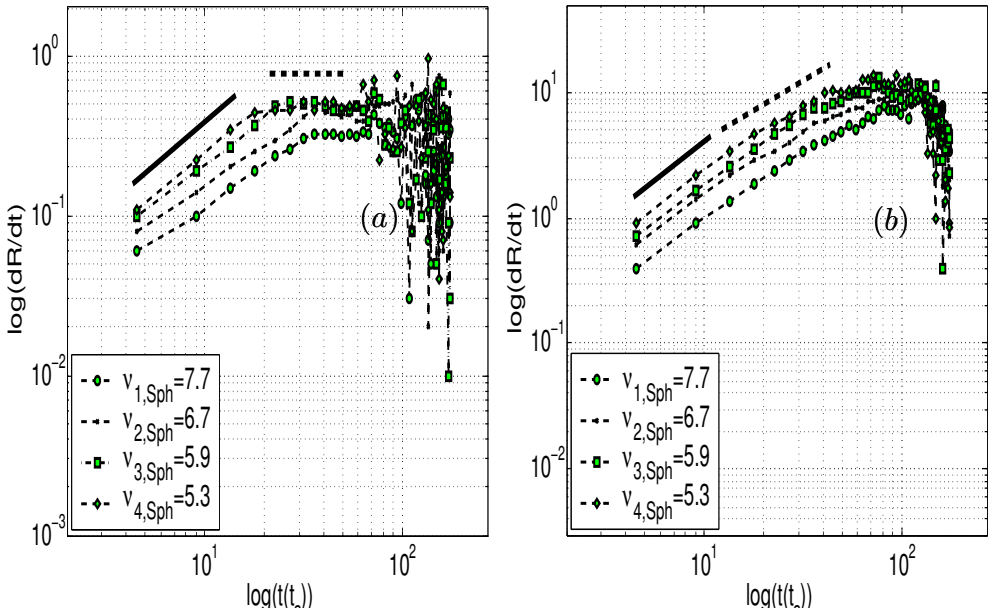

Figure 8.9: The figures show the parallel $\|$ (b) and perpendicular $\perp$ (d) components of the time derivative of the M.S.D. for spheres as the kinematical viscosity is changed. The Reynolds number is 2×10^{-2}, the spheres radius $R_{equi} = 1.01$.

Change in the kinematical viscosity

Next we study the behavior of the system under changes in the kinematical viscosity. Figure 8.9 (a) and (b) shows the M.S.D. for spheres in the perpendicular ($\perp$) and parallel ($||$) components. Figure 8.9 (a) shows well defined ballistic and simple diffusive regimes. The plots show a slight increment in time for the simple diffusive regime as the kinematical viscosity decreases. Also, there is a clear upward shifting as the kinematical viscosity decreases. The spheres increase their M.S.D. as the kinematical viscosity becomes smaller.

In the case of the parallel ($||$) component 8.9 (b), we found a ballistic and non-diffusive regimes. The exponent α for the non-diffusive behavior is the same in all the curves and $\alpha = 1.4$ (Rouyer et. al. (1999)). Such as for the perpendicular ($\perp$) component, the upward shifting is also present for the parallel ($\|$) component.

The ellipsoids system is studied under the same kinematical viscosity variations. Figure 8.10 shows the behavior of the perpendicular ($\perp$) (a) and parallel ($\|$) (b) components of the M.S.D..

The perpendicular component (see figure 8.10 (a)) exhibits ballistic and non-diffusive behavior. The curves, as in the case of spheres, show an upward shifting as the kinematical viscosity decreases. As the viscosity decreases the exponent α for the non-diffusive regime becomes gradually much smaller: $\nu = 7.7 \rightarrow \alpha = 2.4$ to $\nu = 5.0 \rightarrow \alpha = 2.1$.

For the parallel component ($\|$), the difference between the ballistic and the non-diffusive behavior is not pronounced, and for the lower kinematical viscosity $\nu = 5.0 \rightarrow \alpha = 2.0$ the non-diffusive behavior in the system practically disappears.

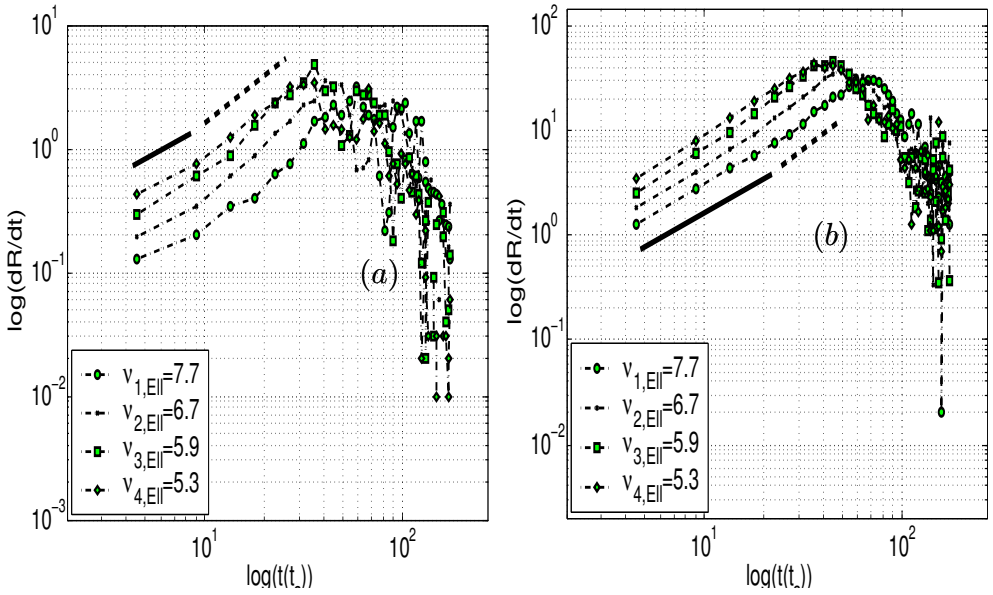

Figure 8.10: The figures show the parallel $\|$ (a) and perpendicular $\perp$ (c) components of the time derivative of the M.S.D. for ellipsoids as the kinematical viscosity is changed. The Reynolds number is 2×10^{-2}, the ellipsoid aspect-ratio is $\Delta r = 0.4/1.6$.

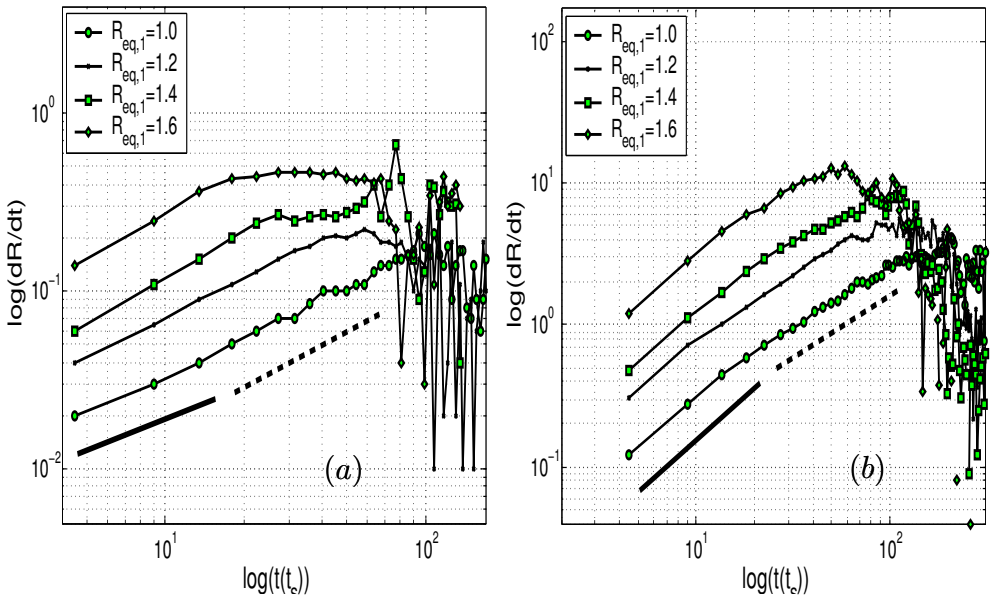

Figure 8.11: The figures show the perpendicular $\perp$ (a) and parallel $\|$ (b) components of the time derivative of the M.S.D. for spheres as the sphere radius changes. The Reynolds number is 2×10^{-2}.

Change in the ellipsoid aspect-ratio and sphere radius

In the case of variations of the equivalent radii, eq. (3.28), figure 8.11 shows the behavior of the parallel ($\|$) and perpendicular ($\perp$) components. As the equivalent radii decreases,

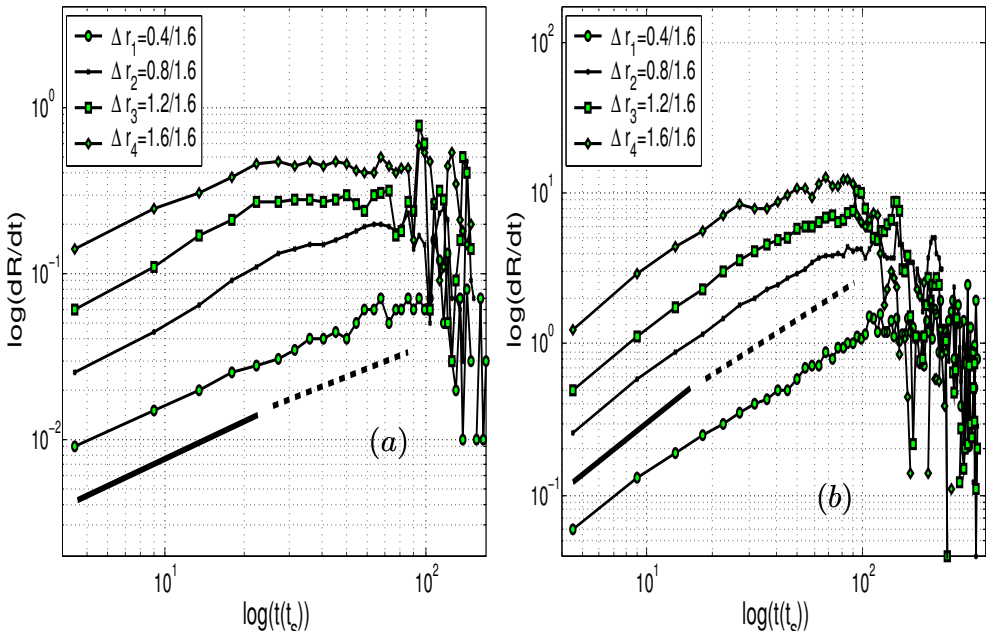

Figure 8.12: The figures show the perpendicular $\perp$ (a) and parallel $\parallel$ components of the time derivative of the M.S.D. for ellipsoids as the ellipsoid aspect-ratio changes. The Reynolds number is 2×10^{-2}.

we can see in figure 8.11 (a) the same kind of upward shifting in the curves, as viscosity or density, is changed in the system. As the sphere radius is increased the presence of the simple diffusive regime is increased during a very long time.

For the perpendicular ($\perp$) component, all the curves look quite similar to each other, with a slight difference being that for spheres with $R_{eq} = 1.6$ the approach to the saturation regime is much faster than in the case of $R_{eq} = 1.0$. The exponent α for this non-diffusive regime is $\alpha = 1.4$.

In figure 8.12 (a) and (b) we present the M.S.D. behavior for ellipsoids as the aspect-ratio is changed. Here we want to draw attention to an interesting change from a non-diffusive regime to simple diffusive behavior that can be observed in the perpendicular ($\perp$) component (see figure 8.12 (a)) as the ellipsoid aspect-ratio tends to one ($\Delta r \rightarrow 1$, sphere). The slope of the curve in the non-diffusive part changes from ($\Delta r = 0.25, \alpha = 2.2$) to ($\Delta r = 1, \alpha \approx 0$).

Furthermore, in the parallel component (see figure 8.12 (b)), we can see the change in the slope that characterizes the variation from non-diffusive behavior for ellipsoids to the non-diffusive behavior for spheres ($\Delta r \rightarrow 1$). The exponents goes from ($\Delta r = 0.25, \alpha = 2.3$) oblate ellipsoids to ($\Delta r = 1, \alpha = 1.4$, Rouyer et. al. (1999)) spheres.

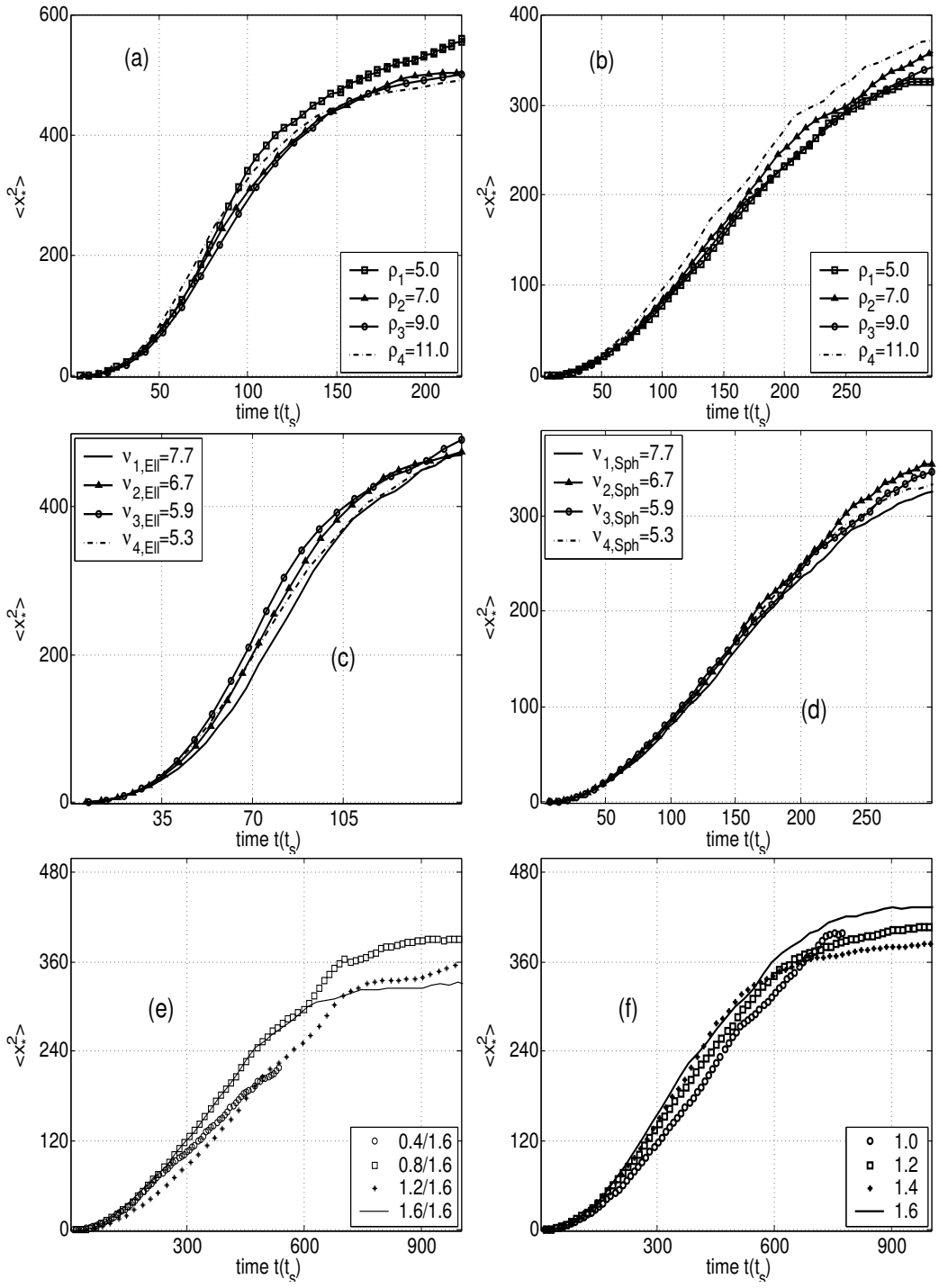

Figure 8.13: We show the collapse of the curves from fig 7.3. All the curves collapse quite well justifying the transformation rule, table 7.1.

8.2.4 Similarity

In table 8.1, we present the transformation rules that are used to collapse the pictures, presented in figure 8.3. The Reynolds number Re is left invariant by the transformations.

Time	$\rightarrow$	Adimensional Time	
t	$\rightarrow$	$\frac{t}{t_s}$	
$< x^2 >$	$\rightarrow$	$\frac{<x^2>}{4R_{eq}^2}$	
v	$\rightarrow$	$\frac{v}{v_s}$	

Table 8.1: Transformation rules in sedimentation.

These results, however, only hold for small Reynolds numbers $Re \lessapprox 10^{-2}$, since there is no analytical expression to account the terminal settling velocity, at moderate Reynolds numbers. Therefore, it is impossible to compute the Stokes time, eq. (3.30) at moderate Re.

8.3 Outlook and Conclusions

In this chapter, the diffusion of oblate ellipsoids in sedimentation was studied. We have found a non-diffusive behavior in both components (parallel and perpendicular), which is completely new and not reported in the literature. Our comparison with the equivalent sphere system to ellipsoids shows that there is a simple diffusive process for the perpendicular and a non-diffusive process for the parallel components. This result regarding the diffusive behavior in spheres agrees with the work of (Rouyer et. al. 1999) and (Miguel and Pastor-Satorras 2001).

In addition, the behavior for ellipsoids and spheres was investigated as the particle density, kinematic viscosity and ellipsoid aspect-ratio or sphere radii were changed. It was found that the increment of the inertial forces, by means of the growth in particle density or the decreasing in the kinematical viscosity, reduces the presence of the diffusive behavior, and the system goes faster from the ballistic to the saturation regime. When the sphere radii are changed, we could observe a similar behavior: As the sphere radius is increased the inertia grows and thus also the particle M.S.D..

It is important to point out the behaviour of the time derivative of the M.S.D. in both components as the aspect-ratio changes (see figure 8.12). For the vertical component, with the growth of the aspect-ratio the M.S.D. goes from the non-diffusive behavior to the simple diffusive regime. In the parallel component, the exponent α for non-diffusive regimes changes for ($\alpha = 2.2, \Delta r = 04/1.6$) flattened ellipsoids to ($\alpha = 1.4, \Delta r = 1$) spheres.

Last, we found a similarity law for the sedimentation process which is valid at small Reynolds numbers. It is presented in table 8.1.

Chapter 9

Velocity Fluctuations

In this last chapter we examine the dynamical behavior of sedimenting ellipsoids and spheres under changes of the container size. In the first section we study the influence on the spatial correlations as the particulate volume fraction is changed, comparing the results for ellipsoids and spheres. We also present the study of the velocity fluctuations as a function of the volume fraction. After that, we investigate the divergence of the velocity fluctuations as the container size is changed. Finally, we summarize.

We choose the density of the fluid, the Stokes velocity and the larger radius of the ellipsoid equal to unity in our system. In all of the cases, the container height is $L = 150$ and a square base of side $L = 22$ extended up to $L = 176$, and a lattice constant of $h = 0.7$. The ratio between the density of the oblate ellipsoids and the fluid is 4.

9.1 Spatial correlations

We start our analysis by studying the spatial correlations in the velocity fluctuations (hereafter SCVF). The normalized autocorrelation function of the parallel ($||$) component of the velocity fluctuations are defined as, (Segré et. al. (1997)):

$$C_{\parallel}(\mathbf{r}) \equiv \frac{\langle \delta v_{\parallel}(0) \delta v_{\parallel}(\mathbf{r}) \rangle}{\langle \delta v_{\parallel}(0)^2 \rangle} \tag{9.1}$$

1cm where the brackets $\langle ... \rangle$ represent an ensemble average over several individual different configurations in space and orientations (ellipsoids). Where $\delta \mathbf{v}_i = \mathbf{v}_i - \mathbf{v}_{sed}$, represents the fluctuations in the velocity and $\mathbf{v}_{sed} = \langle v_i \rangle$ is the mean velocity over the configuration. If the distance $\mathbf{r}$ is taken in the direction parallel to gravity, x, then we call the parallel $C_{\parallel}$ or perpendicular, y, $C_{\perp}$ component.

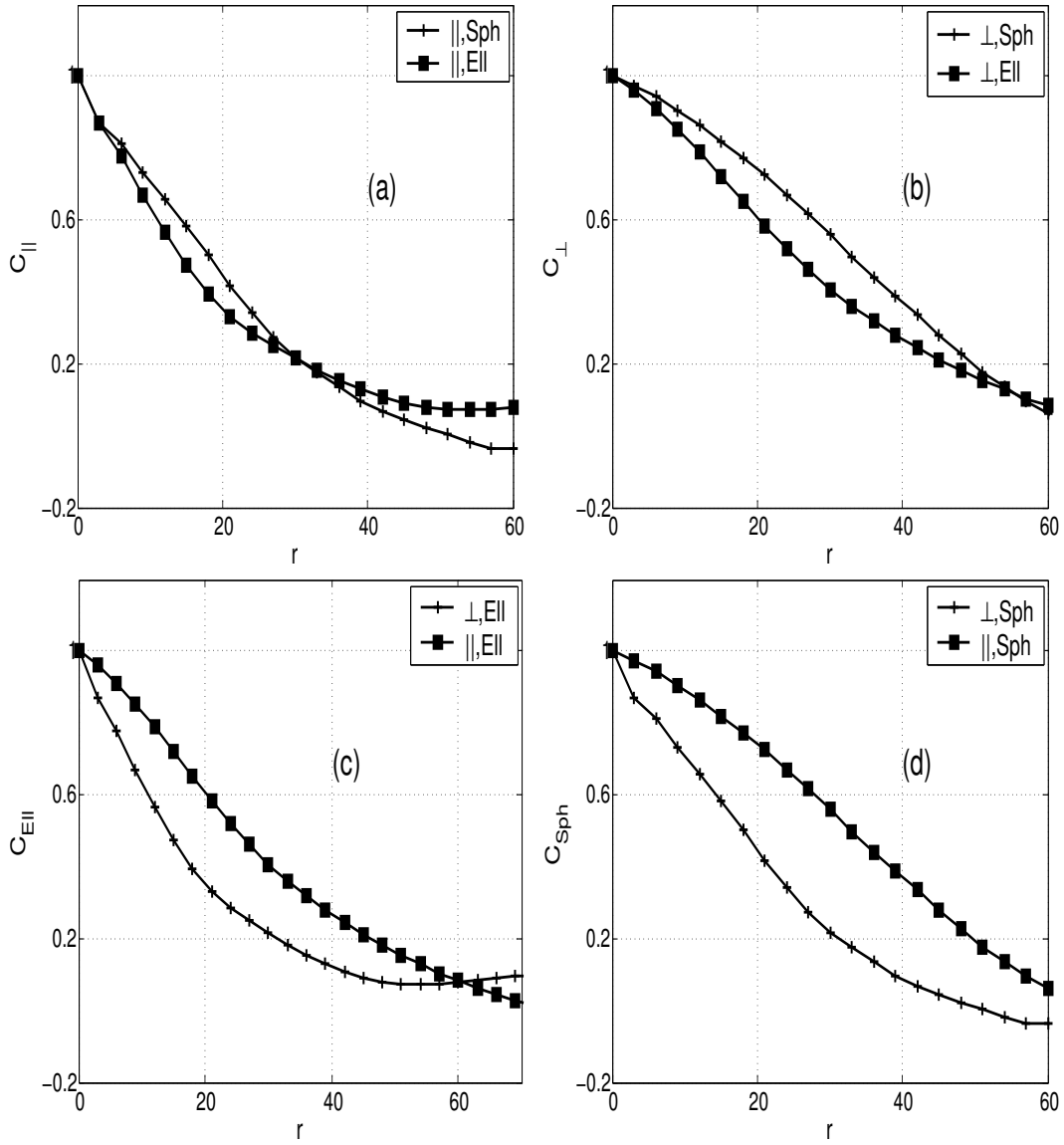

Figure 9.1: The figures show the parallel $\parallel$ (a) and perpendicular $\perp$ (b) components of the SCVF for ellipsoids and spheres. Figures (c) and (d) compare the parallel and perpendicular components for ellipsoids and spheres, respectively. The Reynolds number is 2×10^{-2}, the spheres radius $R_{equi} = 1.01$ and the ellipsoid aspect-ratio is $\Delta r = 0.4/1.6$.

9.1.1 Change in the volume fraction

In figure 9.1, we present the spatial correlations of velocities for ellipsoids and spheres. Figure 9.1 shows the comparison between the parallel (a) and perpendicular (b) components for spheres and ellipsoids. In figures (a) and (b) the components for spheres show a much faster relaxation than ellipsoids. Figures (c) and (d) exhibit the anisotropy, characteristic to the sedimentation process, with a slower decay of the parallel component of the velocity autocorrelation funtion. This anisotropy is present in both spheres, (Nicolai and Guazelli (1995), Segré et. al. (1997), Höfler (2000)) and ellipsoids.

We present the SCVF for the parallel ($\|$) and perpendicular ($\perp$) components fig. 9.2 for spheres (a,b) and ellipsoids (c,d) corresponding to four representatives volume fractions $\Phi_V = 0.02, 0.04, 0.08, 0.16$. The anisotropy between the components is also present as the volume fraction Φ_V increases as is shown in fig. (a) and (b).

The $\|$ component of the SVCF for spheres (see figure 9.2 (a), approximately follows an exponential decay, as $C_{||} \approx exp(-z/\xi_{\|,sph})$, (Nicolai and Guazelli (1995), Segré et. al. (1997), Höfler (2000)). On the other hand, the $\perp$ component (see figure 9.2 (b)) shows a rapid initial decay in a region of different negative values. This minimum defines the value of the correlation length, $\xi_{\perp,sph}$ in the system. Segré et. al. (1997) measured the dependence of the correlation length in the ($\perp$) component as $\xi_{\perp,sph} = 27a\Phi^{-1/3}$, and for the ($\|$) one $\xi_{\|,sph} = 11a\Phi^{-1/3}$, where a is the sphere radius (in our notation $a = R_{eq}$) and Φ the volume fraction.

In order to make our simulations comparable with the experimental results of Segré et. al. (1997) and also with previous simulations, Höfler (2000), we use a system size of squared base with a side 144 and height 150 and a volume fraction of $\Phi_V = 0.03$. Segré et. al. (1997) show that the correlation length of the perpendicular component ($\perp$) becomes $\xi_{\perp,sph} \approx 73a$ for $\Phi_V = 0.05$. In our simulations, we find a correlation length for the equivalent spheres of the order of $\xi_{\perp,sph} \approx 78a$.

In the case for ellipsoids the correlation length (fig. 9.2), with regard to the parallel (c) and perpendicular (d) components, we see a larger value of the correlation length in the parallel component $\xi_{\perp,sph} \approx 87a$ whereas the perpendicular component does not show an appreciable difference.

9.1.2 Collapsing of the spatial correlations

Figure 9.3 (a) and (b) show the collapsing of the SCVF for spheres, in both components, scaling the distance with $R_{eq}\Phi_V^{-1/3}$ as was proposed by Segré et. al. (1997). The collapse works quite well, and we consider it noteworthy that it is valid for changes of the volume fraction by up to 60 times. The correlation lengths that we found are:

$$\xi_{\perp,sph} = 29R_{eq}\Phi_V^{-1/3}; \xi_{\|,sph} = 13R_{eq}\Phi_V^{-1/3} \tag{9.2}$$

which does not really differ from the results of Segré et. al. (1997).

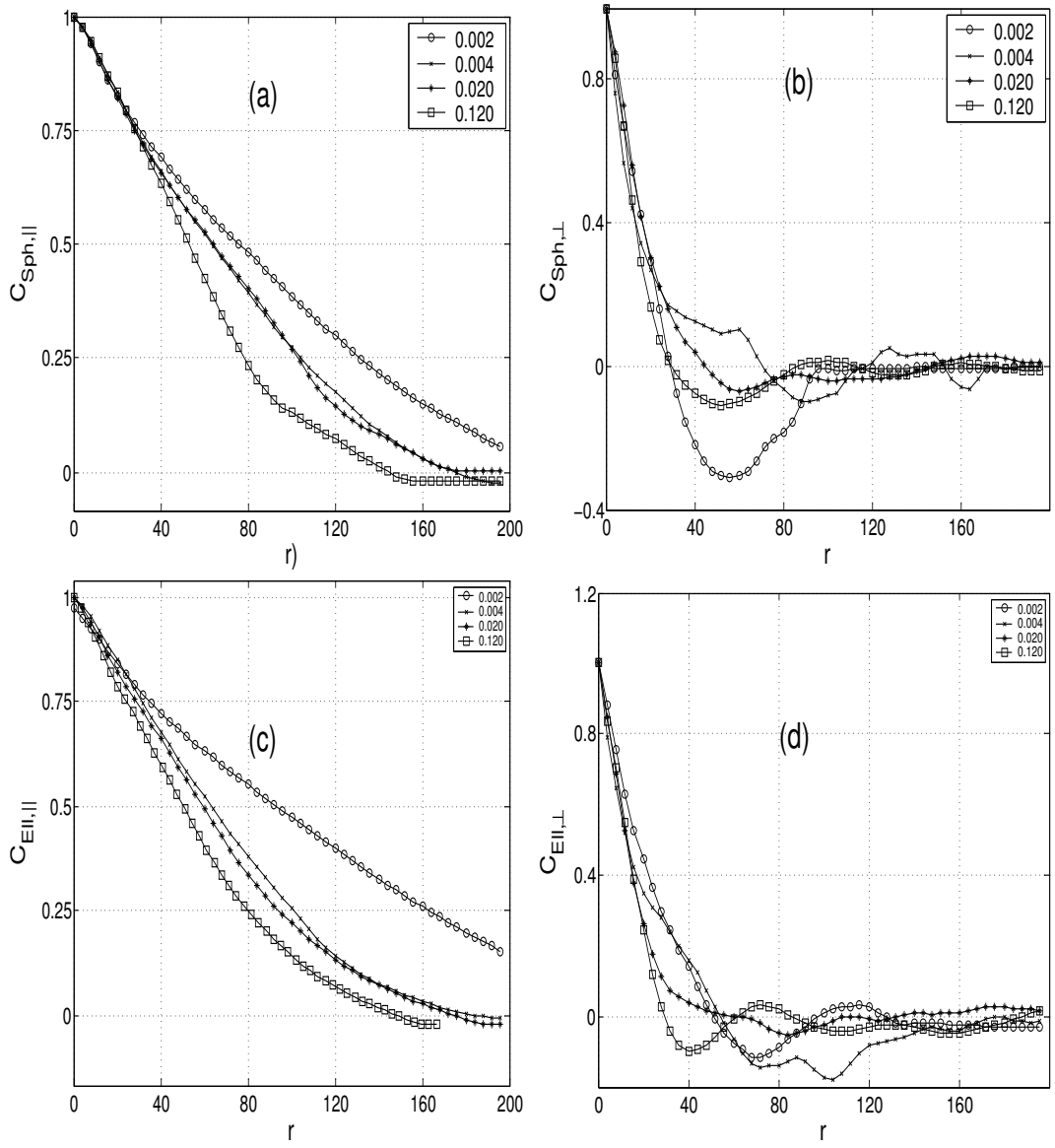

Figure 9.2: Spatial correlations functions in the parallel (a,c) and perpendicular (b,d) components of the SCVF for ellipsoids and spheres, with changes of the volume fraction. The Reynolds number is 2×10^{-2}, the spheres radius $R_{equi} = 1.01$ and the ellipsoid aspect-ratio $\Delta r = 0.4/1.6$.

In the ellipsoid case (see figure 9.3), we present the SCVF for the parallel (c) and perpendicular (d) component, respectively. The collapse also works well in this case. The values for the correlation length are the following:

$$\xi_{\perp,Ell} = 25 R_{eq} \Phi_V^{-1/3}; \xi_{\parallel,Ell} = 10 R_{eq} \Phi_V^{-1/3} \tag{9.3}$$

The correlation length for ellipsoids, in both components, is smaller than for spheres.

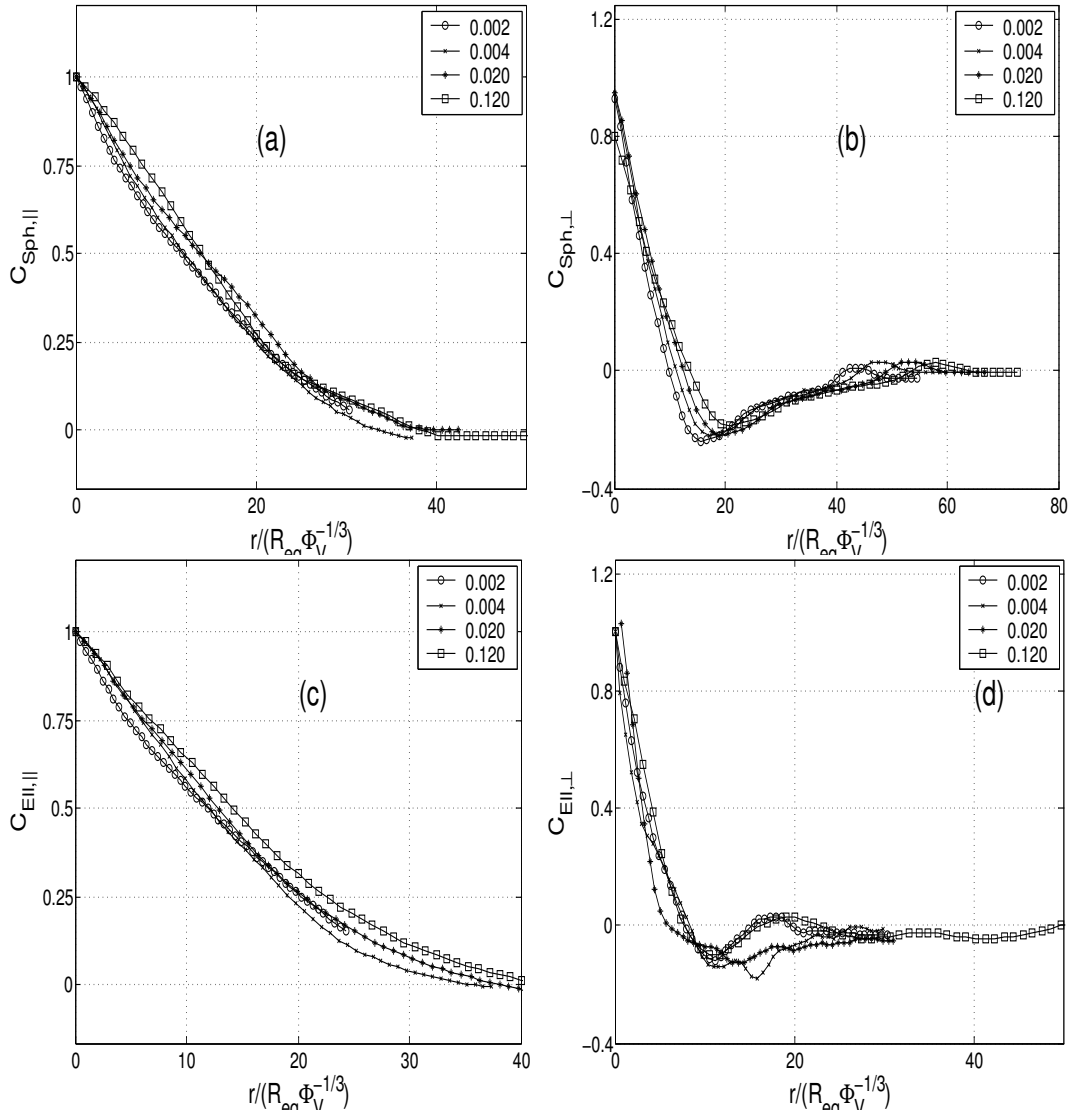

Figure 9.3: Collapsing of the spatial correlations function for data in fig. 8.2.

The amplitude in the parallel ($||$) and perpendicular ($\perp$) components of the velocity fluctuations (see chapter 6 eqs. 6.1 and 6.2), is presented in figure 9.4. The figures are presented in a log-log scale. For $0.005 \leq \Phi_V \leq 0.07$, the velocity fluctuations grow linearly as $\approx \Phi_V^{1/3}$ (straight line superimposed on data), as for spheres as well as for ellipsoids (Segré et. al. (1997)).

For larger volume fractions ($\Phi_V > 0.07$), the fluctuations are reduced in both components, for spheres and for ellipsoids. The decrease in the velocity fluctuations as the volume fraction increases could be explained by the growth of the particle encounters, since the container has a fixed volume and the particle encounters are a dissipative process in nature. Therefore the velocity fluctuations tend to reduce (Kalthoff et. al. (1996)).

It was mentioned in chapter 6 above, that the velocity fluctuations components for spheres are much larger than for ellipsoids. The appearance of rotations around the ellipsoid

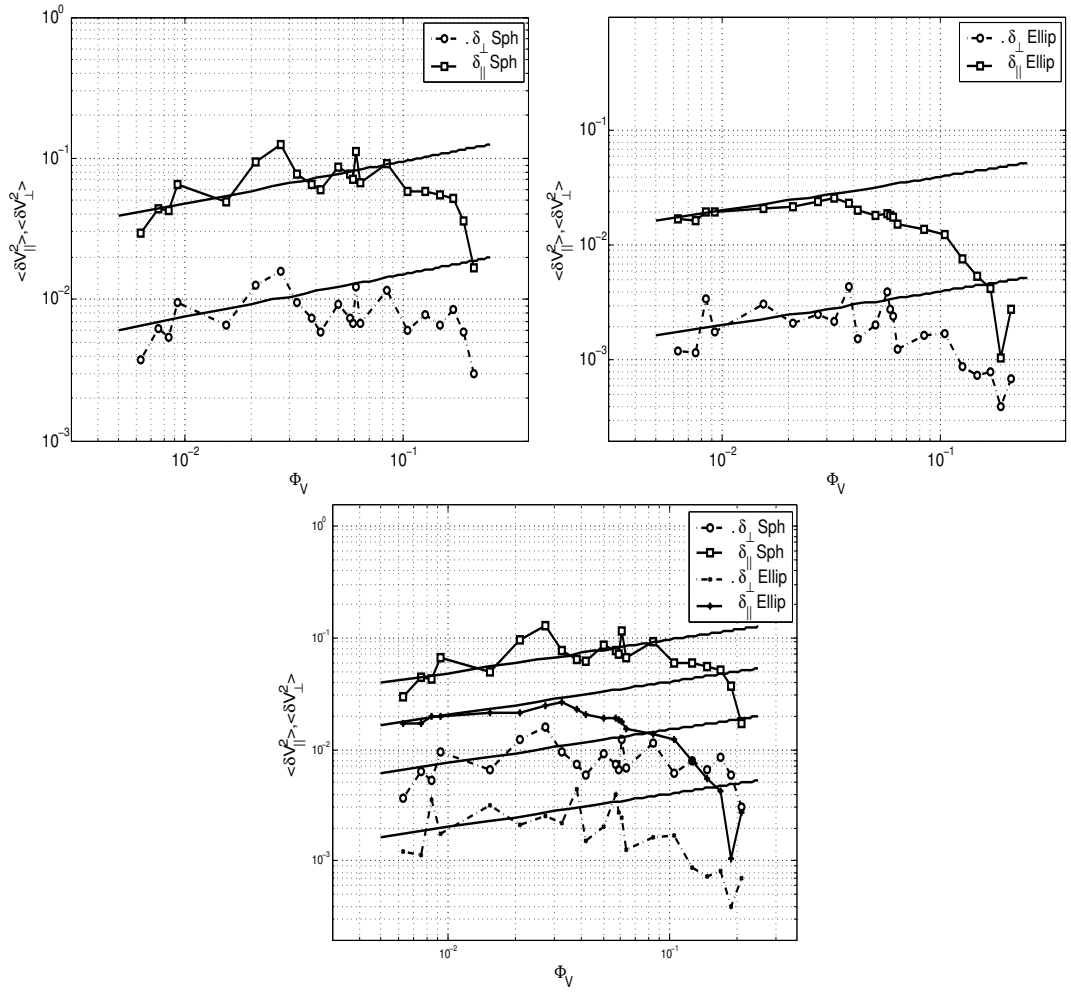

Figure 9.4: The top pictures present the velocity fluctuations for spheres and ellipsoids in the parallel ($\|$) and perpendicular ($\perp$) components as a function of the volume fraction, in a log-log scale. The bottom picture compares the results for both kinds of particles and components. The Reynolds number is 2×10^{-2}, the spheres radius $R_{equi} = 1.01$ and the ellipsoid aspect-ratio $\Delta r = 0.4/1.6$.

center of mass, implies a work against the fluid, then the dissipation of energy is present now for translational and rotational degrees of freedom. Therefore, the decrease of the velocity is more dramatic for ellipsoids than spheres.

9.2 Change of the container size

In the previous section we examined the system as the volume fraction increases with a fixed container side of 176 where the characteristic correlation length was found, eqs. 9.2 and 9.3.

Now we turn to the analysis of the effects of variations in the container size on the velocity

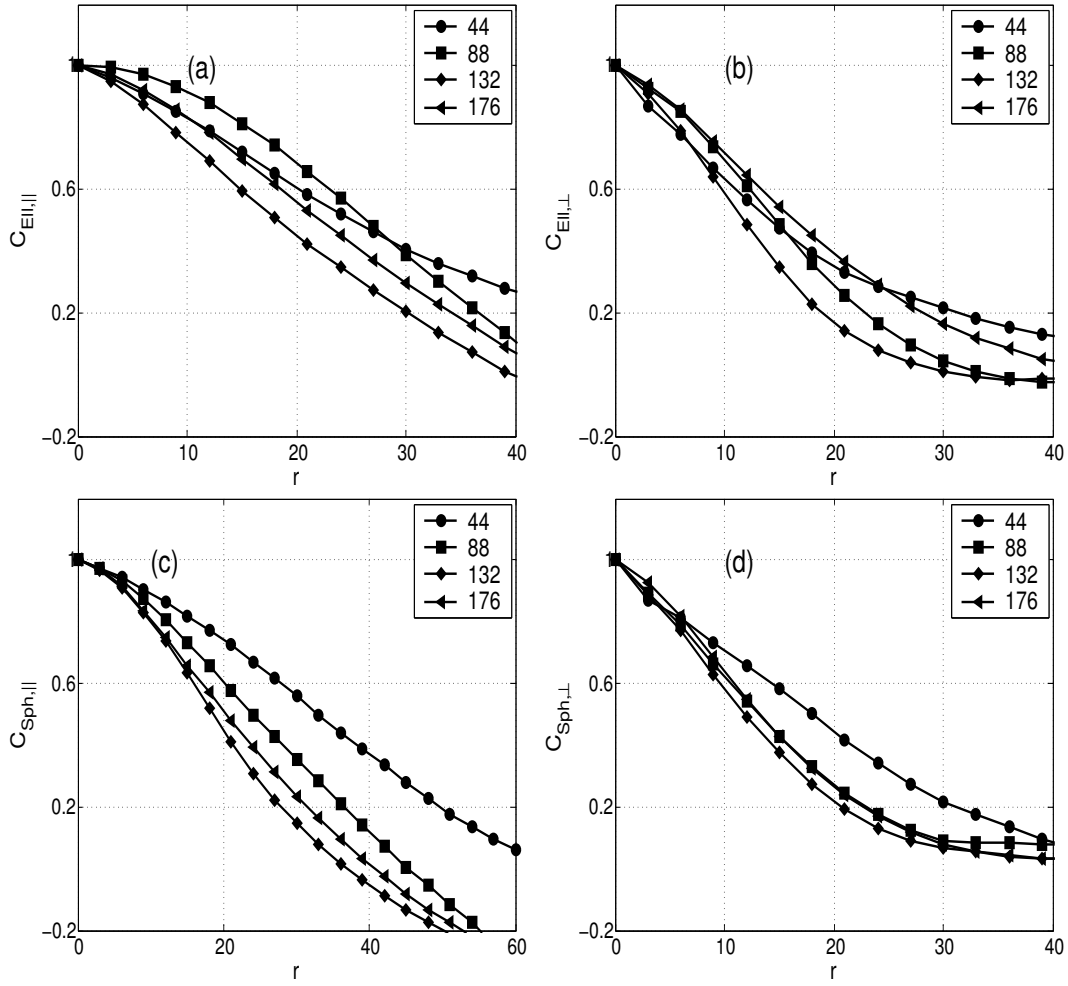

Figure 9.5: Spatial correlation functions for the parallel $\|$ (a,c) and perpendicular $\perp$ (b,d) components of the velocity fluctuations for ellipsoids (a,b)and spheres (c,d) as a function of the container side. The Reynolds number is 2×10^{-2}, the spheres radius $R_{equi} = 1.01$ and the ellipsoid aspect-ratio $\Delta r = 0.4/1.6$.

fluctuations, as examined in the work by (Segré et. al. (1997) and Höfler (2000)). We use a small container size (close to the characteristic correlation length), in order to investigate the size effects on the fluctuations.

In figure 9.5, we show the SCVF for spheres (a,b) and ellipsoids (c,d) as the container size is increased. The correlation length $\xi_{\perp,sph}$ for spheres and ellipsoids decreases in both components as the container increases. However, the decay for spheres is larger than the decay for ellipsoids in the parallel component. The perpendicular component, on the other hand, does not display any difference.

We also measure the pair correlation function as the container side is changed (see figure 9.6). For spheres and ellipsoids we find in the pair correlation for all container sizes, a characteristic length of the order ≈ 2, followed by a monotonic decay that increases with the container side (see figure 9.6 (a) and (b)). It is interesting to point out that the ratio of

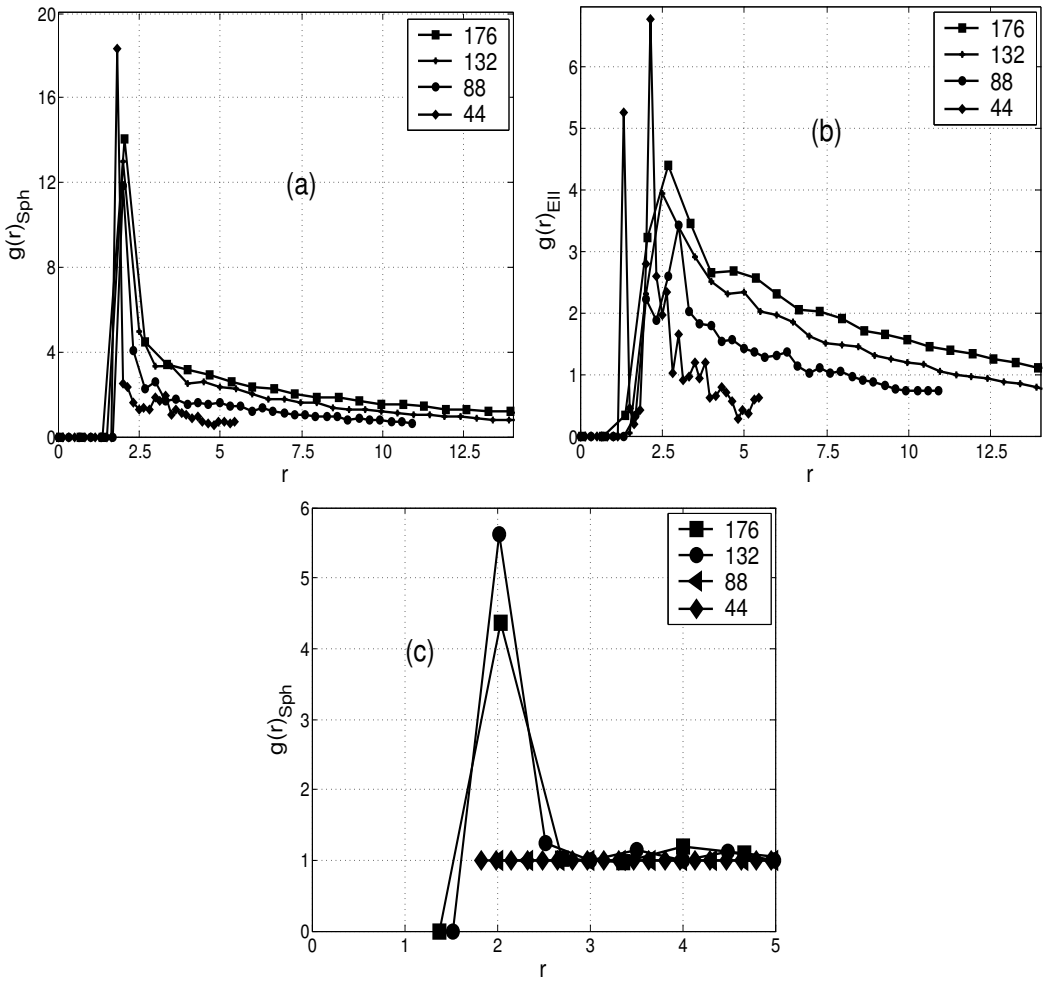

Figure 9.6: Pair correlation function for spheres (a), and ellipsoids (b) and the ratio of the spheres to ellipsoids (c).

the pair correlation for spheres to that of the ellipsoids exhibits higher peak for the larger container side 176.132 (see 9.6 (c)). This peak reveals much larger density fluctuations for spheres than for ellipsoids. The behavior of the pair correlation functions resemble the pair correlation function for liquids, where the positions of neighboring molecules are strongly correlated, leading to a modulation of the pair correlation functions (Barrat and Hansen (2003)), which is very similar to that presented in figure 9.6 (a) and (b).

In order to investigate size effects in the velocity fluctuations, we undertake variations from the correlation length, as in the work of Segré et. al. (1997). The results are present in figure 9.7 for spheres (dash dotted line) and ellipsoids (dash continuous line). The container side are normalized by $L/(R_{eq}\Phi^{-1/3})$. The velocity fluctuations $< \delta V_{\perp,\parallel}/v_s >$ present an initial transition region, which have a strong dependence on the container side (Segré et. al. (1997) and Höfler (2000)), between $20 \leq L/(R_{eq}\Phi^{-1/3}) \leq 100$, after it, the simulation data are independent of the container side. In general, the ellipsoids and spheres show a similar behavior, but with a smaller overall value for ellipsoids. The ratio of the parallel $\parallel$ velocity fluctuation to the perpendicular $\perp$ component, for spheres and

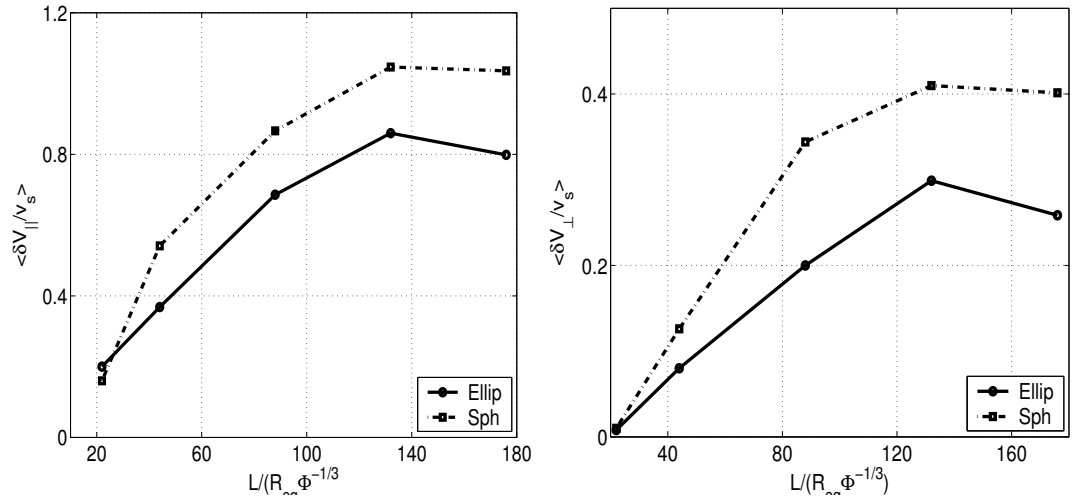

Figure 9.7: The left graphic show the parallel component of velocity fluctuations as the container side is changed. The right picture shows the vertical component. The Reynolds number is 2×10^{-2}, the spheres radius $R_{equi} = 1.01$ and the ellipsoid aspect-ratio is $\Delta r = 0.4/1.6$.

ellipsoids is ≈ 2.5, in agreement with Segré et. al. (1997).

This equal value for both kind of particles, reveals that the anisotropic behavior on the velocity fluctuation components are independent on the particle shape. The symmetry breaking induced by gravity acts equally on spheres and ellipsoids.

As is discussed in chapter 1 and by Caflish and Luke (1985), the velocity fluctuations might diverge with increasing container size. On the other hand, experiments, simulations and theory sec. 1.6 have found no evidence for such divergence. In a previous work, Höfler (2000), it is argued that systems, bounded by walls, do not show a comparable scaling of velocity fluctuations but a saturation, if the smallest extension of the container exceeds a critical size, and then the difficulty to find a unique scaling law. In our simulations, the variations of the container size, were made by changing the entire squared base. The results, fig. 9.7 (a) and (b), don't present evidence for the divergence of the velocity fluctuations neither for spheres nor ellipsoids, and behave really close to the results given by Segré et. al. (1997).

9.3 Outlook and Conclusions

We studied the variation of the container size for spheres and ellipsoids sedimenting at small Reynolds number 2×10^{-2}. It was found that the spatial correlations of the vertical velocity for ellipsoids show a much slower decay as the perpendicular component. The equivalent sphere system reproduces the same anisotropy, this matching rather closely to the results of Segré et. al. (1997).

The collapsing employed in the spatial correlations for $\Phi_V \leq 0.1$ works quite well for

both spheres and ellipsoids, fig. 9.3 and 9.1. The correlation length for ellipsoids have a smaller value than for spheres, eq.9.2 and 9.3.

The velocity fluctuations, for both kinds of particles, also reveal the anisotropy present in the spatial correlations. The collapse transformation used by Segré et. al. (1997), at $\Phi_V \leq 0.1$, agrees quite well with our data, fig. 9.4. After $\Phi_V > 0.1$, all the velocity fluctuations decrease. It is important to remark, that the velocity fluctuations for spheres are much larger as for ellipsoids.

Chapter 10

Conclusion

The aim of this thesis is the study of sedimentation of oblate ellipsoids using a numerical simulation technique Höfler and Schwarzer (2000), which is applyed to the case of one oblate ellipsoid at low and high Reynolds number and many oblate ellipsoids at low and moderate Reynolds number, in three dimensions.

10.1 One Oblate ellipsoid

The motion of a piece of paper or a leaf, as it falls to the ground, is an old and unsolved problem in Physics. Maxwell, Helmholtz and Kelvin are just some who have studied this problem. Recent experiments (Field et. al. (1997) and Belmonte et. al. (1998)) and simplified models Mahadevan (1996), confirm that the motion of falling objects is still far from being understood.

In our work the falling objects are considered a very flat oblate ellipsoid, such as leaves or a sheet of paper, settling in a fluid, in a three dimensional container. We found three basic regimes for the dynamics of the system (steady-falling, oscillatory-periodic, and chaotic).

The steady-falling exhibits a similar physical behaviour as observed experimentally by Field et. al. (1997) and Belmonte et. al. (1998). We have characterized the dynamics of the steady-falling regime when the kinematic viscosity, dropping height, and oblate's aspect-ratio are changed. Some conclusions can be drawn from this part of the work. This regime is present for small values of $I^\star \approx 0.5 - 1$, $Re \approx 100$ and is shown in fig.5.1-5.4.

The periodic behaviour in our simulations is found for $Re \sim 400$ and small aspect-ratios $(\Delta r \leq 0.1)$. The vertical orientation, Θ oscillates with double the period of oscillation of the vertical velocity v_y and at the same period of the horizontal velocity v_x. This periodic motion has also been observed experimentally by Belmonte et. al. (1998), showing that our simulations are essentially correct.

We find that our results in the case of the steady-falling and oscillatory phases, are in good qualitative agreement with the simplified model proposed by (Mahadevan (1996)).

The chaotic behaviour is present for larger aspect-ratios ($\Delta r \geq 0.3$) and in the entire range of Reynolds numbers used in this work. The separation between the spatial trajectories of the falling oblate ellipsoid diverges for small variations in the initial orientation Θ_o, and grows exponentially in time. The value found for the Lyapunov exponent is $\lambda = 0.052 \pm 0.005$. It is worthwhile to point out that we give a quantitative measure of the sensitivity to small changes in the initial state of the system.

For the steady-falling and oscillatory regime we obtain a similarity law, which is a direct consequence of the invariance of the Reynolds and Froude numbers. Also, the similarity expresses the independence of the physical results of the grid size, which is a good test for the dynamics of these two regimes.

We construct a phase diagram that shows three well-defined dynamic regions as is also shown by Field et. al. (1997). The difference with the above reference is that the chaotic behaviour is associated with the transition to chaos through intermittency which is not seen in our simulations. The phase diagram is independent of the initial orientation.

The transition for steady-falling to oscillatory and the transition from steady-falling to chaotic regime can be understood as second and first order phase, respectively and the characteristic transient time and its inverse being the order parameter, respectively.

10.2 Many ellipsoids sedimentation

We have simulated the sedimentation of oblate ellipsoids at small volume fraction ($\Phi_V \leq 0.2$) and small Reynolds number ($Re \approx 10^{-2}$). We have found that at intermediate volume fraction the settling velocity exhibits a local maximum which to our knowledge has never been reported in the literature.

We also present data at moderate Reynolds number ($Re \approx 7$) for the sedimentation velocity of oblate ellipsoids wich follows a monotonic behaviour as the volume fraction Φ_V is increased. As in the case of low Reynolds number the ellipsoids have a smaller sedimentation velocity than the equivalent spheres. The data for ellipsoids and spheres follow the Richardson-Zaki law (1954) with exponents ($n_{Ellip} \approx 3.2$,$Re = 10^{-2}$) and ($n_{Sph} \approx 4.0$,$Re = 7$) respectively.

In addition, the local maximum, at low Reynolds number, in the velocity can be related to the non-monotonic behaviour of the vertical orientation of the ellipsoids along gravity, and can be explained by the "cluster" formation. This non-monotonic behaviour is also found in fiber-like suspensions Herzhaft and Guazzelli (1999). At moderate Re there is also a larger alignment of ellipsoids with gravity, compared to those with small Reynolds number. The alignment with gravity is present also at moderate Reynolds number, which is in agreement with the orientational behaviour of a single ellipsoid Fonseca and Herrmann ((1) 2004).

At low Reynolds number the orientational order parameter Ψ vanishes around $\Phi_V \approx 0.08$ fig. 7.7. As Φ_V decreases the orientational alignment with gravity increases. For low Reynolds number in the limit $\Phi_V \rightarrow 0$ a single ellipsoid aligns with gravity. The

alignment with gravity is a distinctive feature of the steady-state regime for a single oblate ellipsoid as reported in references Fonseca and Herrmann ((1) 2004) and Galdi et. al. (2001). The vanishing of the order parameter, at moderate Re, is slightly shifted ($\Phi_V \approx 0.1$) to the right as the Reynolds number increases (see fig 7.12, bottom). All the simulations in this work are located in the steady-falling phase for a single oblate ellipsoid.

The diffusion of oblate ellipsoids in sedimentation was studied. We have found a non-diffusive behaviour in both components (parallel and perpendicular), which is completely new and not reported in the literature. Our comparison with the equivalent sphere system to ellipsoids shows that there is a simple diffusive process for the perpendicular and a non-diffusive process for the parallel components. This result regarding the diffusive behaviour in spheres agrees with the work of (Rouyer et. al. 1999) and (Miguel and Pastor-Satorras 2001).

Furthermore, the behaviour for ellipsoids and spheres was investigated as the particle density, kinematics viscosity and ellipsoid aspect-ratio or sphere radii were changed. It was found that the increment of the inertial forces, by means of the growth in particle density or the decreasing in the kinematics viscosity, reduces the presence of the diffusive behaviour. When the sphere radii are changed, we could observe a similar behaviour: as the sphere radius is increased the inertia grows and thus also the particle M.S.D..

The vertical component of the M.S.D. passes from the non-diffusive behaviour to the simple diffusive regime as the aspect-ratio increases. For the parallel component, the exponent α for non-diffusive regimes changes for ($\alpha = 2.2$) flattened ellipsoids to ($\alpha = 1.4$) spheres.

Last, we found a similarity law that collapse quite well the diffusion process and it is valid at small Reynolds numbers.

We studied the variation of the container size for spheres and ellipsoids sedimenting at small Reynolds number 2×10^{-2}. It was found that the spatial correlations of the parallel velocity for ellipsoids show a smaller decay as the perpendicular component. The equivalent spheres system reproduces the same anisotropy, this matching rather closely to the results of Segré et. al. (1997).

The collapsing employed in the spatial correlations for $\Phi_V \leq 0.1$ works quite well for spheres and ellipsoids. The correlation length for ellipsoids has a smaller value than for spheres.

The velocity fluctuations for ellipsoids reveal the anisotropy present in the spatial correlations. The collapse transformation used by Segré et. al. (1997), at $\Phi_V \leq 0.1$, agrees quite well with our data. After $\Phi_V > 0.1$, all the velocity fluctuations decreases. It is important to remark, that the velocity fluctuations for spheres are much larger as for ellipsoids.

10.3 Outlook

Despite the facts that falling bodies have been studied for such a long time, there are still many open problems. Using this model it is now possible to study the sedimentation of different types of particles and the structure of the fluid surrounding them. Future work could be addressed in several directions:

- The experiments (Willmarth et. al. (1964), Belmonte et. al. (1998) and Kelly and Wu (1997)) have confirmed, that the presence of vortices is fundamental, as the objects fall or rise in a fluid. Vortex generation is such an important part of fluid dynamics that a complete theory must be taken into account in order to understand the role of the fluid in the motion of falling objects. Then, a natural following work is to undertake a systematic research about the velocity and pressure fields in the dynamics of falling objects. This is a task that our algorithm is able to give.

- The autorotation or the angular motion that the flat object executes as it fall, is an important research in a large number of laboratory studies. The efforts come mainly by practical considerations in meteorology as the formation of hailstones; the dynamics of aircraft after it stall, etc. The autorotation has been found in some experiments (Field et. al. (1997) or Mahadevan et. al. (1999)) for very flat objects. Of particular note is the flat object can oscillate several times as it fell, increasing its amplitude in each oscillation until it completely turned over. The simulation of this type of motion requires that the thickness object (smaller ellipsoid diameter) has to be, at least of the order of the grid size. Therefore, the larger object diameter (small aspect-ratio) and the container size will imply a huge number of grid points in the simulation for the investigation of this motion. In order to carry out the simulation of autorotation, the above conditions must demand a high computational effort. The simulation technique used in this thesis in connection with the parallelized algorithm version can overcome these difficulties.

- In the dynamics of one falling flat object we found a similarity law for the steady-falling and oscillatory phases (Sections 5.1 and 5.2). The experimental data supporting these relations would be very important.

- We found a non-monotonic behaviour for the oblate ellipsoid settling velocity as the volume fraction increases. Also the increasing ellipsoid aligns with gravity as the volume fraction decreases. Finally in the dynamics of many ellipsoids sedimentation, we found an anomalous diffusion behaviour for the parallel component to gravity. Up to now, we don't know an experimental, simulation or theoretical result related with this settling law or anomalous diffusion, and an experimental work ratifying these behaviours is necessary.

- Suspensions in nature and industry generally involve the mixtures of particles of different types, shapes and sizes (e.g., oblate ellipsoids, prolate ellipsoids and spheres). The bidisperse suspensions are normally made of two different size spherical particles, but not alike shaped. In the statistical physics of bidisperse

hard-spheres mixtures is known (Asakura and Oosawa (1954)) the “depletion interaction”, which it is the effect of the large particles together increase the available volume, therefore the entropy, for the small particles. Then, the study of this “depletion interaction” due to the shape and not only to volume difference is another important task for accomplish.

References

Ackerson B. J., and Clark N. A. (1984). Shear-induced partial translational ordering of a colloidal solid. *Phys. Rev. A.*, *30*, 906.

Adams M. and Fraden S.(1998). Phase behavior of mixtures of rods (tobacco mosaic virus) and spheres (polyethylene oxide, bovine serum albumin). *Biophys. J.*, *74*, 669.

Adrian R.J.(1991). Particle-imaging techniques for experimental fluid mechanics. *Annu. Rev. fluid Mech. 23*, 261.

Allen M. P. and Tilsdesley D. J. (1987). Computer simulations of liquids. *Clarendon Press, Oxford, 1987*.

Aref H. and Jones S. W. (1993). Chaotic motion of a solid through ideal fluid. *Phys. Fluids A. 5*, 3026.

Asakura S. and Oosawa F.(1954). On interaction between two bodies immersed in a solution of macromolecules. *J. Chem. Phys. 22*, 1255.

Ballents L., Marchetti M.C. and Radzihovsky L. (1998). Nonequilibrium steady states of driven periodic media. *Phys. Rev. B. 57*, 7705.

Barrat, J. L. and Hansen, J. P.(2003). Basic concepts for simple and complex fluids. *Cambridge University Press, Cambridge, 2003*.

Basu A., Bhattacharjee J.K. and Ramaswamy, S.(1999). Mean magnetic field and noise cross-correlation in magnetohydrodynamic turbulence: results from a one-dimensional model. *Eur. Phys. J. 9*, 735.

Batchelor G. K (1970). The stress system in a suspension of force-free particles. *J. Fluid Mech. 41*, 545.

Batchelor G. K. (1970). Slender-body theory for particles of arbitrary cross-section in Stokes flow. *J. Fluid Mech. 44*, 419.

Batchelor G. K. (1972). Sedimentation in a Dilute Dispersion of Spheres. *J. Fluid Mech. 52*,part 2, 245.

Batchelor G. K.(1982). Sedimentation in a dilute polydisperse systeme of interacting spheres. Part 1. General theory. *J. fluid Mech. 119*, 379.

Batchelor G. K. and Janse Van Rensburg W.(1986). Structure formation in bidisperse sedimentation. *J. fluid Mech. 166*, 379.

Bauer M., Habip S., He D.R. and Martiensen W. (1992). New type of intermittency in discontinous maps. *Phys. Rev. Lett.. 68*, 1625.

Beenakker C.W.J., Van Saarloos W and Mazur,P.(1984). Many-Sphere Hydrodynamic Interactions III. The Influence of a Plane Wall. *physica A.. 127*, 451.

Belmonte A., Eisenberg H. and Moses E. (1998). From Flutter to Tumble: Inertial Drag and Froude Similarity in Falling Paper. *Nature*. *81*, 345.

Berne B. and Pecora R.(1990). Dynamic Light Scattering whit applications to Chemistry, Biology and Physics . *Malabar, Fl: Krieger*.

Biben T. and Hansen J.p.(1991). Phase separation of asymmetric binary hard-sphere fluids. *Phys. Rev.Lett.. 66*, 2251.

Bibette J.(1991). Depletion interactions and fractionated crystallization for polydisperse emulsion purification. *J. Colloid interface Sci.. 147*, 474.

Blake J. (1971). A note on the image system for a stokeslet in a no-slip boundary. *Proc. Camb. Phil. Soc.. 71*, 303.

Blanc R. and Guyon E. (1991). The physics of sedimentation. *La Recherche . 22*, 866.

Brady J.F. and Bossis G.(1985). The rheology of concentrated suspensions of spheres in simple shear flow by numerical simulation. *J. Fluid Mech. 155*, 105.

Brenner H. (1961). The slow motion of a sphere through a viscous fluid towards a plane surface. *Chem. Eng. Sci. 16*, 242.

Brenner M.P. (1999). Screening mechanisms in sedimentation. *J. Phys Fluids. 11,4*, 754.

Cowan M.L., Page J.H. and Weitz D.A (2000). Velocity fluctuations in fluidized suspensions probed by ultrasonic correlation spectroscopy. *Phys. Rev. Lett. 85(2)*, 453.

Chaikin P.M. and Lubensky T.C.(1998). Principles of Condensed Matter Physics. *New Cambridge university Press*.

Chandrasekhar S.(1981). Hydrodynamic and Hydromagnetic Stability. *New York: Dover*.

Chu X.L., Nikolov.A.D. and Wasan D.T(1996). Effects of interparticle interactions on stability aggregation and sedimentation in colloidal suspensions. *Chem. Eng. Comm.. 150*, 123.

Caflish R. E. and Luke J. H. C. (1985). Variance in the sedimentation speed of a suspension. *Phys. Fluids . 28(3)*, 759.

Das D. and Barma M.(2000). Particles Sliding on a Fluctuating Surface: Phase Separation and Power Laws. *Phys. Rev. Lett. 85*, 1602.

Davis R.H. and Hassen M.A.(1988). Spreading of the Interface at the Top of a Slightly Polydisperse Sedimenting Suspension. *J. Fluid Mech.. 196*, 107.

De Groot R. H. and Mazur P. (1984). Non-equilibrium thermodynamics. *New York: Dover*.

Debye P. and Hükel E.(1923). The theory of electrolytes. I. Lowering of freezing point and related phenomena. *Z. Phys. 24*, 185.

Einstein A. (1906). Investigatons on the theory of the Brownian movement. *Ann. Phys.. 19*, 289 .

Ertas D. and Kardar M.(1992). Dynamic roughening of directed lines. *Phys. Rev. Lett. 69*, 929.

Evans M.R., Kafri Y., Koduvely H.M and Mukamel D.(1998). Phase Separation in One-Dimensional Driven Diffusive Systems. *Phys. Rev. Lett. 80*, 425.

Fessas Y.P. and Weiland R.E...(1981). Convective solids settling induced by a buoyant phase *AIChE J.. 27*, 588.

Field S., Klaus M., Moore M. and Nori F. (1997). Chaotic dynamics of falling disks. *Nature*. *388*, 252.

Fogelson A. L. and Peskin C. S. (1988). A fast numerical method for solving the three-dimensional Stokes equations in the presence of suspended particles. *Journal of Computational Physics 79*, 50.

Fonseca F. and Herrmann H. (1) (2004). Simulation of the Sedimentation of a Falling Oblate Ellipsoid. accepted for publication in *Phys. A*.

Fonseca F. and Herrmann H. (2) (2004). Sedimentation of oblate ellipsoids at low and moderate Reynolds number. accepted for publication in *Phys. A.*.

Forster D. (1980). Hydrodynamic Fluctuations, Broken Symmetry and Correlation Functions. *Bejamin/Cummings, Reading, MA, 1975*.

Forster D., Nelson D.R. and Stephen M.J. (1977). Large-distance and long-time properties of a randomly stirred fluid. *Phys. Rev. A.. 16*, 732.

Galdi G. P., Pokorny M., Vaidya A., Joseph D.D. and Feng J. (2001). Orientation of symmetric bodies falling in a second-order liquid at nonzero Reynolds number. *J. Math. Fluid Mech.. 3*, 183.

Goldstein H., Poole C. and Safko D. J. (2002). Classical Mechanics. *Addyson Wesley, San Francisco, 2003*.

Grinstein G., Lee D.H. and Sachdev S.(1990). Conservation laws, anisotropy, and "self-organized criticality" in noisy nonequilibrium systems. *Phys. Rev. Lett.*, *64*, 1990.

Halperin B.I. and Hohenberg P.C. (1977). Theory of dynamic critical phenomena. *Rev. Mod. Phys 49*, 435.

Ham J.M. and Homsy G.M. (1988). . *Int. J.multiphase Flow*. *14*, 533.

Happel J. and Brenner H.(1965). Low Reynolds Number Hydrodynamics. *Englewood Cliffs, NJ: prentice Hall*, 1965.

Herzhaft, B. and Guazzelli, E. (1999). *J. Fluid Mech.. 384*, 133.

Hoyos M., Bacri J.P., Martin J. and Salin, D.(1994). Structure, density, and velocity fluctuations in quasi-two-dimensional non-Brownian suspensions of spheres. *Phys. Fluids.. 6*, 3809.

Höfler K. and Schwarzer S. (2000). Navier-Stokes simulation with constraint forces: Finite-difference method for particle-ladden flows and complex geometries. *Phys. Rev. E. 43*, 761.

Höefler K. (2000). Simulation and Modeling of Mono- and Bidisperse Suspensions. Doctoral Thesis. *Stuttgart University*.

Huang P. Y., Hu H. H. and Joseph D. D. (1998). Direct simulation of the sedimentation of elliptic particles in Oldroyd-B fluids. *J. Fluid Mech.. 362*, 297.

Jánosi I.M., Tel. T., Wolf D.E and Gallas J.A.C. (1997). Chaotic particle dynamics in viscous flows: The three-particle Stokeslet problem. *Phys. Rev.E. 56*, 2858.

Jayaprakash C., Hayot F. and Pandit R.(1993). Universal properties of the two-dimensional Kuramoto-Sivashinsky equation. *Phys. Rev. Lett.. 71*, 12.

Kajikawa M (1982). Observation of the falling motion of early snowflakes. *J. Meteorol. Soc. Jpn. (Suppl.) 1*, 797.

Kalthoff, W. Schwarzer, S. Ristow, G. and Herrmann, H. (1996). On the application of a novel algorithm to hydrodynamic diffusion and velocity fluctuations in sedimenting systems. *Int. J. Mod. Phys. C 7 No.4*, 543.

Kelley Erin and Wu M. (1997). Path Instabilities of Rising Air Bubbles in a Hele-Shaw Cell. *Phys. Rev. Lett. 79*, 1265.

Koch D.L. and Shaqfeh, E.S.G (1991). Screening in sedimenting suspensions. *J. Fluid Mech. 224*, 275.

Koch D.L.(1994). Hydrodynamic diffusion in a suspension of sedimenting point particles with periodic boundary conditions. *Phys. Fluids. 6*, 2894.

Kraichnan R.(1962). Eddy viscosity and diffusivity: exact formulas and approximations. *Phys. Fluids. 5*, 1374.

Kuusela E., Höefler K. and Schwarzer S. (2001). Computation of particle settling speed and orientation distribution in suspensions of prolate spheroids. *J. of Engineering Mathematics 41*, 221.

Kuusela E., Lahtinen, J.M. and Ala-Nissila, T. (2003). Collective effects in settling of spheroids under steady-state sedimentation. *Phys. Rev. Letters. 90*, 094502.

Kuusela E. and Ala-Nissila T.(2001). Velocity correlations and diffusion during sedimentation. *Phys. Rev. E. 63*, 061505.

Kynch G.J.(1952). A theory of sedimentation. *faraday Soc. 48*, 166.

Ladd A.J.C.(1993). Dynamical simulations of sedimenting spheres. *Phys. Fluids A. 5(2)*, 299.

Ladd A.J.C.(1994). Numerical simulations of particulate suspensions via a discretized Boltzman equation. Part 1. Theoretical fundation. *J. Fluids Mech. 271*, 285.

Ladd A.J.C.(1996). Hydrodynamic screening in sedimenting suspensions of non-Brownian spheres. *Phys. Rev. Lett. 76*, 1392.

Ladd A.J.C.(2002). Effects of container walls on the velocity fluctuations of sedimenting spheres *Phys. Rev. Lett. 88*. 048301-1.

Lamb H. (1932). Hydrodynamics. *2nd. Cambridge: Cambridge Univ. Press*.

Landau L.D. and Lifshitz E.M.(1969). Statistical Physics. *Reading, MA; Addison-Wesley*.

Lahiri R. and Ramaswamy S.(1997). Are Steadily Moving Crystals Unstable?. *Phys. Rev. Lett. 79*, 1150.

Lahiri R., Barma M. and Ramaswamy,S (2000). Strong phase separation in a model of sedimenting lattices. *Phys. Rev. E. 61*, 1648.

Landau L.D and Lifshitz I.M.(1959). Fluid Mechanics. *oxford: Pergamond.*

Landau L.D and Lifshitz I.M.(1965). Theory of Elasticity. *Oxford: Pergamond.*

Langevin,P. (1908). Sur la Theorie du Mouvement Brownien *Comptes rendus. 146*, 530.

Lei X., Ackerson B.J and Tong P.(2001). Settling Statistics of Hard Sphere Particles. *Phys . Rev. Lett. 86*, 3300.

Leighton D. and Acrivos A.(1987). The shear-induced migration of particles in concentrated suspensions. *J. Fluid Mech. 181*, 415.

Levine A., Ramaswamy S., Frey E. and Bruisma R. (1998). Screened and unscreened phases in sedimenting suspensions. *Phys. Rev. Lett. 81*, 5944.

Lugt H. J. (1983). Autorotation. *Annu. Rev. Fluid Mech. 15*, 123.

Ma S.K.(1976). Modern Theory of Critical Phenomena. *Reading MA: Benjamin.*

Mahadevan L. , Aref H. and Jones S. W. (1995). Comment on 'Behavior of a Falling Paper'. *Phys. Rev. Lett.. 75*, 1420.

Mahadevan, L. (1996). Tumbling of a falling card. *C. R. Acad. Sci . 323*, 729.

Mahadevan L., Ryu A. and Samuel, D. T. (1999). Tumbling cards. *Phys. Fluids 11*, 1.

Marchildon E. K., Clamenand A. and Gauwin W. H. (1964). Drag and oscillatory motion of freely falling cylindrical particles. *Can. J. Chem. Eng. 64*, 178.

Martin P.C., Parodi O and Pershan P.S.(1972). Unified Hydrodynamic Theory for Crystals, Liquid Crystals, and Normal Fluids. *Phys. Rev. A. 6*, 2401.

Maxwell, J.C. (1853). The Scientific Papers of James Clerk Maxwell. *Cambridge and Dublin Math. J. 9*, 115.

Mises Von R. (1945). Theory of Flight. *McGraw-Hill, New York, 1945.*

Miguel M.-C. and Pastor-Satorras R. (2001). Velocity fluctuations and hydrodynamic diffusion in sedimentation. *Europhys. Lett. 54(1)*, 45.

Nicolai H., Herzhaft B., Hinch E. J., Ogers L. and Guazzelli E. (1995). Particle velocity fluctuations and hydrodynamic self-diffusion of sedimenting non-Brownian spheres. *Phys. Fluids. 7(1)*, 12.

Nicolai H. and Guazzelli E. (1995). Effect of the vessel size on the hydrodynamic diffusion of sedimenting spheres. *Phys. Fluids. 7(1)*, 12.

Olla P. (1999). A simplified model for red cell dynamics in small blood vessels. *Phys. Rev. Lett.. 82*, 453.

Paulin S.E and Ackerson B.J. (1990). Observation of a phase transition in the sedimentation velocity of hard spheres. *Phys. Rev. Lett. 64*, 2663.

Pan T.-W., Joseph D.D., R. Bai, R. Glowinski and V. Sarin (2002). Fluidization of 1024 spheres: simulations and experiments. *J. Fluids Mech. 451*, 169.

Pedley T.J. and Kessley J.O.(1992). *Annu. Rev. fluid Mech. 24*, 313.

Perram J. W. and Rasmussen J. (1996). Ellipsoid contact potential: Theory and relation to overlap potentials. *Phys. Rev. E. 54*, 6565.

Perrin J. (1916). Atoms. *Oxbow Press, Amherst, MA, USA*, 1990.

Peysson Y. and Guazzelli E.(1999). Velocity fluctuations in a bidisperse sedimenting suspension. *Phys. Fluids 11*, 1953.

Press W. h., Flannery B. P., Teukolsky S. A. and Vetterling W. T. (1992). Numerical recipes in C. *Cambridge: Cambridge University Press*.

Priestley C.H.B.(1959). Turbulent Transfer in the Lower Atmosphere. *Chicago: University of Chicago Press*.

Pusey P. and Ramaswamy S.(1997). Theoretical Challenges in the Dynamics of Complex Fluids, Lectures in a NATO Advanced Study Institute Series. 1990.

Qi Dewei., Luo Lishi., Aravamuthan Raja and Strieder William (2002). Lateral Migration and Orientation of Elliptical Particles in Poiseuille Flows. *J. Statist. Phys. 107*, 101.

Ramakrishnan T.V. and Yussouff M.(1979). First-principles order-parameter theory of freezing. *Phys. Rev. B. 19*, 2775.

Ramaswamy S. (2001). Issues in the statistical mechanics of steady sedimentation. *Adv. Phys. 50*, 297.

Richardson J. F. and Zaki W. N. (1954). Sedimentation and Fluidisation: Part I. *Trans. Instn. Chem. Engrs. 32*, 35.

Rouyer F., Martin J. and Salin D.(1999). Non-gaussian dynamics in quasi-2d noncolloidal suspensions. *Phys. Rev. lett. 83*, 1999.

Russel W.B., Saville D.A. and Schowalter W.R (1989). Colloidal Dispersions. *Cambridge: Cambridge University Press*

Saffman P.G.(1975). On the formation of vortex rings. *Stud. appl. Maths. 52*, 115.

Schimittmann B and Zia R.K.P.(1995). Phase Transitions and critical Phenomena. *vol.17*.

Segré P. E., Liu F., Umbanhowar P. and Weitz D. A. An effective gravitational temperature for sedimentation. *Nature 409*, 594.

Segré P.N., Herbolzheimer E. and Chaikin P.M.(1997). Long-range correlations in sedimentation. *Phys. Rev. Lett. 79*, 2574.

Simha R.A. and Ramaswamy S. (1999). Traveling Waves in a Drifting Flux Lattice. *Phys. Rev. Lett. 83*, 3285.

Tanabe Y. and Kaneko K. (1994). Behaviour of a falling paper; reply. *Phys. Rev. Lett. 73 75*, 1372.

Tong P. and Ackerson, B.J.(1998). Analogies between colloidal sedimentation and turbulent convection at high Prandtl numbers. *Phys. Rev. E. 58*, 6931.

Tory E.M., Kammel M.T and Chan Man Fong C.F. (1992). *Powder Technol. 73*, 219.

Viets H. and Lee D. A. (1971). Motion of freely falling spheres at moderate Reynolds numbers. *A.I.A.A. Journal. 232*, 2038.

von SmoluchowskI M.(1916). Three discourses on diffusion, Brownian movements, and coagulation of colloid particles. *Phys Zeits. 17* , 557.

Wachmann B. and Schwarzer S. (1998). Three-Dimensional Massively Parallel Computing of Suspensions. *Int. J. Mod. Phys. C 9(5)*, 759.

Wachmann B., Schwarzer S. and K. Höefler (1998). Local drag law for suspensions from particle-scale simulations. *Int. J. Mod. Phys. C 9(8)*, 1361.

Willmarth W., Hawk N. and Harvey R. (1964). Steady and unsteady motion and wakes of freely falling disks. *Phys. Fluids 7*, 197.

Wu X.-L. and Libchaber A.(2000). Particle Diffusion in a Quasi-Two-Dimensional Bacterial Bath. *Phys. Rev. Lett. 84*, 3017.

Xue J.-Z., Herbolzheimeer E., Rutgers M.A., Russel W.B. and Chaikim P.M. (1992). Diffusion, dispersion, and settling of hard spheres. *Phys Rev. Lett. 69*, 1715.

Xue J.Z., Herbbolzheimer E., Rutgers M. A., Russel W.B and Chaikin P.M.(1995). Crystalline fluidized beds. *Phys. Rev. E. 51*, 4674.

Acknowledgments

I would like to thank Prof. Dr. Hans J. Herrmann for the great opportunity to work at the $ICA1$ and for his invaluable support and orientation, without him, this work would have been impossible.

During my work I had a lot of moral support by my mother, $Florinda$, she helped me along the distance and in all the aspects of life that are more away of Physics. Also, I have to express my gratitude to Diana Alonso, my great adventure partner, we were always side-by-side in our life in Germany.

I am grateful to the members of the ICA1 for the support and the comradeship, specially with Reinmar Mück and Stefan Schwarzer, who guided me at the beginning in the art of simulations. I would like to thank T. Ihle for the physical and scientific critics concerning to my work. My special thanks to V. R. Iyengar and F. Raischel for writting corrections to this work, and also to Marlies Parsons, who supported me at the ICA1 concerning all administrative affairs.

I was very lucky to meet a lot of friends that made my stay in Germany a great expierience of frienship in my life, specially R. Cruz, A. Mora, A. Ehl, J. Garibay, L. López, J.D. Muñoz, O.L. Castro, F. Alonso, J. Jovel, V. Schwaemmle, M. Hasse, L. Aguilera, O. Pozos, M. Sidri and in general to all OLA people.

I am also very grateful to all the latin american community, here in Stuttgart, and in special to the Colombian community, for the wonderful time that we had together along these years.

Morover, I would also like to thank R. Diel for her understanding, affection, generosity and constant support during the last time of my thesis.

I would like to give my gratitude to the project SBF404 of the German Research Foundation (Deutsche Forschungsgemeinschaft) for the financial support.

Finally, I want to express my deepest respect and admiration for the German people that make me possible learn a bit of this great nation.

Frank Rodolfo Fonseca Fonseca
Stuttgart 14th June 2004